THE DESIGN OF A SINGLE ROTOR AXIAL FLOW FAN

FOR A COOLING TOWER APPLICATION

Phillippe Roger Paul Bruneau

Thesis presented in partial fulfillment of
the requirements for the degree of Master of
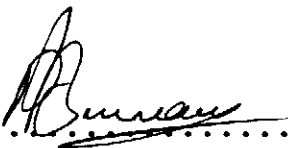Engineering (Mechanical) at the University of
Stellenbosch

Thesis Supervisor : Prof. T.W. von Backström

Declaration

I, Phillippe Roger Paul Bruneau, the undersigned, hereby declare that this thesis is my own original work. It is being submitted for the Degree of Master of Engineering (Mechanical) at the University of Stellenbosch. It has not previously been submitted, in its entirety or in part, for any degree or examination in any other University.

....

Signature of candidate

This .10.th. day of August 1994

i

Abstract

A design methodology for low pressure rise, rotor only, ducted axial flow fans is formulated, implemented and validated using the operating point specifications of a 1/6th scale model fan as a reference. Two experimental fans are designed by means of the design procedure and tested in accordance with British Standards 848, Type A.

The design procedure makes use of the simple radial equilibrium equations, embodied in a suite of computer programs. The experimental fans have the same hub-tip ratio and vortex distribution, but differ in the profile section used. The first design utilises the well known Clark-Y aerofoil profile whilst the second takes advantage of the high lift characteristics of the more modern NASA LS series.

The characteristics of the two designs are measured over the entire operating envelope and compared to the reference fan from which the utility and accuracy of the design procedure is assessed. The performance of the experimental fans compares well with both the reference fan as well as the design intent.

Opsomming

'n Ontwerpmetode vir lae drukstyging, enkel rotor aksiaal waaiers is geformuleer, toegepas en bevestig deur gebruik te maak van die ontwerppunt spesifikasies van 'n 1/6 skaal verwysingswaaier. Twee eksperimentele waaiers is ontwerp deur middel van die ontwerpmetode en getoets volgens die BS 848, Type A kode.

Die ontwerpmetode maak gebruik van die eenvoudig radiale ewewigsvergelykings en 'n stel rekenaarprogramme. Die twee eksperimentele waaiers het dieselfde naaf-huls verhouding en werwel verdeling, maar verskil daarin dat verskillende vleuelprofiele gebruik is vir elkeen van die twee waaiers. Die eerste ontwerp maak gebruik van die bekende Clark-Y profiel terwyl die tweede die moderne NASA LS profiel gebruik.

Die karakteristieke van die twee eksperimentele waaiers is gemeet oor die hele werkbereik en vergelyk met die verwysings waaier waardeur die geldigheid en akkuraatheid van die ontwerpmetode bepaal is. Die werkverigting van die eksperimentele waaiers vergelyk goed met die verwysingswaaier en bevredig die ontwerpsdoelwitte.

Acknowledgements

Table of Contents

List of Tables

List of Figures

Nomenclature

SYMBOL	DESCRIPTION	UNITS
a	swirl coefficient, constant	var
A	cross-sectional area	m^2
b	constant	[.]
c	constant	[.]
$c_{1,2}$	absolute velocity	m/s
c	blade chord	m
c_θ	swirl velocity	m/s
c_x	axial velocity	m/s
C_L	lift coefficient	[.]
C_D	drag coefficient	[.]
d	constant	[.]
d	diameter	m
e	constant	[.]
F	force	N
g	acceleration due to gravity	m/s^2
h	specific enthalpy	J/kg
h	blade height (span)	m
h_{HG}	atmospheric pressure (mm mercury)	mm
i	incidence angle	$(°)$
k	constant	[.]
K_{th}	theoretical pressure rise coefficient	[.]
K_T	total pressure rise coefficient	[.]

K_S	static pressure rise coefficient	[·]
m	mass	kg
$\dot{m}$	mass flow rate	kg/s
n	swirl exponent	[·]
n_b	number of blades	[·]
N	rotational speed	$rev/\min$
p	static pressure	Pa
p_d	dynamic pressure	Pa
p_o	total pressure	Pa
p_{FD}	fan dynamic pressure	Pa
p_{FS}	fan static pressure	Pa
p_{FT}	fan total pressure	Pa
P_{fan}	fan power consumption	kW
Q	volumetric flow rate	m^3/s
r	radius	m
R	gas constant	$J/kg.K$
Re	Reynolds number	[·]
s	blade pitch	m
s	specific entropy	J/kg
t, T	temperature	$°C, K$
t_c	tip clearance	mm
u	specific internal energy	J/kg
U	blade speed	m/s
V	average fan exit velocity	m/s
w	relative velocity	m/s

| W | specific work | J/kg |
| x_b | hub-tip ratio | $[.]$ |

Greek Symbols

α	absolute flow angle	(°)
β	relative flow angle	(°)
ϵ	swirl coefficient	[·]
ϕ	flow factor	[·]
ϕ_{BS}	blade setting angle	(°)
η	efficiency	[·]
ρ	density	kg/m^3
σ	blade solidity	[·]
ξ	stagger angle	(°)
ζ	total pressure loss coefficient	[·]
$\tan(\gamma)$	drag/lift ratio	[·]
Δ	actuator disc decay rate	[·]
Ω	rotational speed	rad/s

Subscripts and Superscripts

a	annulus
act	actual or non-ideal
av	average
amb	ambient/atmospheric conditions
$bell$	bellmouth
d	dynamic component

h	hub
$inlet$	inlet station
$loss$	loss component
p, $plen$	plenum chamber
me	meridional plane
m, $mean$	meanline conditions
o	total quantity
$outlet$	outlet station
r	radial plane
R	rotor
t	tip
th	theoretical or ideal
$\overline{(.)}$	mass averaged quantity
1, 2, 3	station positions
θ	rotational plane, swirl component

1 INTRODUCTION

The purpose of this work is to establish, implement and validate
a rational design procedure for rotor only, ducted axial flow
fans of the low pressure rise type, commonly found in industrial
cooling and ventilation applications. After reviewing the
literature, a design methodology was formulated and implemented
in the form of three computer programs. Using the operating
point specifications of an existing fan as a reference, two
experimental fans were designed, built and tested in accordance
with British Standards 848, Type A. The performance charac-
teristics so obtained were then compared with that of the
reference fan from which the utility and accuracy of the design
procedure was assessed.

The motivation for this study arises from the work of Venter
(1990) who has performed extensive measurements on a 1.542 m
diameter model of the cooling fans installed in the forced
draught condenser of a large power station. Venter's inves-
tigation was directed towards understanding the effects of
different flow resistances and flow distorting components such
as safety grids, walkways, supporting beams and heat exchangers
on the overall performance of the installed units. He also
considered the effects of fan design parameters such as blade
tip clearances and sealing discs and measured the velocity
distributions immediately ahead of and behind the fan blading.
Venter's investigations included the performance measurement
of a 1/6th scale model of a single fan/heat exchanger unit as
well as the isolated model fan in a standard test facility (BS
848 Type A). These measurements indicated that significant
regions of reversed flow were present in the vicinity of the
hub, a phenomenon also encountered in the full scale units and
an obvious source of inefficiency. After effectively increasing

the hub-tip ratio of the model fans from a value of 0.15 to 0.289 by means of a simple flat disc attached to the rotor hub, significant improvements in efficiency were obtained.

The full scale condenser unit consists of 48 fans arranged in a 6x8 array as depicted in Figure 1.1. Because the system consists of a large number of fans in parallel, each drawing air from the atmosphere, the induced flow pattern will result in fans closer to the edge of the fan platform being subject to distorted cross-flows, exacerbated by variable wind direction and strength. Depending on the severity of the distortion (ie non-uniform inlet velocity profiles) the fan blading can stall, accompanied by losses in aerodynamic efficiency and peak pressure rise, as well as blade vibrations.

Two problems directly associated with the fan are highlighted in Venter's study, namely the occurrence of reverse flows in the hub region and the fact that the fans are subjected to distorted inlet flows. These observations suggested that the design of the installed fans be reviewed, attempting to improve the efficiency of the fan whilst maintaining the original pressure rise and volume flow rate. Furthermore, in the interest of minimizing costs, any potential replacement fan should retain the basic configuration and dimensions of the existing fans, ie an eight bladed rotor with no stationary blade rows and rotating at the originally specified speed. Given these constraints, the following considerations were accorded close scrutiny :

    i.   The effects of hub-tip ratio variation and the inclusion of a nose cone

    ii.   Selection of vortex distribution

    iii.   The consequences of different blade profile sections

The scope of the work herein is confined to the design of two single stage, rotor-only fans at the operating point. The two experimental fans are designed with the same hub-tip ratio and vortex distribution, but differ in the profile section used. The first design utilises the well known Clark-Y aerofoil profile whilst the second takes advantage of the high lift character-istics of the more modern NASA LS series. The characteristics of the two designs are measured over the entire operating envelope and compared to the 1/6th scale model reference fan.

The design procedure implemented makes use of the simple radial equilibrium equations, embodied in a suite of computer programs. These provide the user with a ready means to :

    i.   Establish an optimum vortex distribution and hub-tip ratio

    ii.   Perform detailed fan design with an estimate of design point performance

    iii. Generate a blade co-ordinate data file for use on a CAD system and NC machine

The two experimental fans are tested in isolation from system effects, ie in a standard test facility exhausting directly to atmosphere and with no imposed inlet distortion. Whilst the effects of inlet flow distortions and the associated problems have been a motivating factor for this study, time constraints have precluded the measurement of the experimental fans under such conditions. However, during the design phase, due cog-nizance has been given to factors which might improve distortion tolerance and a further study intended to measure inlet distortion performance has been initiated.

The thesis consists of five chapters which cover inter alia, the following topics :

i.   Literature survey and review of the fan design problem

ii.   Fan geometry and symbolic conventions

iii.   Radial equilibrium and vortex distributions

iv.   Description of the design method and computer programs

v.   Description of the experimental fan designs

vi.   Description of the experimental facility and measured parameters

vii.   Presentation of the experimental results

viii. Discussion and conclusions

2 LITERATURE SURVEY AND REVIEW OF FAN DESIGN PROCEDURES

Axial flow fans have been used for displacing large volumes of air against modest pressure rise for many years and became increasingly widespread in Europe during the Industrial Revolution. Nowadays, axial flow fans find general application, ranging from simple desk fans to the first stages of turbo-fan compressors in aviation propulsion systems. Industrial fans lie between these two extremes, providing air for numerous purposes and are required to operate quietly at modest efficiencies against total pressure loads of the order of a few kilopascals.

Until the early years of this century, aerodynamic design methods were rudimentary and predominantly empirical. Bass (1987) notes that the origins of contemporary fan design methods can be attributed to the pioneering aircraft propeller studies of Betz and Prandtl in the early 1920's and subsequently refined by Glauert and Goldstein. With particular reference to ducted axial flow fans, Keller (1937) appears to be the earliest comprehensive treatment whilst workers such as Collar (1940), Patterson (1944) and Thwaites (1951) have subsequently made contributions to fan design theory, specifically windtunnel applications. Van Niekerk's (1958) paper is conspicuous in that it presents a novel method for the optimisation of the fan geometry, obviating the iterative graphical procedures of earlier writers. More recently, Wallis (1983) provides an in-depth treatment of axial flow fans, the associated ducting and system effects and advocates a design procedure based on that of Patterson (1944). Whilst significant advances are evidenced in the treatment of blade losses, exit flow deviation, high solidity blading and general blade design, the synthesis is not remarkably different. Indeed, it is apparent that current design techniques vary little from the original two-dimensional blade element theories of the 1930's and 1940's. In his thesis,

Van Niekerk (1964) comments on the then current state of fan design theory, declaring that very little further development beyond that of Glauert and Keller (1937) had been performed.

The advent of digital computers in the early 1960's and extensive research and development into turbo-compressors and turbines have resulted in numerous numerical methods and computer programs for resolving the complicated flow fields within turbomachine blade passages. However, Wallis (1983) and Bass (1987) both consider that in general, design requirements for industrial fans are not so formidable that the application of three-dimensional methods are warranted. In contrast, Bard and Böös (1987) describe a computer based design procedure which utilises streamline curvature and finite difference techniques to design and analyse fan blading. They claim that the usage of advanced computer methods can be especially effective as a diagnostic tool in cases where system effects alter fan performance adversely. They also note that there is still much reticence amongst fan manufacturers to implement these methods, ostensibly on the grounds that the complexity of the programs and the cost of hardware and software are economically prohibitive.

Smith (1987) concurs with Wallis (1983) and Bass (1987) on the necessity for advanced computer methods. He advocates a "traditional" two-dimensional analysis of a pressure rise calculated from the average change in momentum. He further describes a suite of computer programs which implement the method. Smith stresses the importance of being able to compare the measured flow conditions with those calculated by the design programs, noting that a knowledge of the pressure distribution upstream and downstream of a blade row enables losses and section efficiencies to be calculated, thereby indicating where design changes are needed. Due to the slow response time of yawmeters, only average pressures, velocities and flow-angles are measured.

6

Smith argues that with this limitation on the pressure measurement and in the interest of feeding back measured data into the design process, there is little advantage in pursuing a complicated three-dimensional approach which computes detailed blade flow fields and streamlines.

In reviewing the literature on fan design, it is clear that most design procedures are fundamentally the same, the only real differences in approach being that of blade selection and optimisation. Moreover, the abundance of publications addressing system effects and noise measurement/control would suggest that fan manufacturers and users give precedence to these issues over aerodynamic design and efficiency. Nevertheless, the value of sound design technique is stressed by Wallis (1983) :

> "...axial flow fans are finding greater acceptance in industrial applications, as alternative equipment to the radial flow variety. However, the full potential of the axial flow fan will only be realised when modern design techniques and the latest information are utilised to the fullest extent. At present [1983] the percentage of ineffectual axial flow fan installations is considerably higher than that for its radial counterpart. The problem arises because of an unrefined aerodynamic design approach adopted by many duct and fan engineers."

2.1 The Fan Design Problem

In this section, the fan design problem is briefly reviewed and summarised. Firstly, the notation used in this work is presented, after which approaches to blade design are discussed. In this work, the nomenclature used is based on that

of Dixon (1978) but in those cases where Dixon does not discuss a particular parameter, the symbols of Wallis (1983) have been adopted.

2.1.1 Nomenclature

The most general fan configuration is one that consists of three blade rows bounded by an inner and outer shroud, as depicted in Figure 2.1 The first blade row comprises the non-rotating inlet guide vanes which consist of flow accelerating (nozzle type) blades. The second row of blades is the fan rotor which imparts kinetic energy to the working fluid, driven by some external power source. The third blade row, also non-rotating, is the flow straightener whose function it is to extract the residual swirl velocity component at the rotor exit and to recover some of the exit kinetic energy in terms of a static pressure rise.

Depending on the desired pressure rise and volume flow rate characteristics of a fan, the various combinations of inlet guide vanes, rotor rows and flow straighteners may be employed. The most frequently encountered configurations are as follows :

    i.   Inlet guide vanes, single rotor and flow straightener

    ii.   Inlet guide vanes and rotor

    iii.   Rotor and flow straightener

    iv.   Rotor only

    v.   Two contra-rotating rotors

Most fan applications will make use of at least an outer shroud with an inner, or hub shroud as necessary. Only

single rotor configurations appear in some cases without either hub or tip shrouds. A schematic of the shrouded, single rotor type fan of interest in this study is illustrated in Figure 2.2, indicating the station numbering to be used in the remainder of the text.

The velocity triangles for both the general fan configuration and the rotor only configuration are presented in Figure 2.3 and 2.4. Table 2.1 lists the symbols and meanings of the velocity vectors. The convention used here is to denote the inlet flow angles as positive when measured clockwise from the machine axis, while the absolute outlet flow angle is positive measured anti-clockwise from the machine axis. The relative outlet flow angle is measured positive in a clockwise direction from the machine axis.

Figure 2.5 shows a two-dimensional section through a fan rotor cascade at a given radius and Table 2.2 lists the various parameters.

2.1.2 Fan Design

The design of an axial flow fan is an iterative process which may be considered in four phases :

    i.   The specification of the design objectives in terms of overall pressure rise and volumetric flow rate. The application will dictate the pressure rise and volumetric flow rate with possibly the outer diameter and rotational speed constrained by installation and power source limitations.

9

ii. Establish the general configuration (eg number/type of blade row(s), hub-tip ratio) based on the design objectives.

iii. Design the blading that will achieve the pressure rise whilst passing the desired flow rate according to some criterion such as maximum efficiency or minimum cost.

iv. Perform the structural design to ensure that the blades are capable of withstanding the expected aerodynamic and centrifugal loads

As mentioned previously, any improvements to the existing fan were to be confined to vortex distribution, hub-tip ratio and blading selection. Consequently, only phases ii. and iii. are discussed from here on.

When designing a fan, the following general assumptions are made :

i. The flow is incompressible

ii. The hub and outer shroud form concentric cylinders

iii. The flow both upstream and downstream of the blade rows is symmetric

iv. The swirl distribution is a free-vortex

v. The blade can be considered to be made up of a series of two-dimensional sections along the blade length and the flow at each of these sections can be considered two-dimensional

The free-vortex assumption,

$$c_\theta = \frac{k}{r} \qquad \qquad 2.1$$

indicates that the swirl velocity is inversely proportional to the radius and provides the starting point for the majority of authors because it results in two simplifying flow features. Firstly, the axial velocity through a blade row is constant, both along the blade span (ie radially) and through the fan (ie axially). Secondly, the work and total pressure distributions along the blade span are also constant.

Although the details differ from author to author, the following summarises the basic approach to fan sizing and the determination of velocity triangles.

Because the axial through flow velocity is constant, ie, $c_{x1} = c_{x2} = c_x$, the continuity equation can be used to obtain

$$Q = \pi r_t^2 (1 - x_b^2) c_x \qquad \qquad 2.2$$

Assuming the volumetric flow rate and tip radius will be specified by the application, the axial velocity corresponding to a number of different hub-tip ratios can be calculated.

The Euler work equation (Dixon (1978))

$$P_{o2} - P_{o1} = \rho U (c_{\theta 2} - c_{\theta 1}) \qquad \qquad 2.3$$

describes the relationship between swirl velocity and total pressure rise along a streamline through the fan. For a single rotor fan, the absolute inlet velocity is assumed to be axial and hence the inlet swirl velocity is also zero. Substituting the expression for swirl velocity into the Euler work equation results in

$$p_{o2} - p_{o1} = \rho \Omega r \left(\frac{k}{r} \right) = \rho \Omega k \qquad 2.4$$

which indicates that the total pressure distribution at station 2 is constant. Since the rotational speed and total pressure will be specified, the swirl constant, k, can be determined.

In order to select an appropriate hub-tip ratio, Patterson (1944) and Wallis (1983) place a maximum value on the hub swirl coefficient

$$\epsilon_{2h} = \frac{c_{\theta_2}}{c_x} \qquad 2.5$$

which is equivalent to limiting the permissible angle of exit swirl at the hub since

$$\alpha_2 = atan \left(\frac{c_{\theta_2}}{c_x} \right) \qquad 2.6$$

A hub-tip ratio corresponding to a hub swirl coefficient less than or equal to 1.0 results in blading that can be designed using isolated aerofoil theory. When higher swirl coefficients are used, interference effects must be taken into account. Some authors such as Osborne (1966) will place experience based limits on the hub and tip flow factors instead, ie

$$\phi_h = \frac{c_x}{U_h} = \frac{c_x}{\Omega r_h} \qquad 2.7$$

$$\phi_t = \frac{c_x}{U_t} = \frac{c_x}{\Omega r_t} \qquad 2.8$$

Once a suitable value for the hub-tip ratio has been established, the radial distributions of the velocity vectors and angles can be determined via the geometry of the velocity diagrams.

Blade design may in principle be approached in two ways, namely the treatment of the blade as a series of isolated aerofoil sections, or by regarding the blades as a rotating cascade. In practice, the method implemented depends on the blade solidity, ie

$$\sigma = \frac{c}{s}$$ 2.9

which in turn is dependent on the blade loading factor, $C_L \sigma$. Early on in the design process, the appropriate method becomes apparent although it frequently happens that both are employed, ie cascade at the hub and isolated aerofoil at the tip.

The isolated aerofoil approach treats each blade as a series of two-dimensional aerofoil sections, considers the lift and drag forces acting on them and resolves these into torque and thrust planes. Integrating from hub to tip gives shaft torque and static pressure rise across the rotor exit plane. Calculations of the local lift and drag forces require a knowledge of the local air velocity relative to the blade which can to some extent be controlled by the choice of swirl and pressure distribution.

The equation for blade loading, derived in Appendix C, is given by

$$C_L \sigma = 2 \left(\frac{c_{\theta_2}}{c_x} \right) \cos \beta_m$$ 2.10

where C_L is a blade section lift coefficient and β_m is the mean flow angle relative to the rotor blade, defined as

$$\tan\beta_m = \frac{1}{2}(\tan\beta_2 + \tan\beta_1) \qquad\qquad 2.11$$

The flow angles and swirl distribution will be known from the velocity distribution, so the blade loading factor can be calculated at all radial stations along the blade span. In order to calculate the blade chords and stagger angles for the blade sections, Wallis (1983) recommends the following :

i.   Depending on the aerofoil profile to be used, suitable values of lift coefficient at the hub and tip are selected. Since most profile sections will have a peak lift coefficient in the region of 1.2 to 1.4, the maximum value is taken to be 1.0 at the hub and in the range 0.4 to 0.6 at the tip. A linear interpolation between the hub and tip values gives lift coefficients along the blade span.

ii.   the solidity along the blade span is calculated from the loading factor and lift distributions, after which the chords at each section are determined from

$$c = \frac{2\pi r}{\sigma n_b}$$

where n_b is the number of fan blades. It frequently occurs that the chord lengths so obtained are too large at the hub to be practical. By varying the lift coefficient distribution and number of fan blades, acceptable values can usually be arrived at.

Limitations to the isolated aerofoil approach become apparent when blades are sufficiently close to each other for the suction and pressure surface velocity fields to interact and seriously restrict the development of the full lift forces. A number of empirical corrections to the lift slope and zero lift line are available, but for solidity values greater than approximately 0.7, the reliability of the isolated aerofoil approach deteriorates. Attempts have been made to extend the scope of isolated aerofoil theory to closely spaced blades by the introduction of an interference factor, defined as the ratio of the lift force of single blade in a cascade to that of an isolated single blade.

When the isolated aerofoil assumption is valid, any aerofoil section for which lift and drag coefficient data is available may be used. In the case of blading with small flow turning, Osborne (1966) and Wallis (1983) suggest the use of flat undersurface profiles such as the Göttingen 436, RAF-6 or Clark-Y. In those cases where the solidity is high enough to demand a cascade approach, a number of methods are reported in the literature. The approach advocated by Wallis (1983) is the use of F-series aerofoils, which are essentially C-4 circular arc sections with a local increase in nose camber. The method allows the designer to tailor the camber, thickness and any extra nose camber for any solidity. The F-series of blades provides a unified approach to fan blade design

15

but Hay, Metcalfe, Reizes (1978) note that since Wallis' method is geared towards giving the best aerodynamic performance, blading designed via this method will operate closer to the stall point. In those cases where the fan installation is such that distorted inlet flows are present, higher noise levels can be expected. McKenzie (1987) proposes a method for selecting C-4 profiles for optimum efficiency, similar to that of Hay, Metcalfe, Reizes (1978). Hay et al (1987) have extended the work of Hay, Metacalfe, Reizes (1978) and McKenzie (1987), adopting a philosophy aimed at reducing fan noise. This is achieved by choosing the design to be far away from the stall whilst maintaining high efficiencies, albeit somewhat reduced from that of McKenzie (1987). The design method is particularly suited to industrial applications which may be subject to inlet flow distortions.

2.1.3 Fan Performance

The procedure used to describe the experimentally measured fan performance follows that of Venter(1990) who in accordance with the BS 848 Type A (1980) fan test code and the recommendations of Wallis (1983) plots fan static pressure, fan static efficiency and power consumption against volumetric flow rate. These parameters are defined with reference to Figure 2.2.

2.1.3.1 Fan Pressures

BS 848, Type A (1980) (see also Osborne (1966) and Wallis (1983)) defines the fan total pressure as

$$p_{FT} = p_{o2} - p_{o1} \qquad\qquad 2.12$$

which is the difference between the total pressures at fan inlet and outlet.

The fan dynamic pressure is that corresponding to the average velocity at the fan outlet, obtained by dividing the volume flow rate by the area of the fan outlet annulus, ie

$$p_{FD} = \frac{1}{2}\rho V_2^2$$

2.13

where

$$V_2 = \frac{Q}{A_2}$$

2.14

and A_2 is the fan exit flow area based on the shroud diameter.

The fan static pressure is given by

$$p_{FS} = p_{FT} - p_{FD}$$

2.15

which is the fan total pressure less the fan velocity pressure, equivalently expressed

$$p_{FS} = p_{o2} - p_{o1} - \frac{1}{2}\rho V_2^2 = p_2 - p_{o1}$$

2.16

In effect, BS 848 Type A is defining the exit static pressure, p_2 as

$$p_2 = p_{o2} - \frac{1}{2}\rho V_2^2$$

2.17

For design puposes in this work, the total to static
efficiency is used, namely

$$p_{ts} = p_{o2} - \frac{1}{2}\rho\left(c_x^2 + c_{\theta_2}^2\right) - p_{o1}$$
2.18

where the dynamic pressure is given by

$$p_d = \frac{1}{2}\rho\left(c_x^2 + c_{\theta_2}^2\right)$$
2.19

to yield

$$p_{ts} = p_2 - p_{o1}$$
2.20

An examination of Equations 2.16 and 2.18 reveals that the
fan static pressure and total to static pressure are not
the same. However, as far as the comparsion of calculated
and measured performance is concerned, this is not a
contradiction because when the fan static pressure is
measured experimentally (see Appendix D), the average exit
velocity, V_2, is not used to deduce the fan static pressure.
The fan static pressure is obtained directly by measuring
the static pressure difference between the atmosphere
(station 2, Figure 2.2) and the total pressure at inlet
(station 2, Figure 2.2). The fan static pressure as measured
in accordance with BS 848, Type A and the total to static
pressure as calculated are in fact the same quantity. For
the sake of correctness in the remainder of the text, the
term "total to static pressure" is used when reference is
made to the design static pressure rise and appropriately,
"fan static pressure" is used for the experimentally
measured static pressure rise.

18

2.1.3.2 Efficiency

Two efficiencies are defined by BS 848, Type A, namely a fan total efficiency and fan static efficiency, respectively defined by the following equations :

$$\eta_{FT} = \frac{p_{FT}Q}{P_{fan}}$$

2.21

$$\eta_{FS} = \frac{p_{FS}Q}{P_{fan}}$$

2.22

where P_{fan} is the measured fan input power.

As explained above regarding the usage of "total to static pressure" and "fan static pressure" the total to static efficiency is defined

$$\eta_{ts} = \frac{p_{ts}Q}{P_{fan}}$$

2.23

3 RADIAL EQUILIBRIUM AND VORTEX DISTRIBUTIONS

The central theme of all the fan design procedures examined in the literature survey is the assumption of a free vortex swirl distribution. Most authors advocate the use of a free vortex because of the ensuing design simplifications in respect of radially constant axial velocity, total pressure rise and work distributions. Furthermore, both Wallis (1983) and Bass (1987) indicate that this swirl distribution generally results in the highest efficiencies. However, it was considered prudent to closely examine the effects of different swirl distributions on fan design and performance, particularly in view of the stated objectives of this work.

In this chapter, the radial equilibrium equations are derived and the implications of different swirl distributions summarised.

3.1 Radial Equilibrium

The simplest approach to the study of axial flow turbomachines is to assume that the flow conditions prevailing at the meanline are fully representative of the flow at all other radii, ie a single velocity diagram is assumed to represent the average conditions along the entire blade span. This two dimensional analysis at the mean line can provide a reasonable approximation to the actual flow if the hub-tip ratio is large, in excess of 0.8. In the case of lower hub-tip ratios, substantial radial variations in the velocity triangles are encountered, and mean line velocity diagrams do not of necessity represent the average flow conditions for the entire blade span. The changing shape of the velocity diagrams along the blade span are a manifestation of the radial variation in blade speed, radial components of velocity and the balance of forces that must exist in the flow. Considerations must therefore also

be given to the hub and tip regions, since the redistribution of mass flow arising from radial variations will markedly affect the outlet velocity profiles, flow angle distributions and ultimately, the power input to the flow.

Radial flow acceleration within a turbomachine is caused by the imbalance between the centrifugal forces and the radial pressures restoring equilibrium. Thus, for example, radial mass redistribution towards the blade tip will continue until the resulting pressure increases counteract the radial flow.

Consider an element of fluid in a generalised turbomachine flow field as depicted in Figure 3.1(a). When there is a tangential component of velocity, the resulting circumferential flow (Figure 3.1(b)) must be maintained by a pressure force. The pressure force serves to balance the centrifugal force acting on the fluid and to keep the fluid element moving along its curved path in the tangential direction. When the axial through flow path (streamline) travelled by the fluid element is curved (Figure 3.1(c)), additional forces are required to maintain the flow along the curved path and must be accounted for as part of the nett pressure force. Any linear acceleration of the flow must also have an associated pressure force, part of which is in the radial direction if the streamline is inclined from the horizontal. The balance of forces required to account for these factors is termed "Radial Equilibrium".

The force on a fluid element due to gravity is neglected and if unit length is assumed in the x-direction, the nett pressure force (directed radially inward) is :

$$F_{p,nett} = (p+dp)(r+dr)d\theta - prd\theta - 2\left(p+\frac{dp}{2}\right)dr\sin\frac{d\theta}{2} \qquad 3.1$$

21

Neglecting higher order terms and setting $\sin(d\theta/2) = d\theta/2$ yields :

$$F_{p,nett} = r.dp.d\theta \qquad\qquad 3.2$$

The mass of fluid acted on by the pressure force is :

$$m = \rho[\pi(r+dr)^2 - \pi r^2]\frac{d\theta}{2\pi} \qquad\qquad 3.3$$

which reduces to

$$m = \rho r\, dr\, d\theta \qquad\qquad 3.4$$

To balance the centrifugal force associated with the circumferential flow, the radial pressure force is :

$$F_{p,c} = m\frac{c_\theta^2}{r} = \rho r\, dr\, d\theta\frac{c_\theta^2}{r} = \rho c_\theta^2\, dr\, d\theta \qquad\qquad 3.5$$

The radial component of the pressure force required to balance the centrifugal force associated with the flow along the meridional streamline is :

$$F_{p,s} = -m\frac{c_{me}^2\cos\alpha_{me}}{r_{me}} = -\rho r\, dr\, d\theta\frac{c_{me}^2\cos\alpha_{me}}{r_{me}} \qquad\qquad 3.6$$

The positive directions for the streamline curvature and inclination angle are indicated in Figure 3.1(c). The minus sign in the equation indicates that the balancing pressure force required to produce the linear acceleration along the meridional streamline is :

$$F_{p,l} = -m \frac{dc_{me}}{dt} \sin \alpha_{me} = -\rho \, r \, dr \, d\theta \frac{dc_{me}}{dt} \sin \alpha_{me}$$ 3.7

Setting the nett radial pressure force equal to the various components yields :

$$\frac{1}{\rho} \frac{dp}{dr} = \frac{c_\theta^2}{r} - \frac{c_{me}^2}{r_{me}} \cos \alpha_{me} - \frac{dc_{me}}{dt} \sin \alpha_{me}$$ 3.8

This equation is the "Radial Equilibrium Equation" (REE), and includes all contributing factors. Streamline Curvature Methods (SCM's) as reported by Novak (1967), Smith (1966) and others, have been used successfully in the past to solve this equation for compressor and turbine flow problems. However, SCM procedures are relatively complicated to implement and as a first attack on the design problem, it is not always convenient to use the REE in complete form as above. For axial flow (or near axial flow), and concentric hub and tip shrouding, the meridional streamline curvatures ($1/r_{me}$) and inclination angles α_{me} are both quite small. Therefore the last two terms on the right hand side of the radial equilibrium equation are small compared to the first (rotational) term and can often be neglected, resulting in

$$\frac{1}{\rho} \frac{dp}{dr} = \frac{c_\theta^2}{r}$$ 3.9

This approximation to the REE is known as the "Simple Radial Equilibrium Equation" or SREE. In the following, four different forms of the SREE are derived and utilised, and for the sake of brevity, the above equation is referred to as SREE(1).

In an annular flow where there is no radial component of velocity, the stream surfaces are concentric cylindrical surfaces, and the flow is in radial equilibrium. The Simple Radial Equilibrium Method is based on the premise that any radial flow that does occur only takes place within the blade passage (see Figure 3.2). The flow entry to, and exit from the blade row is in equilibrium. The assumption also implies that the flow is axisymmetric and steady and therefore the effect of discrete blade wakes is not transmitted to the flow.

3.2 The Simple Radial Equilibrium Equations

In the following, the approach of Dixon (1978) is used to provide simplified forms of the radial equilibrium equations suitable for design work. If the streamline slope is assumed to be zero at some axial stations far ahead and behind a blade row, there is no radial component of velocity and the total enthalpy at both these locations may be written

$$h_o = h + \frac{1}{2}(c_\theta^2 + c_x^2) \qquad\qquad 3.10$$

Differentiating with respect to radius gives

$$\frac{dh_o}{dr} = \frac{dh}{dr} + c_x\frac{dc_x}{dr} + c_\theta\frac{dc_\theta}{dr} \qquad\qquad 3.11$$

Now substituting the thermodynamic relation

$$T\frac{ds}{dr} = \frac{dh}{dr} - \frac{dp}{\rho dr} \qquad\qquad 3.12$$

and incorporating SREE(1) yields

24

$$\frac{dh_o}{dr} - T\frac{ds}{dr} = c_x\frac{dc_x}{dr} + \frac{c_\theta}{r}\frac{d(rc_\theta)}{dr}$$ 3.13

For a single stage axial fan under ideal conditions, the flow at the inlet to the fan is assumed to be radially uniform, (constant inlet axial velocity), so the total inlet enthalpy and entropy are also constant. The rotor does not necessarily impart constant work to the flow and in general will not induce radially constant losses. At any point through the fan, radial gradients of enthalpy and entropy will be dependent on the uniformity of the inlet flow, the gradients imposed by the rotor blades, and the gradient damping due to radial mixing.

If an ideal fan is considered, ie losses are neglected, the entropy gradient will be zero and therefore the SREE may be written as

$$\frac{dh_o}{dr} = c_x\frac{dc_x}{dr} + \frac{c_\theta}{r}\frac{d(rc_\theta)}{dr}$$ 3.14

and designated SREE(2)

Furthermore, if the flow is assumed incompressible, as in the case of a low pressure rise fan, the total pressure is given by

$$p_o = p + \frac{1}{2}\rho(c_x^2 + c_\theta^2)$$ 3.15

Differentiating with respect to radius gives

$$\frac{1}{\rho}\frac{dp_o}{dr} = \frac{1}{\rho}\frac{dp}{dr} + c_x\frac{dc_x}{dr} + c_\theta\frac{dc_\theta}{dr}$$ 3.16

25

and upon substituting into SREE(1) obtain

$$\frac{1}{\rho}\frac{dp_o}{dr} = \frac{c_\theta}{r}\frac{d}{dr}(rc_\theta) + c_x\frac{dc_x}{dr}$$

3.17

which is the third form of the SREE, SREE(3). This equation provides a relationship between the total pressure, swirl velocity and axial velocity and may be used in both the "indirect" and "direct" design problems. In the "indirect" case, a swirl velocity distribution is specified and the axial velocity distribution is deduced, whereas in the "direct" problem, the swirl angle variation is specified and the axial and swirl velocities are calculated.

By imposing the additional restriction that the total pressure gradient is zero, the fourth form of the SREE, SREE(4) is obtained :

$$c_x\frac{dc_x}{dr} + \frac{c_\theta}{r}\frac{d}{dr}(rc_\theta) = 0$$

3.18

3.3 Radial Velocity Triangle Variations

Although enthalpy gradients (or total pressure gradients) behind blade rows will in general be non-zero, SREE(4) can be used to gain some insight into the consequences and effects of different swirl distributions on radial velocity triangle variation. Following the approach of Glassman (1975), it is convenient to consider this special case of the SREE because due to the relatively simple form of the equation, it is easily integrated to give closed form expressions for the axial and swirl velocities. Although the following analysis does not provide accurate results in terms of absolute values, the general trends are indicated.

In the design of axial flow turbomachines, a power law swirl distribution of the form

$$c_\theta = a r^n \qquad \qquad 3.19$$

has often been used and is assumed here. In this expression, 'a' and 'n' are constants. Substituting the power law swirl distribution into SREE(4) and integrating between the limits of r_m and r gives :

$$\frac{c_x}{c_{x,m}} = \left\{ 1 - \tan^2\alpha_m \left(\frac{n+1}{n} \right) \left[\left(\frac{r}{r_m} \right)^{2n} - 1 \right] \right\}^{1/2} \qquad 3.20$$

where α_m and $c_{x,m}$ are the absolute flow angle and axial velocity at the mean radius. The above equation is valid for all values of exponent 'n' except 0, in which case the integration provides :

$$\frac{c_x}{c_{x,m}} = \left\{ 1 - 2\tan^2\alpha_m \ln\left(\frac{r}{r_m} \right) \right\}^{1/2} \qquad 3.21$$

Another swirl distribution case of interest not covered by the power law form is that of constant absolute outlet angle α, ie

$$c_\theta = c_x \tan\alpha \qquad \qquad 3.22$$

Substitution into SREE(4) and integration effects

$$\frac{c_x}{c_{x,m}} = \left(\frac{r}{r_m} \right)^{-\sin^2\alpha} \qquad 3.23$$

The radial variations in swirl velocity, axial velocity and flow angle for a mean radius flow angle of 30° are computed from the above equations and presented in Figures 3.3, 3.4 and 3.5. Immediately apparent is the strong dependence of axial velocity and flow angle variation on the specified swirl distribution. As the swirl distribution exponent 'n', deviates from a value of -1, the changes in axial velocity and flow angle become more exaggerated. As indicated in the graphs, the axial velocities and flow angles associated with certain values of 'n' cannot be obtained with all blade lengths (ie hub-tip ratios). The range of 'n' that can be used for design purposes becomes larger as the hub-tip ratio increases.

3.4 Swirl Velocity Distributions

As indicated above, the design problem requires that a swirl velocity distribution be specified and the other flow parameters are deduced as a consequence of the swirl distribution. The designer is therefore faced with the decision as to which swirl distribution to choose so that all the design constraints and specifications will be satisfied.

In the past, a number of standard swirl distributions have been used in turbomachine design, each having its own merits and applicability. Amongst the most commonly used swirl distributions are the free vortex, forced vortex and general swirl distributions, described below.

3.4.1 Free Vortex

When a value of -1 is used for the swirl exponent 'n', the swirl velocity distribution is given by

$$c_\theta = \frac{k}{r}$$

which is the condition for a free vortex distribution. The free vortex is widely used in all types of turbomachines where the radial variation of velocity diagrams is taken into account.

If the free vortex condition is specified at both stator and rotor outlets, then there is no radial variation in the specific work $\Delta(\Omega r c_\theta)$ because both $(r c_\theta)_{outlet}$ and $(r c_\theta)_{inlet}$ are radially constant. Thus the specific work calculated from the mean line velocity diagram is valid for the entire flow. Furthermore, since the axial velocity remains radially constant through a blade row, there is no streamline curvature through the fan.

Design simplicity is one of the main reasons for the widespread use of the free vortex, however, as evidenced in the graph (Figure 3.5), a potential problem is that of excessive blade twist. For the case indicated, the difference between inlet and exit absolute flow angle is of the order 60° which results in a blade having an overhanging tip section. This situation may elicit manufacturing difficulties and excessive bending stresses. Furthermore, in the case of a single rotor fan without stators to extract the exit swirl velocity component, free vortex designs can lead to excessive root swirl with an attendant increase in losses.

3.4.2 Non Free Vortex Distributions

Free vortex designs are so commonly used that all other distributions are often classified together in the "non free vortex category" and are implemented in an attempt to alleviate some of the potential disadvantages associated with the free vortex.

The constant flow angle design (n=1) results in velocity triangle diagrams broadly similar to the free vortex and is therefore subject to the same problem of high rotor blade twist. A possible advantage is that if a stator is used, this blade row is untwisted whereas in the free vortex case, both stator and rotor rows are twisted.

The super vortex (n=-2) appears to have no advantage of any sort, the blade twist being more severe that for the free vortex. The exit velocity variation is large and cannot be sustained on blades with hub-tip ratios much below 0.6.

The constant swirl (n=0) and forced vortex distributions do ameliorate the blade twist problems of the free vortex, however, here too, the radial variation in axial velocity is large and cannot be sustained on blades with hub-tip ratios below approximately 0.2.

For single rotor fans, the non free vortex distributions all imply radial variation in specific work. Moreover, the radial gradient in axial velocity is responsible for a radial variation in mass flow rate per unit area, resulting in streamline shift through the machine. The mean section conditions will not represent true average conditions and considerable error may be incurred if a fan is designed on the basis of the meanline flow conditions alone. A non-free vortex machine must be designed by integrating the flow conditions between hub and tip in order to compute work and flow rate. The proper design of a non-free vortex design is therefore more complex than that of the free vortex variety.

4 DESIGN METHOD

The design of the candidate fans was performed in two phases, the first being an optimisation of the vortex and hub-tip ratio, and the second, the design of the fan blading. The design procedure was implemented in three computer programs, FANVTX, FANOPT and FANBLD. FANVTX and FANOPT were used to study the effects of vortex distribution and hub-tip ratio variations on efficiency for a given design point duty. Based on the findings of this study, a swirl distribution and hub-tip ratio were selected for the new designs, after which blade details were determined by means of program FANBLD.

In this chapter, the design and manufacture of the two test fans is described and discussed under the following headings:

    i.   Design specification and constraints

    ii.   Optimisation of the vortex distribution and hub-tip ratio

    iii. Blade design and profile selection

    iv.   Manufacture of the test fans

4.1 Design Specification and Constraints

The control fan, referred to as the V-Fan, is a 1/6th scale model of the operational fan. The rotor, depicted in Figure 4.1 is eight bladed with no hub shroud or nose cone with the aerofoil section and planform shown in Figure 4.2. The blades of the V-fan have very little twist which would indicate an arbitrary vortex design. It should also be noted that since the blade sections are not exact replicas of the full scale

fan (see Figure 4.3), the comparative performances of the V and experimental fans cannot be strictly extrapolated to the full scale.

Venter (1990) tested the V-fan with and without hub plates and found that the inclusion thereof improved the efficiency and pressure rise characteristics. In order to establish a starting point for the design of the candidate fans, the design operating conditions for the V-fan with hub plate, listed in Table 4.1 were assumed. Fan static pressure rise, volumetric flow rate and rotational speed would normally be prescribed as design constraints, the fan power consumption and efficiency being predicted by the designer as a consequence of the design constraints, blading geometry, installation, etc. However, since the fans considered here are possible replacements for existing machines, the maximum power consumption is restricted by the capabilities of the electric motors already installed. For this reason, the power consumption, volumetric flow rate and rotational speed were regarded as the primary (fixed) constraints whilst the values of fan static pressure rise and efficiency listed in Table 4.1 were considered lower limits.

Furthermore, in the interests of minimising the costs of replacement, the only major design changes were to be restricted to the following :

   i.   Hub-tip ratio

   ii.   Vortex distribution

   iii. Blade profiles

   iv.   The inclusion of a nose cone

4.2 Optimisation of the Vortex Distribution and Hub-tip ratio

Program FANVTX calculates the velocity triangle vectors, pressure distributions and efficiencies for a single stage, rotor only fan at the design point. The specified parameters include the hub-tip ratio, ambient conditions, volumetric flow rate and exit swirl velocity distribution (or absolute outlet angle distribution). With regard to the specification of swirl velocity, the user can either provide specified values in tabular form, or select a power law distribution of the form

$$c_\theta = a r^n \qquad\qquad 4.1$$

where the swirl exponent 'n', is specified and constant 'a' is initially unknown.

Using this latter option, the optimisation exercise was started by calculating a number of possible designs for a range of hub-tip ratios. For each combination of swirl exponent and hub-tip ratio, the value of the constant 'a' corresponding to the prescribed total to static pressure and flow rate was determined. The data from all these computations was plotted as total to static efficiency vs swirl exponent for lines of constant hub-tip ratio, indicating that a swirl distribution very close to a free vortex (ie n = -1) was an optimum. The corresponding hub-tip ratio was close to 0.2.

In the second part of the optimisation, the method of Van Niekerk (1958) was used to obtain an optimum hub-tip ratio. In this approach, the fan is assumed to be a free vortex design. The method includes allowances for blade and annulus losses and is therefore a more realistic approach. The results of these computations were plotted as total to static efficiency vs total to static pressure for a number of different hub-tip ratios, indicating that a hub-tip ratio of 0.4 was an optimum.

The method and sequence of calculations in the two programs is summarised here. Only the final form of the equations are presented and the reader is referred to Appendices A and B for the detailed derivations.

4.2.1 FANVTX

Apart from the selection of swirl distribution, program input includes the specification of general geometric and operating data with which the solution of SREE(3) in conjunction with the chosen swirl distribution yields the axial exit velocity and total pressure variation across the fan exit plane. From these calculated data, the remaining exit flow conditions (velocity triangle components and static pressure) as well as the mass averaged efficiency, power absorption and overall pressure rise are deduced. Finally, actuator disc theory is used to estimate the shape of the streamlines through the fan blade row. The flow is assumed to be incompressible and isentropic and although no viscous losses are calculated, the "wasted" kinetic energy in the exit flow is determined. The fan hub and tip shrouds are also assumed to be concentric cylinders.

FANVTX allows the designer to establish the effects of overall sizing (particularly hub-tip ratio), swirl distribution and operating conditions such as rotational speed and flow rate on the ideal performance of a fan. The fact that the flow is assumed to be ideal is no real disadvantage as viscous losses are estimated when the blading is designed, ie in program FANBLD.

The sequence of calculations in FANVTX is as follows :

    i.   Input specification

    ii.   Preliminary calculations

34

iii. Iteration for the axial exit velocity dis-
     tribution

iv. Calculation of flow parameters

v. Streamline estimation

4.2.1.1 Input Specification

The user provides the following data to start the calcu-
lations :

i. Tip radius

ii. Hub-tip ratio

iii. Ambient pressure

iv. Ambient temperature

v. Volumetric flow rate

vi. Rotational speed

vii. Swirl exponent

viii. Swirl coefficient

ix. Number of radial stations across the fan
    annulus

x. Number of streamlines

xi. Number of axial stations for streamline
    calculations

xii. Number of swirl coefficients

4.2.1.2 Preliminary Calculations and Deduced Parameters

Before the velocity triangle distribution and mass averaged performance of the fan can be calculated, a number of parameters must be deduced from the input data. Firstly, the ambient temperature and pressure as well as the rotational speed are converted to base units. Thereafter, the following parameters are calculated :

i.   Fluid density

ii.   Inlet axial velocity (assumed constant and uniform across the fan inlet annulus)

iii. Mass flow rate

iv.   The static pressure at the fan inlet face (also assumed constant and uniform across the fan inlet annulus)

v.   Hub radius

vi.   The radial stations at which the calculations will be performed

4.2.1.3 Axial Exit Velocity Distribution

The iteration for the axial exit velocity is the central and most important part of the program. Essentially, SREE(3)

$$\frac{1}{\rho}\frac{dp_o}{dr} = \frac{c_\theta}{r}\frac{d}{dr}(rc_\theta) + c_x\frac{dc_x}{dr} \qquad 4.2$$

and the general swirl distribution

$$c_\theta = ar^n \qquad 4.3$$

are combined to provide an expression for the axial exit velocity as a function of radius :

$$c_{x_2} = \sqrt{2a\Omega(r^{n+1} - r_h^{n+1}) - R(r)a^2(n+1) + c_{x_2}^2(r_h)} \qquad 4.4$$

where

$$R(r) = \ln\left(\frac{r}{r_h}\right)^2 \qquad for \quad n = 0 \qquad 4.5$$

$$R(r) = \frac{r^{2n} - r_h^{2n}}{n} \qquad for \quad n \neq 0 \qquad 4.6$$

This expression for the axial exit velocity is written in terms of known parameters but must be solved iteratively because of the inclusion of $c_{x_2}(r_h)$ under the square root. A value for $c_{x_2}(r_h)$ is guessed and the corresponding radial distribution of c_{x_2} calculated directly from Equation 4.4. Since the mass flow rate through the fan is known from the specification of the geometry and volumetric flow rate, the compatibility of the axial exit velocity distribution arising from the guessed value of $c_{x_2}(r_h)$ can be audited by integrating the continuity relationship

$$\frac{\dot{m}}{2\pi\rho} = \int_{r_h}^{r_t} c_{x_2} \cdot r\, dr \qquad 4.7$$

over the fan exit plane. The appropriate value of $c_{x_2}(r_h)$ is obtained when inlet and exit mass flow rates concur to within an acceptable tolerance, a value of 0.01% being used in the design calculations.

37

4.2.1.4 Calculation of Flow Parameters

Once the exit swirl velocity distribution and the axial exit velocity distribution have been determined, the distribution of all remaining angles and velocities, pressure rise and efficiency may be calculated.

The unknown angles and velocity vectors are calculated directly from the simple geometric relationships obtained from the velocity triangles of Figure 2.4 and listed in Table 4.2.

The specific work distribution is determined from the Euler work equation which in the case of the rotor only fan simplifies to

$$W(r) = \Omega r c_{\theta_2} \qquad\qquad 4.8$$

The total power absorbed by the fan is the mass averaged value, obtained from the specific work distribution by integrating over the fan exit annulus

$$P_{fan} = \frac{2\pi\rho}{\dot{m}} \int_{r_h}^{r_t} c_{x_2}(r) W(r) . r dr \qquad\qquad 4.9$$

The pressure distributions at the fan exit are calculated from the velocity components as follows :

$$p_{o2} = p_{o1} + \rho \Omega r c_{\theta_2} \qquad\qquad 4.10$$

$$p_{2_d} = \frac{1}{2}\rho\left(c_{\theta_2}^2 + c_{x_2}^2\right) \qquad\qquad 4.11$$

$$p_2 = p_{o2} - p_{2_d} \qquad\qquad 4.12$$

The mass averaged pressures for the fan are then obtained by integrating the distribution over the annulus, ie

$$\overline{p}_{o2} = \frac{2\pi\rho}{\dot{m}} \int_{r_h}^{r_t} c_{x_2} p_{o2} . r . dr \qquad \qquad 4.13$$

$$\overline{p}_2 = \frac{2\pi\rho}{\dot{m}} \int_{r_h}^{r_t} c_{x_2} p_2 . r . dr \qquad \qquad 4.14$$

from which the fan total to total pressure and fan total to static pressures are obtained, ie

$$\Delta p_{o_{tt}} = \overline{p}_{o2} - p_{o1} \qquad \qquad 4.15$$

$$\Delta p_{ts} = \overline{p}_2 - p_{o1} \qquad \qquad 4.16$$

Two non-dimensional pressure coefficients, the total pressure rise coefficient and the static pressure rise coefficient are also calculated :

$$K_T = \frac{\overline{p}_{o2} - p_{o1}}{\frac{1}{2}\rho c_{x_1}^2} \qquad \qquad 4.17$$

$$K_S = \frac{\overline{p}_2 - p_{o1}}{\frac{1}{2}\rho c_{x_1}^2} \qquad \qquad 4.18$$

Note that the velocity used to non-dimensionalise the pressure rise is the inlet axial velocity (ie upstream of the hub), assumed constant. In the case of free vortex designs, the inlet and outlet axial velocities are identical

and the subscript is superfluous. For the general vortex case, the inlet and outlet velocities are different and distinction between the two must be made.

The total to total and total to static efficiencies are calculated as follows :

$$\eta_{tt} = \frac{(\overline{P}_{o2} - P_{o1})_{act}}{(\overline{P}_{o2} - P_{o1})_{th}}$$

4.19

$$\eta_{ts} = \frac{(\overline{P}_2 - P_{o1})_{act}}{(\overline{P}_{o2} - P_{o1})_{th}}$$

4.20

Note that in FANVTX, no total pressure losses are taken into account and the actual (ie real) total pressure rise is identical to the theoretical total pressure rise (ie the Euler total pressure rise), therefore giving a total to total efficiency of 100%. In program FANBLD where total pressure losses are accounted for, the theoretical total pressure rise is given by

$$\Delta P_{o_{th}} = (\overline{P}_{o2} - P_{o1})_{act} + \Delta P_{o_{loss}}$$

4.21

and the total to total efficiency is given by

$$\eta_{tt} = \frac{(\overline{P}_{o2} - P_{o1})_{act}}{(\overline{P}_{o2} - P_{o1})_{act} + \Delta P_{o_{loss}}}$$

4.22

Similarly, the total to static efficiency is given by

$$\eta_{ts} = \frac{(\overline{P}_2 - P_{o1})_{act}}{(\overline{P}_{o2} - P_{o1})_{act} + \Delta P_{o_{loss}}}$$

4.23

It should also be noted that the total to static efficiency as defined above is different to the fan static efficiency as specified by BS848 (Equation 2.22), primarily in the

sense that the total to static efficiency is reduced by
the inclusion of the swirl velocity component, but also
in that the dynamic pressure used in BS848 is based only
on the outer diameter of the fan shrouding and does not
take into account the area reducing effect of a hub shroud.

4.2.1.5 Streamline Shift and Curvature

Streamline shift arises from radial differences in the
axial velocity component between the fan inlet and exit
stations. In order to calculate the streamline shift
through the fan, the mass flow rate between the hub and
each radial station at the fan inlet station is determined
using the equation of continuity. The axial velocity
distribution at the exit station is also known and the exit
mass flow rate as a function of radius is obtained by again
using the continuity equation. The radial positions of a
streamline passing through the fan rotor are established
when the mass flow rates between the hub and two corre-
sponding radial stations at inlet and outlet are identical,
expressed as

$$\dot{m}_{r1} = \int_{r_h}^{r_1} 2\pi\rho c_{x_1}.r\,dr = \dot{m}_{r2} = \int_{r_h}^{r_2} 2\pi\rho c_{x_2}.r\,dr \qquad 4.24$$

The simplified radial equilibrium theory only provides for
the calculation at stations far upstream and downstream of
a blade row. Using the above method, only the total shift
in streamlines between these two stations is determined,
the actual shape of the streamlines and the distance over
which the streamline curvature takes place remaining
unknown.

Actuator disc theory (Appendix E) allows the calculation of the axial velocity field between the far upstream and downstream stations, ie the axial velocity at any radius and axial position may be determined. Once this velocity field has been established, a procedure similar to that of the radial shift described above is used to estimate the streamline shape.

At the far upstream location, the axial velocity profile is constant and the mass flow rate is given by

$$\dot{m}(r) = \pi \rho c_{x_1}(r^2 - r_h^2)$$ 4.25

Selecting a series of radii across the flow annulus at the far upstream station will determine the starting positions for a set of streamlines. Since the axial velocity profile will in general not be constant through the fan, the position of a particular streamline at a downstream station will be given by that radius at which the mass flow rate between the hub and this radius is equal to the mass flow rate between the hub and the original radius at the far upstream station. In FANVTX, the procedure for the calculation of the streamlines is as follows :

    i.   Streamline radii at the far upstream station are selected and the corresponding mass flow rates between the hub and each streamline are calculated.

    ii.   At each pre-selected axial station, the axial velocity profile is calculated using the actuator disc equations.

    iii.   At each axial station, the velocity profile is integrated to give the mass flow rate distribution as a function of radius, ie

$$\dot{m}(r) = \int_{r_h}^{r} 2\pi\rho c_x(r).r\,dr \qquad\qquad 4.26$$

iv.　For a given streamline, the radius is then interpolated from the mass flow rate/radius relationship at the corresponding far upstream mass flow rate.

4.2.2 FANOPT

FANOPT implements the optimisation method of Van Niekerk (1958), adapted for rotor only fans (see Appendix B). The primary limitations and assumptions are that of a free vortex swirl distribution and that the solidity of the fan blading is sufficiently low everywhere to permit the use of free aerofoil lift/drag data, ie no interference effects are present.

The user specifies the following input data :

i.　The number and range of hub-tip ratios to use.

ii.　The range of fan static pressures to use.

iii.　The volumetric flow rate.

iv.　The estimated value of the average drag/lift ratio for the blading $(\tan\gamma_{av})$.

v.　Tip radius.

vi.　Rotational speed.

vii.　An estimated value of the annulus efficiency.

For the specified range of hub-tip ratios fan total to total and total to static efficiencies are calculated from

$$(1 - \eta_{tt})_{avg} = \frac{2}{3} \frac{(\tan \gamma)_{avg}}{\phi_t} \frac{(1 - x_b^3)}{(1 - x_b^2)} + \frac{2(\tan \gamma)_{avg}[\phi_t - \epsilon_h x_b]}{(1 + x_b)} + (1 - \eta_a) \frac{\phi_t}{2\epsilon_h x_b} \qquad 4.27$$

$$(1 - \eta_{ts})_{avg} = \frac{2}{3} \frac{(\tan \gamma)_{avg}}{\phi_t} \frac{(1 - x_b^3)}{(1 - x_b^2)} + \frac{2(\tan \gamma)_{avg}[\phi_t - \epsilon_h x_b]}{(1 + x_b)} \qquad 4.28$$

$$+ (1 - \eta_a) \frac{\phi_t}{2\epsilon_h x_b} + \frac{\phi_t}{2\epsilon_h x_b} \left[1 - 2(\epsilon_h x_b)^2 \cdot \frac{\ln(x_b)}{(1 - x_b^2)} \right]$$

The computations result in a series of constant hub-tip ratio curves, where fan efficiencies (total and static) are plotted against fan total to static pressure rise. Since the desired fan static pressure rise is known, the optimum hub-tip ratio is that which gives the highest efficiency for the specified pressure rise.

4.3 Blade Design

4.3.1 FANBLD

Program FANBLD is used to determine the blading geometry required to achieve the flow turning as prescribed by FANVTX. After the blade shape and size has been established, an estimate of the viscous losses and actual fan efficiency at the design point is also made.

The input to FANBLD is taken almost exclusively from the output of FANVTX and includes the number of radial stations, the number of blades, ambient temperature and pressure, the radial stations across the fan annulus, all the velocity distributions, the relative blade inlet and exit angles and the hub and tip lift coefficients.

The calculation of the blading geometry is separated into two parts, firstly the determination of blading parameters and thereafter the calculation of blade section co-ordinates. The overall procedure is to treat the fan as being made up of a number of separate two dimensional aerofoils at each radial station. Using the velocity and flow angle data from FANVTX and the relationships derived in Appendix C, the radial distributions of camber angle, blade loading factor, solidity, lift coefficient, angle of attack and stagger angle are calculated. The calculation of the blade co-ordinates require only the chord and stagger angle at each radial station. Since almost all standard aerofoil data is presented in terms of non-dimensional co-ordinates normalised with respect to the chord, the blade profile at each radial station is easily scaled to the correct (ie real) size. The scaled profiles are then rotated to lie at the desired stagger angle and stacked about a radial line passing through the centroid of each profile. In the present version of FANBLD, only data for Clark-Y and NASA LS profiles are included although other profile data may easily be added.

The calculations within FANBLD are separated into four phases

i.   Input specification

ii.   Calculation of blading parameters

iii. Efficiency estimate

iv.   Calculation of blade co-ordinates

4.3.1.1 Input Specification

The input data required by FANBLD consists mainly of velocity and angle distributions as calculated by FANVTX,

the only new parameters that the user must specify being the number of blades and the hub and tip values of lift coefficient, ie :

i.   Number of radial stations along the blade length

ii.   Number of blades

iii.   The radial position at each station along the blade length

iv.   Ambient temperature and pressure

v.   Inlet relative flow angle distribution

vi.   Exit relative flow angle distribution

vii.   Inlet axial velocity

viii.   Exit axial velocity distribution

ix.   Exit swirl velocity distribution

x.   Inlet relative velocity distribution

xi.   Exit relative velocity distribution

xii.   Hub and tip lift coefficients

4.3.1.2 Blading Parameters

The primary variables calculated in the Blading Parameter section are the blade chord, angle of attack and stagger angle, necessary to fully define the aerofoil sections and twist of the blade. The calculations are started by first obtaining the mean relative flow angles and velocities;

$$c_{x_m} = \frac{1}{2}(c_{x_1} + c_{x_2})$$

           4.29

$$\tan\beta_m = \frac{1}{2}(\tan\beta_1 + \tan\beta_2)$$

$$w_m = \frac{w_{x_m}}{\cos\beta_m}$$

and the blade loading factor

$$C_L\sigma = 2\left(\frac{c_{\theta_2}}{c_{x_m}}\right)\cos\beta_m$$

at each radial station

From the specified values of hub and tip lift coefficient and the corresponding loading factors calculated above, the blade chords at the hub and tip are determined from the definition of solidity, ie

$$c = \frac{2\pi r(C_L\sigma)}{n_b C_L}$$

Having determined the hub and tip values of blade chord, a linear interpolation for intermediate radial stations is performed to give the radial distribution of blade chord. In the current version of FANBLD, only a linear interpolation is provided for although an exponential or other suitable variation might also be used.

Having established the blade section chords, the solidity, lift coefficient and Reynolds number distributions are determined from the following respective relationships :

$$\sigma = \frac{c n_b}{2\pi r}$$

$$C_L = \frac{(C_L\sigma)}{\sigma}$$

$$Re_c = \frac{\rho w_m c}{\mu}$$

The section angles of attack are obtained from the empirically derived angle of attack vs lift coefficient curves for the selected aerofoil section. In FANBLD, a spline is fitted to this data and for each profile at a given radius, the angle of attack corresponding to the calculated lift coefficient is then interpolated.

Finally, the stagger angle for each profile section is calculated from the velocity triangle relationship

$$\xi = \beta_1 - \alpha \qquad\qquad\qquad\qquad 4.37$$

Note that the stagger angle, ξ, is different to the "blade setting angle", ϕ_{BS}, as used by Venter (1990). The "blade setting angle" is the angle between the tangent to the blade lower surface and the perpendicular to the machine axis, whereas the stagger angle is the angle between the blade chord and the machine axis. These differences are illustrated in Figure 4.4.

4.3.1.3 Blading Efficiency

The expressions for the total to total and total to static efficiencies are given respectively by

$$\eta_{tt} = \frac{(\overline{p}_{o2} - p_{o1})_{act}}{(\overline{p}_{o2} - p_{o1})_{act} + \Delta p_{o\,loss}} \qquad\qquad 4.38$$

$$\eta_{ts} = \frac{(\overline{p}_2 - p_{o1})_{act}}{(\overline{p}_{o2} - p_{o1})_{act} + \Delta p_{o\,loss}} \qquad\qquad 4.39$$

where $\Delta p_{o\,loss}$ is the total pressure loss due to viscosity and secondary flows. Following the practice of Wallis (1983), the total pressure loss is determined from the relationship

$$\Delta p_{o_{loss}} = \frac{1}{2}\rho \zeta w_m^2 \qquad\qquad 4.40$$

where the total pressure loss coefficient, ζ is defined by

$$\zeta = K_{th}\left(\frac{C_D \phi}{C_L \cos^2 \beta_m}\right)_{mean} \qquad\qquad 4.41$$

and the subscript 'mean' indicates that all parameters within the brackets are evaluated at the midspan radius.

K_{th} is the theoretical pressure rise coefficient defined as the Euler (ie ideal) pressure rise non-dimensionalised with respect to the inlet axial velocity :

$$K_{th} = \frac{p_{o_2} - p_{o_1}}{\frac{1}{2}\rho C_{x_1}^2} \qquad\qquad 4.42$$

Following the practice of Wallis (1983), the drag coefficient comprises the summation of profile and secondary components as follows :

$$C_{D,mean} = C_{D,prof} + C_{D,sec} \qquad\qquad 4.43$$

where the secondary drag coefficient is assumed proportional to the square of the lift coefficient, ie

$$C_{D,sec} = 0.018 C_L^2 \qquad\qquad 4.44$$

The drag coefficients are those corresponding to the mean radius profile and angle of attack.

4.3.1.4 Blade Co-ordinates

Standard aerofoil profile co-ordinate data is usually presented in the form of tabulated upper and lower surface co-ordinates, non-dimensionalised with respect to the chord length, the chord lying along the horizontal axis and the leading edge located at the origin. In FANBLD, the calculation of blade co-ordinates involves the scaling of the standard blade profile to user dimensions as well as the stacking of each blade profile around its centroid.

Initially the centroid of the profile in non-dimensional units is calculated relative to the origin. Thereafter, for each fan blade section, the standard profile as well as the co-ordinates of the centroid are scaled to full size.

4.4 Design Discussion

4.4.1 Evaluation of Vortex Distribution and Hub-tip ratio

In order to determine the effects of swirl distribution, the fan static efficiency was computed using FANVTX for a range of hub-tip ratios within the domain 0.2 to 0.5. The volumetric flow rate, static pressure rise, tip radius and rotational speed being kept constant at the design point values. Figure 4.5 indicates the efficiency variation so obtained. During the computations it was found that the range of swirl exponent, 'n', satisfying the given constraints was limited to high negative values in the vicinity of -1, the free vortex case. The primary cause of this limitation is that as the swirl exponent deviates further from the free vortex condition, the greater the radial variation in the axial velocity. As the swirl exponent is reduced (approaching

zero), a situation is soon reached where the axial exit velocity at the tip is approaches zero in an attempt to satisfy continuity. Any further reduction in the swirl exponent will effect an untenable reverse flow. The permissible range of swirl exponent is extended by an increase in hub-tip ratio, but accompanied by a significant decrease in efficiency, Figure 4.5 indicating a 5% efficiency reduction when the hub-tip ratio is increased from 0.3 to 0.5. The efficiency reduction associated with the higher hub-tip ratios is attributable to the fact that for a constant volumetric flow rate, increasing the hub-tip ratio will induce higher through flow velocities and therefore correspondingly higher dynamic pressures. In the expression for the fan total to static efficiency (Equation 4.39), the entire dynamic pressure component is deducted, ie no static pressure recovery is assumed. An increase in the through flow velocity therefore clearly serves to reduce the value of fan total to static efficiency for fixed volumetric flow rate and power consumption.

Two other considerations are worthy of discussion. Firstly, it is evident that the change in efficiency over the range of hub-tip ratio, 0.2 to 0.4 is relatively small, being of the order 1.5%. This would suggest that when designing a fan of the type of interest here, a small sacrifice in terms of efficiency may allow the use of higher hub-tip ratios, with an attendant reduction in blade twist and manufacturing/stress problems.

Secondly, for a given hub-tip ratio, the choice of swirl exponent within the allowable range has very little effect on the efficiency, although the data indicates that an absolute maximum efficiency of 73% is obtained for a swirl exponent -0.9 and not the free vortex case, $n = -1.0$. It is however conceded that there is likely to be little physical

difference between fan blading designed for these respective swirl coefficients, and certainly for the given fan duty and geometry, the free vortex design is appropriate.

Figure 4.6 illustrates the efficiency/pressure rise characteristics obtained from FANOPT when using the design point specifications of volume flow, static pressure rise and rotational speed. For the given characteristics, an annulus efficiency (η_a) of 80 % and a drag/lift ratio $(\tan\gamma)$ of 0.017 was assumed. It should be noted that the annulus efficiency and average drag/lift ratio must be assumed or estimated in the preliminary design phase since blade and annulus details are unknown. However, the values used here are considered connservative by Van Niekerk (1958). In the graph, the fan total to static efficiency is plotted against the total to static pressure rise for hub-tip ratios varying between 0.2 and 0.6.

In the FANOPT calculations, the swirl factor was constrained between the values 0.3 and 1.2 in order to limit the absolute flow angles at the hub to 17° and 50° respectively, since according to Wallis (1983), absolute flow angles in excess of 48° (swirl factor approximately 1.1) lead to very high exit losses.

The same trend as that for the FANVTX calculations (Figure 4.5) is indicated, namely, a decrease in total to static efficiency as hub-tip ratio is increased. However, consequent to the inclusion of annulus and blading losses, lower total to static efficiencies are indicated. It is evident from Figure 4.6 that at low static pressure rise, the low hub-tip ratio designs will provide higher efficiencies. As the pressure rise requirement increases, the low hub-tip ratio configurations cannot attain the higher pressures without exceeding the hub swirl factor limitation.

For the given design point specifications, corresponding to a total to static pressure rise of ±210Pa, the highest static efficiency is obtained for a hub-tip ratio of 0.4, providing 62.7%.

The optimum flow factor calculated using Van Niekerks method (Equation B35, Appendix B) for a hub-tip ratio of 0.4 and hub swirl factor 1.1 is 0.082 as opposed to a value of 0.168 implied by the volumetric flow rate and diameter design contraints. This would suggest that for higher efficiencies, the rotational speed should be increased by factor of approximately 2.

In light of the foregoing, a hub-tip ratio of 0.4 and a free vortex swirl distribution were selected for the design of the candidate fans.

4.4.2 Blade Design

The design point specifications as listed in Table 4.1 and a hub-tip ratio of 0.4 provided the input to FANVTX from which velocity triangle data and mass averaged parameters were obtained. Before proceeding with the design of the blading, the tip flow factor, ϕ_t and the hub swirl factor ϵ_{2h} were given some consideration.

The tip flow factor for the free vortex design and hub-tip ratio of 0.4 is $\phi_t = 0.168$. According to Wallis'(1983) recommendations, a tip flow factor less than approximately 0.2 is acceptable for a single rotor type fan. Wallis also recommends a limit on the hub swirl coefficient of 1.1 for rotors without inlet guide vanes but including exit flow straighteners. A plot of the swirl factor distribution along the blade span is provided in Figure 4.7. In this graph, the swirl distributions for the free vortex, swirl exponent n= -0.9 and a parabolic approximation are shown. The free

vortex swirl factor distribution has a maximum value of 1.1, acceptable in terms of the Wallis (1983) recommendations and resulting in an absolute exit flow angle $\alpha_{2h} = 47.6°$ at the hub. With a view to reducing the exit swirl and associated losses, calculations for the power law form with exponent n=-0.9 were performed. The n =-0.9 design implies a root swirl factor of 1.025 and an exit absolute flow angle of 45.7°. In order to reduce the hub exit swirl still further, a parabolic curvefit having essentially a free vortex distribution from the mean radial station onwards was calculated. This "arbitrary" vortex distribution resulted in a reduction of the exit flow angle to 43.5°. The Euler work equation for single rotor fans (Equation 4.10) clearly indicates the dependency of pressure rise on the exit swirl velocity. Further reductions in the root swirl factor start having a discernible effect on the fan pressure rise and streamline shift. Reducing the root swirl factor is also beneficial in terms of tolerance to distorted inlet flows in that the root section blade loading is also reduced. In light of the foregoing arguments, the parabolic swirl distribution was accepted as the design case and used as input to FANVTX to generate new velocity triangle data.

It is noteworthy that Wallis (1983) strongly advises the use of a stator row for fans requiring a total pressure rise factor (K_T, Equation 4.17) in excess of 4.0. For the given design specification, the total pressure rise factor is of the order 4.5. However, in light of the previously stated constraints, the experimental fans were to be limited to a single rotor configuration, forcing the acceptance of high swirl angles and the associated exit losses.

Two blade profiles were selected for the experimental fans, namely the well known Clark-Y section and the more modern NASA LS series. Since the Clark-Y profile section has been

used extensively in aircraft propellers and fan designs where the pressure rise and flow turning requirements are low, it therefore serves as a control design. The NASA profiles (McGhee et al, (1978,1980)) were selected on the basis of the excellent lift/drag characteristics, promising not only high efficiency but good off-design performance and tolerance to inlet flow distortion. With reference to the lift/angle of attack and lift drag curves illustrated in Figures 4.8 and 4.9, the NASA profiles show a maximum lift coefficient of ±1.6 and a maximum lift/drag ratio of ±85, significantly higher than conventional profiles with corresponding values of the order 1.2 and 60 for the maximum lift coefficient and maximum lift/drag ratio respectively. One of the disadvantages of using the NASA profiles is that no camber variation can be accommodated, whereas with the Clark-Y section, camber changes are effected through a thickness variation although limited by blade passage blockage effects. However, according to Wallis (1983), constant camber blading can be satisfactory for small flow turning angle applications typical of single rotor fans.

The velocity triangle data from FANVTX was input to FANBLD to perform the fan design. Figures 4.10 and 4.11 show the stacked blade profiles for the blades using the Clark-Y and NASA profiles, designated B1 and B2 respectively. Both B1 and B2 fans have a 13% thickness/chord ratio at the root, reducing to 9% at the tip.

4.5 Fan Manufacture

This section briefly describes the manufacture of the B1 and B2 fan blading as well as a hub providing for a hub-tip ratio of 0.4

4.5.1 Blades

FANBLD includes an option whereby the user can specify how many radial stations and the number of blade co-ordinates around the blade profile required to accurately define the geometry for manufacture, within the limits 100 radial stations and 1000 profile points. In the case of the B1 and B2 fans, 50 radial stations and 100 surface points per radial station were used to generate such a data file, subsequently submitted to a CAD/NC system. A three-axis milling machine was then used to cut a wood master blade for each of the B1 and B2 designs (see Figure 4.12) and after polishing and checking the master blades for dimensional accuracy, female glass-fibre moulds were made from the masters.

The structure of the experimental blades consists of a thin glass-fibre shell encasing a plastic foam core, into which an aluminimum stub shaft is secured. In order to check the mechanical integrity of the stub shaft/foam bond, a sample blade was tested to destruction in a specially designed jig. The load required to pull the stub shaft out of the foam core was found to be approximately 29000 N, a value far exceeding the anticipated centrifugal loads and indicating a safety factor of approximately 3.

The mass of the eight blades for each of the B1 and B2 designs was measured and the relative positions around the hub optimised using the EXCHANGE algorithm of Sinclair et al (1993). Upon preliminary testing in the fan test facility, no excessive vibrations were encountered and no further balancing of the rotor was attempted.

The blades were designed such that the root section was perpendicular to the stub shaft axis (ie a straight "cut-off") so as to allow for a wide range of different blade angle settings. Consequently, the gap between the blade root

section and the hub was excessively large and resulted in root leakage. To alleviate this problem, soft wood "root seals", contoured to the root profile were cut and fixed to the blade roots, effecting the desired sealing but still allowing for blade angle variation (See Figure 4.13).

The angular positions of the B fan blades were set using the stagger angle of the root section, referred to the drive shaft axis. The rapid and accurate setting of blade angles was facilitated by means of special protractors shaped to the B1 and B2 root section profiles as illustrated in Figure 4.14.

4.5.2 Hub

A hub for the B fans was designed and constructed with features to expedite tip clearance and blade angle adjustment, as shown in Figure 4.15. The blade stub shaft passes through a threaded collar with the lip on the stub shaft butting up against the top surface of the collar. Tip clearance is adjusted by screwing the collar up or down to the desired height with the stub shaft secured by means of two lock nuts.

The hub was also designed to accommodate a hemispherical nose cone, moulded in glass-fibre, as well as a wooden flat plate so as to establish the advantages or otherwise of streamlined nose shapes.

5 EXPERIMENTAL EVALUATION

The performance of the B fans was evaluated by experimentally measuring the pressure, efficiency and power consumption characteristics as functions of the volumetric flow rate and comparing to that of the V fan. A fair and meaningful comparison was ensured by using the same test facility and experimental procedure as that described by Venter (1990). Initially, the test rig and data acquisition system was qualified for use by measuring the V fan performance characteristics, and comparing these to the measurements of Venter (1990). Thereafter, a comprehensive series of tests on both B fans was performed. In this chapter, the test facility and instrumentation are described, after which the experimental results are presented and discussed.

5.1 Test Facility and Instrumentation

5.1.1 Test Facility

The test facility (Figure 5.1) conforms to the British Standards 848 fan test code with the capability to characterise fans with a maximum rotor diameter of 1.600 m. The test facility was designed to allow the testing for any combination of free or ducted inlet/outlet (type A, B, C and D test). Since type A tests are relevant to this work, only features applicable to these tests are described.

A calibrated inlet bell-mouth is used to determine the volumetric flow rate through the system (item 1. in Figure 5.1). The average inlet diameter of the section in which the pressure tappings is installed is 1.008 m with a maximum deviation of 2 mm.

An auxiliary fan (item 5) is installed directly downstream of the throttling device (item 3), which is used to counteract pressure losses due to the various components in the flow system. The auxiliary fan is six bladed and is attached directly to the shaft of an 11 kW electric motor situated in the main flow stream. The rotor has a 1.540 m diameter and all blade angles are pre-set to 24°.

Flow straighteners are either of egg-grate or radial blade design in accordance with BS848. Two flow straighteners (item 2) are mounted on either side of the throttling device, with the third straightener (item 6) located directly downstream of the auxiliary fan. The latter is intended to eliminate the swirl component of velocity introduced by the auxiliary fan.

A transformation section is required to connect the calibrated bellmouth to the test facility. Two transformation pieces convert the round ducts to square and back to circular to accommodate the flow throttling device. Two transformation pieces are also used to enlarge the channel diameter from 1.500 m to 1.550 m and then back to 1.500 m to accommodate the auxiliary fan. The last transformation piece is a diffuser ensuring an even distribution of air entering the settling chamber, after which a set of flow guide vanes are installed which distribute the air flow more evenly.

The plenum chamber (item 8) is constructed of galvanised sheet metal panels with inside dimensions 4.000 m x 4.000 m x 7.000 m. A set of stainless steel mesh screens (item 9) are installed at the locations specified by BS848. Access to the inside of the chamber is obtained via two air tight doors, one upstream and the other downstream of the wire mesh screens. The outlet of the settling chamber is fitted

with a square opening, 2.500 m x 2.500 m through which fan inlet casings are installed for free inlet characteristic tests.

An hydraulic power pack (item 11) is used to rotate the model test rotors (item 10), having a maximum rated output of 10 kW at 750 rpm. The rotational speed is fully variable at all power settings.

5.1.2 Instrumentation

A schematic diagram indicating the location of the various transducers and test instrumentation is presented in Figure 5.2

Höttinger PD1 inductive differential pressure transducers with a range -1000 to +1000 Pa are used to measure the pressure drop across both the bellmouth and the plenum chamber. A Höttinger T2 (resistive full bridge type) torque transducer with a nominal range -500 to +500 Nm is used to measure the torque. Input signals from all the transducers are amplified by means of an Höttinger KWS 3073 bridge amplifier over the range -10 V to +10 V. The calibration of these instruments is described in Appendix E.

The rotational speed of the fan is measured by means of a simple magnetic pick-up sensor connected to a dual output frequency counter. The first output is a digital display used to adjust the rotational speed whilst the second is a linear voltage output measured by the computer. The calibration of this unit is described in Appendix E.

Output voltages from the bridge amplifier (related to the fan inlet pressure, inlet bell-mouth pressure drop and shaft torque) in addition to a voltage related to the rotational speed are transmitted to an Olivetti M21 personal computer.

Real time voltage inputs are displayed graphically so as allow the test operator to observe and avoid any transient effects. Once steady state conditions are achieved, 500 voltages are measured at a sampling interval of 20 ms. The average of these is calculated and saved to disk.

5.2 Test Procedure and Data Processing

5.2.1 Test Procedure

For all tests, the rotational speed was held constant at the design point value of 750 rpm (within ±2 rpm), whilst the volumetric flow rate and torque were varied over the entire operating envelope of the fan.

The procedure for measuring the performance of the fan is as follows :

i.   Connect all transducers and pressure tubes and zero the bridge amplifier.

ii.   Ensure that both doors to the plenum chamber are closed, check the test fan rotor for clearance within the inlet casing and that the fan support stand is secure.

iii.   Set the throttle to the fully closed position.

iv.   Start the auxiliary and model fans.

v.   Adjust the speed of the test fan until a steady 750 rpm is maintained and take the data point.

vi.   Adjust the throttle valve to the next setting and repeat from (v.) until the full range of settings have been measured.

The ambient pressure and temperature was measured before and after each test and the average of the two readings taken as the test temperature. The thermometer used to measure the ambient temperature was checked against a calibrated thermocouple and found to under-read by $\pm 1.5 °C$. Temperature values reflected in the data files are corrected by this amount. No noticeable difference between the temperature inside the plenum chamber and the ambient value was observed, as long as sufficient time for stabilisation was allowed (± 10 minutes running before taking measurements).

5.2.2 Data Processing

The test procedure as described above results in a data file, stored on the computer hard disk, containing the bell-mouth pressure drop, fan static pressure, torque and rotational speed for each setting of the throttle valve. This data, in addition to the ambient temperature and pressure is used to deduce the fan performance maps by means of program FANDAP.

In FANDAP, all the data from a test is scaled to the reference temperature and density ($20 °C$ and 1.2 kg/m^3 respectively), after which the bell-mouth pressure drop is converted to the corresponding volumetric flow rate and the power deduced from the torque and the rotational speed. The fan static efficiency is calculated and all data is stored in a format conducive to plotting the performance maps. FANDAP and sample calculations outlining the data processing are described in Appendix D.

5.3 Experimental Results

The experimental measurement of the V and B fans was performed in two phases :

i.   Facility and instrumentation qualification using the V fan.

ii.   Measurement of the B fan chracteristics.

5.3.1 Facility Qualification

In order to qualify the test facility for measurement of the B fan characteristics, six tests on the V fan were conducted. The objective was to establish a base line for comparison by repeating the tests of Venter (1990).

The V fan with the hub plate in the downstream location and blade angle settings of 16° at the tip was chosen as the reference configuration against which the B fans would be compared, since in accordance with the findings of Venter (1990) and Van Rhyn (1993), this configuration provided the highest efficiency at the design point flow rate and pressure rise.

However, during this qualification testing, some problems were encountered. Firstly it was discovered that the inlet casing was badly out of round which made setting the tip clearance to the nominal 3 mm impossible. Secondly, the shaft couplings and bearings of the fan drive train were found to be worn. Consequently, the inlet casing had to be filled with body putty and reshaped to the original 1.542 m nominal diameter and during which time, the bearings and couplings of the drive train were replaced.

After this rebuild, the rotational "no-load" torque of the fan drive system was measured by running the fan drive system (without any fan rotor attached) at the design point speed of 750 rpm. During these rotational tests, a number of spurious or extraneous torques were measured, ranging from

63

between 2.0 and 5.0 Nm initially, but increasing to approximately 7.0 Nm when the heavy B fan hub was attached. The excessive 7.0 Nm "no-load" torque measured with the B fan hub in situ was attributed largely to windage and pumping effects. Since this hub would be used in conjunction with either the nose cone or flat plate, thereby preventing air flow through the hub, this reading was disregarded as a true "no-load" value. In an attempt to discover the causes and eliminate the problem, the drive system was stripped and rebuilt a number of times with particular attention being paid to shaft alignment and coupling play. However, both the existence and variation of these secondary torques persisted and whilst plausible causes such as excessive bearing friction arising from over-greasing or misalignment, shaft coupling rubbing friction, or a torque transducer malfunction were suggested, the exact nature of the problem was not established.

For the sake of consistency, a constant torque value of 2.0 Nm (ie the lowest measured) was subtracted from all fan performance torque readings and is reflected in all the power and efficiency characteristics presented in this thesis.

Another problem was encountered with the V fan, namely the setting of the blade angles. The blades were set at the tip using an angled plate clamped in a vise (see Figure 5.3). The angle of the setting plate was positioned with the aid of a digital protractor and using the flat surface of a marble measuring table as a horizontal reference. However, due to non-uniformities in the shape of the tip sections, there is some doubt as to whether all the blades were set at the correct angle. Additionally, the shaft of one of the fan blades was slightly bent, causing the tip to stand proud of the measuring plate, further complicating the setting of the blade angle.

5.3.2 V Fan Characteristics

The first qualification test with the V fan was conducted without the hub plate. Figures 5.4, 5.5 and 5.6 are the measured fan pressure rise, power and efficiency characteristics for this configuration, compared to the data of Venter (1990). The pressure characteristics show good agreement, significant differences apparent only at the higher volumetric flow rates. In contrast, the power consumption characteristic indicates a nearly constant offset of 0.215 kW, corresponding to a torque value of 2.75 Nm, and increasing to 6.412 Nm at the higher volumetric flow rates. The efficiency characteristic initially shows good agreement with that of Venter but starts deviating from a flow rate of 10 m^3/s onwards. The measured fan static efficiency at the design point (16 m^3/s) is 52% . Venter obtains a maximum efficiency value of 55.54% at the design point 16 m^3/s.

Figures 5.7, 5.8 and 5.9 depict the performance characteristics of the V fan with hub plate installed and contain the data for the five tests performed on the V fan in this configuration. The fan static pressure chracteristic, Figure 5.7, indicates good data repeatability for the pressure measurement, although the data for test 5 is marginally higher than that for the other tests. Similarly, the power consumption characteristic also indicates good repeatability with the exception of test 5, a manifestation of the torque offset problem discussed previously. In this particular case, the data points lie substantially above those for the other tests and show an almost constant deviation of ±350 W, corresponding to a torque of 4.5 Nm at the design point speed of 750 rpm. It should be noted that the "no-load" 2.0 Nm has already been deducted from all the data in these tests.

Of the five V fan tests, tests 1 and 2 were performed prior to the modification to the inlet casing and the drive train, whereas tests 3, 4 and 5 were performed afterwards. With the exception of test 5, all the data show good repeatability, suggesting that the modifications did not alter the test facility characteristics significantly.

Since the efficiency is deduced from both the pressure and power characteristics, error in either parameter will be reflected in the efficiency characteristics. Test 3 was conducted without the auxiliary fan and therefore does not cover the entire operating range of volumetric flow rate. Whilst the pressure and power consumption values for this test fall only slightly below the mean, the efficiency deduced from these data shows significant deviation from the rest of the efficiency values, being ±3% at 16 m^3/s.

In light of the above it was decided to discard tests 3 and 5, and use the remaining tests as the datum. Figures 5.10, 5.11 and 5.12 show these data superimposed on a least squares polynomial curve fit. The maximum efficiency obtained is 53.4% at a flow rate of 14.89 m^3/s, whereas at the design point, the efficiency obtained is 53.1%

Figures 5.13, 5.14 and 5.15 present a comparison between these curve fits and Venters data. The pressure characteristics display a difference at and around the design point flow rate (16 m^3/s), being of the order 10 Pa.

The power consumption comparison reflects greater differences at the two extremes of the flow rate range, although near the design point, the agreement is very close.

The efficiency characteristic, Figure 5.15, includes three sets of data. The first curve is the efficiency characteristic plotted from the data presented in Venters thesis. However, there appears to be an inconsistency in Venters

efficiency calculations, since if the efficiency is computed from his pressure and power data, the resulting characteristic (denoted "Venter (mod)" in Figure 5.15) indicates lower efficiencies than the characteristic presented in his thesis. The efficiency characteristic plotted from the experimentally measured data (denoted "Bruneau") follows Venters modified curve closely, especially for flow rates in excess of 10 m^3/s. Venters (original) value for peak efficiency is 57.2% at 15.25 m^3/s with a design point efficiency of 57.0%. The modified data suggests a peak efficiency of 54.8% at a volumetric flow rate of 15.33 m^3/s and a design point value of 54.6%. The corresponding values for the experimentally measured data are 53.4% at 14.89 m^3/s, and 53.1%.

5.3.3 B Fan Characteristics

As described previously, the B fans were designed to include a hemispherical nose cone. However, in view of the fact that Venters model fan and the full-scale fan are used without any form of nose fairing, tests without the nose cone were also performed. Furthermore, in order to allow for tip clearance and blade angle settings, the root section of the B fan blading was made straight, resulting in large clearances between the blade root section and the hub. In order to reduce root clearance losses, wooden root seals (see Figure 4.13) were made and installed. As a result, three configurations for testing were possible, namely :

    i.   nose cone with open roots

    ii.   nose cone with sealed roots

    iii. flat plate with sealed roots

The objective of the first test series conducted on the B fans was to establish the effect of the nose cone on performance. The performance characteristics of both the B1 and B2 fans were measured for nose cone and flat plate configurations, with and without the root seals. Figures 5.16, 5.17 and 5.18 present such a comparison of B1 fan characteristics without root seals. For the sake of clarity, only two stagger angle settings are plotted although the indicated trends were similar for intermediate stagger angles. Apparent from these graphs is the small effect of the nose cone on the pressure, power and efficiency characteristics. Measurements conducted with the root seals in place also indicated no significant nose cone effect on fan performance, confirmed by corresponding measurements using the B2 blading.

The inclusion of root seals has a marked, positive effect on fan performance. Figures 5.19, 5.20 and 5.21 show a comparison of B2 fan characteristics, with and without root seals at a stagger angle of 59°. In this particular case, the nose cone was included. The pressure characteristic shows that root seals result in a higher pressure rise over the entire operating envelope, accompanied by a higher power absorption. At a design point flow rate of 16 m^3/s, the fan static pressure rise is 227 Pa for the sealed root case, as opposed to 191 Pa for the open root, with power consumptions 6.151 kW and 5.576 kW respectively. However, the nett effect on the fan static efficiency is a substantial improvement over the entire operating envelope, most significant at the higher flow rates. At the design point, the sealed root yields a fan static efficiency of 58.7% whilst the open root provides 54.4%. Peak efficiencies occur for both cases at approximately 13 m^3/s, providing 59.8% and 55.5% for sealed and open roots respectively.

The reference power characteristic for the V fan (Figure 5.12) reveals a peak power marginally over 6 kW. In order to compare the B1 and B2 designs to the V fan, the stagger angle resulting in similar maximum power consumption was selected as B fan datums. For comparative purposes, the B fan reference configurations include both root seals and nose cone. In the case of the B1 fan, the datum stagger angle is 63°, whilst that for the B2 fan is 59°. Figures 5.22, 5.23 and 5.24 compare the reference V, B1 and B2 characteristics.

The most noticeable feature of the pressure characteristic, Figure 5.22, is the relatively steep gradient $\Delta p/\Delta \dot{Q}$ of the B fans as compared to the V fan. This implies the B fans are less sensitive to pressure load fluctuations, ie for a given pressure load change, the volumetric flow rate change for the B fans will be less than that for the V fan. At the design point volumetric flow rate of 16 m^3/s, the B1 and B2 pressure rise is almost the same, being 224.7 Pa and 227.2 Pa respectively, whilst that for the V fan is 211.1 Pa.

Figure 5.23 indicates that the B fans have somewhat more peaked power characteristics than the V fan. For the given stagger angle settings, the B1 and V fans have almost identical power consumptions at the design point flow rate. Peak power consumptions for the B1 and B2 fans occur at lower volumetric flow rates than that of the V fan, being 6.144 kW at 12.75 m^3/s and 6.295 kW at 13.75 m^3/s respectively. The V fan peak power consumption of 6.205 kW occurs at the design point flow rate of 16 m^3/s.

Figure 5.24 reveals that up to a volumetric flow rate of 18.5 m^3/s, the B fans are more efficient than the V fan. The B1 design point efficiency is 61.84% whilst that for the B2 fan is 59.16%. The peak efficiencies for the B fans occur

at the same volumetric flow rate of 14.5 m^3/s being 62.98% and 60.14% respectively. In contrast, the V fan has a peak efficiency of 53.42% at 14.89 m^3/s and a design point efficiency of 53.08%

A complete set of B fan characteristics for a range of different blade stagger angles and the reference configuration (nose cone and root seals) are presented in Figures 5.25 to 5.33.

5.3.4 Discussion of the Experimental Results

From the characteristics presented above, it is initially apparent that B fan performance is superior to V fan. However there are a number of mitigating factors which warrant discussion.

Firstly, the problems of torque offset reduce the general validity of the power and efficiency data in that uncertainties with regard to the absolute values remain. However, the fact that a consistent torque offset of 2.0 Nm was deducted for both V and B fans would suggest that at least in a relative sense, the comparison is both conservative and fair. Indeed, given that the highest torque offsets were measured with the heavy B fan hub, it is possible that subtracting only 2.0 Nm from the B fan torque data discounts the actual attainable efficiency.

It should also be noted that the surface finish of the model V fan blades is much rougher than that of the B fans, implying extra losses not associated specifically with the design itself. Furthermore, the V fan model blades are not exact replicas of the full scale units and therefore, the measured test data cannot be extrapolated directly to the operational fans.

The blade angle setting difficulties associated with the V fan will have contributed to discrepancies in the pressure characteristics measured here, and that of Venter (1990). In his thesis, Venter measured the V fan pressure characteristics for a range of blade setting angle, for which the indicated sensitivity is of the order 11.5 Pa per degree at the design point flow rate. With the given procedure for setting the V fan blade angles and the variation in tip profiles of the model blading, it is unlikely that an accuracy of better than ±0.5 degrees is possible. Nonetheless, the small data spread of the measured V fan pressure characteristics (Figure 5.7) would suggest that the blade angle setting was consistent, since for the five tests presented, the blade angles were reset three times.

Another factor affecting the accuracy of the measured characteristics is the axial placement of the fan rotors within the inlet shroud. The rig supporting the drive train and the rotor is not connected to the fan inlet shroud, the axial placement of the rotor being effected by moving the entire rig backwards or forwards to the designated position. The fan inlet shroud is bolted to the plenum chamber wall which is constructed of thin galvanised sheet steel. Consequently, this structure is not very rigid and on operating the test fans, the decrease in pressure within the plenum chamber causes the plenum chamber wall (and therefore the inlet shroud) to move away from the fan. Although prior to testing, the axial position was always set such that the trailing edge tips of the fan blades were 40 mm within the shroud, this position would vary during a test. This situation was particularly true of the B fans whose pressure characteristics are significantly higher than that of the V fan over most of the operating envelope, especially at the lower volumetric flow rates.

Notwithstanding the issues discussed above, both V and B fans were tested in the same test facility as that used by Venter (1990). Whilst it is possible that the performances of both the V and B fans are not accurately reflected in an absolute sense, the relative performances are indicated.

6 CONCLUSIONS AND RECOMMENDATIONS

6.1 Conclusions

A design methodology for rotor only, ducted axial flow fans has been developed and used to design two experimental fans. It was found that for the prescribed geometric dimensions and operating point conditions of 210 Pa fan static pressure rise and 16 m^3/s volumetric flow rate, the free vortex swirl distribution was appropriate. Although alternative swirl distributions were considered, significant deviation from the free vortex case is only feasible with high hub-tip ratios (of the order 0.5). As a consequence of the low volumetric flow rate of the design specification and the corresponding low axial through flow velocity, deviations from the free vortex case result in axial velocities at the blade tip approaching 0 m/s.

When the tip diameter is fixed and the volumetric flow rate specified, hub-tip ratio has a substantial effect on fan performance in that static efficiencies at low static pressure rise are higher for low hub-tip ratio configurations. However, the low hub-tip ratio designs are unable to deliver the higher static pressure rises without excessive root swirl and associated exit losses. The optimum hub-tip ratio satisfying the design constraints was determined to be 0.4

The scale model V fan and the experimental B fans were tested in a test facility conforming to British Standards 848 Type A and the relative performances compared. At the design point flow rate and nominal power consumption of 6.0 kW, the B fans indicate higher fan static efficiencies than the V fan, namely 61.84%, 59.16% and 53.08% for the B1, B2 and V fans respectively.

The fan static pressure rise is also higher for the B fans at the design point, respectively 224.7 Pa, 227.2 Pa and 211.1 Pa for the B1, B2 and V fans.

The inclusion of a faired nose cone for the B fans had no significant effect on the performance of the B fans, the performance characteristics for the B fans including the hemispherical nose cone and flat plate being identical for all practical intents and purposes.

The sealing of the B fan root sections provided marked performance improvements over the unsealed case, being of the order 36 Pa for the fan static pressure rise and 4.3% for the fan static efficiency. The power consumption for the sealed configuration was however slightly higher at 6.151 kW, as opposed to 5.576 kW for the unsealed case.

The B2 fan blades which utilise NASA-LS series aerofoil sections show marginally lower performance in terms of fan static efficiency and fan static pressure rise than the B1 blading incorporating the Clark-Y section. The probable reason is due to low values of design lift coefficient and the fact the NASA section blades could not be tailored in terms of camber. The full effect of the high lift/drag characteristics of this section will most likely become apparent under conditions of highly distorted inlet flows.

The predicted total to static efficiency for the B fans using the Van Niekerk (1958) method is 62.7% with a corresponding total to static pressure rise of ±211 Pa. This compares favourably with the measured efficiency and pressure rise of the B fans, namely 61.84% and 224.7 Pa for the B1 fan, and 59.16% and 227.2 Pa for the B2 fan.
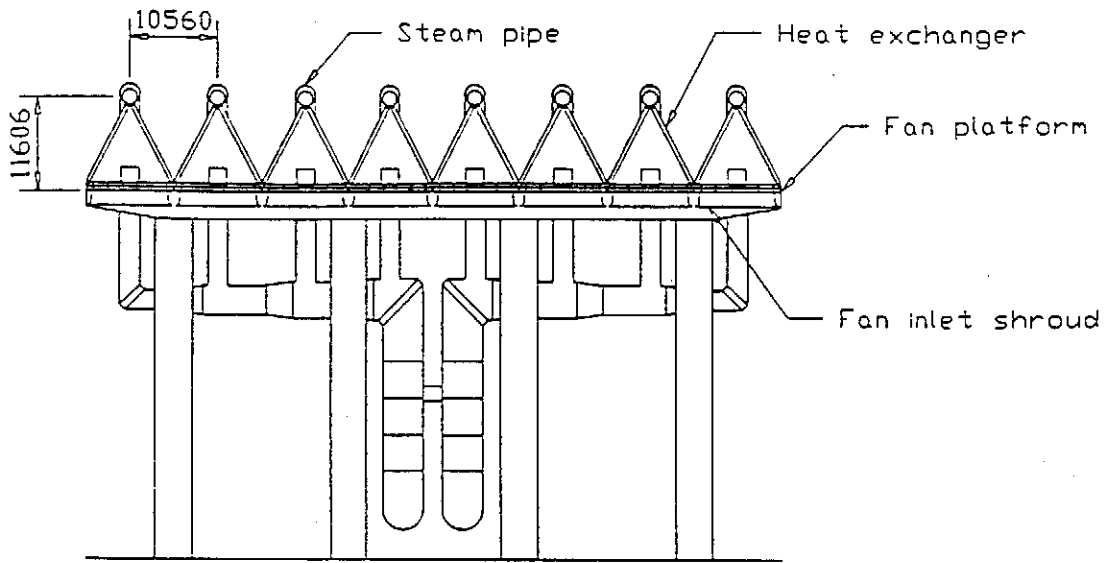
6.2 Recommendations

In view of the fact that one of the motivations for this study was to design a fan with an increased tolerance to distorted inlet flows, tests to establish the performance of the B fans under these conditions should be conducted.
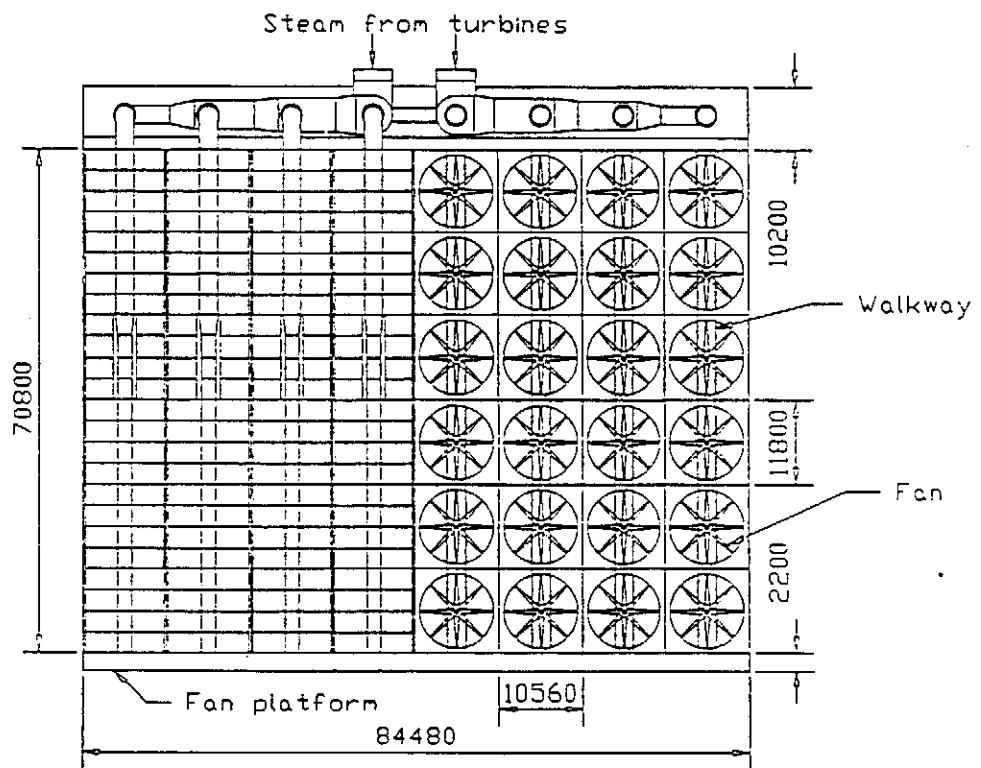
As discussed in Chapter 5, there is some doubt as to the validity of the absolute values of the measured torque and efficiency as a consequence of spurious torques measured under conditions of no load. The exact nature of the torque offset problem should be established and remedial action taken.

There also remain uncertainties with regard to the V fan blade setting angles. The method used by Venter (1990) and the author is operator dependent and a more accurate and repeatable method should be implemented.

The stiffness of the plenum chamber wall is also a possible cause of data inaccuracy, resulting in the axial placement of the fan rotor within the shroud changing with various plenum chamber pressures. Modifications to strengthen and stiffen the plenum chamber wall should be performed.

10560

11606

Steam pipe

Heat exchanger

Fan platform

Fan inlet shroud

Frontal elevation

Steam from turbines

70800

10200

Walkway

11800

Fan

2200

Fan platform

10560

84480

Plan

Figure 1.1 Full scale installation (from Venter (1990))
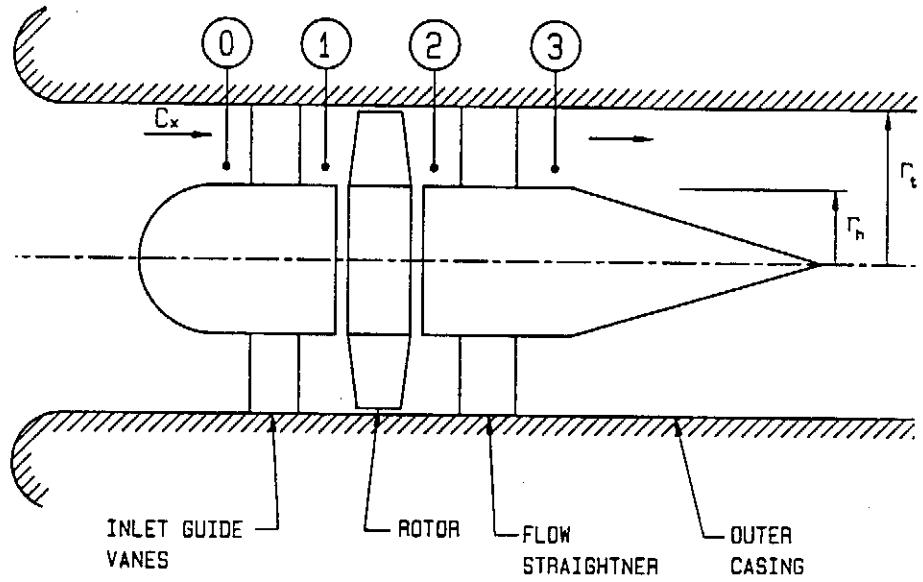
Figure 2.1 General fan arrangement

r_h = HUB RADIUS
r_t = TIP RADIUS
r_m = MEAN RADIUS
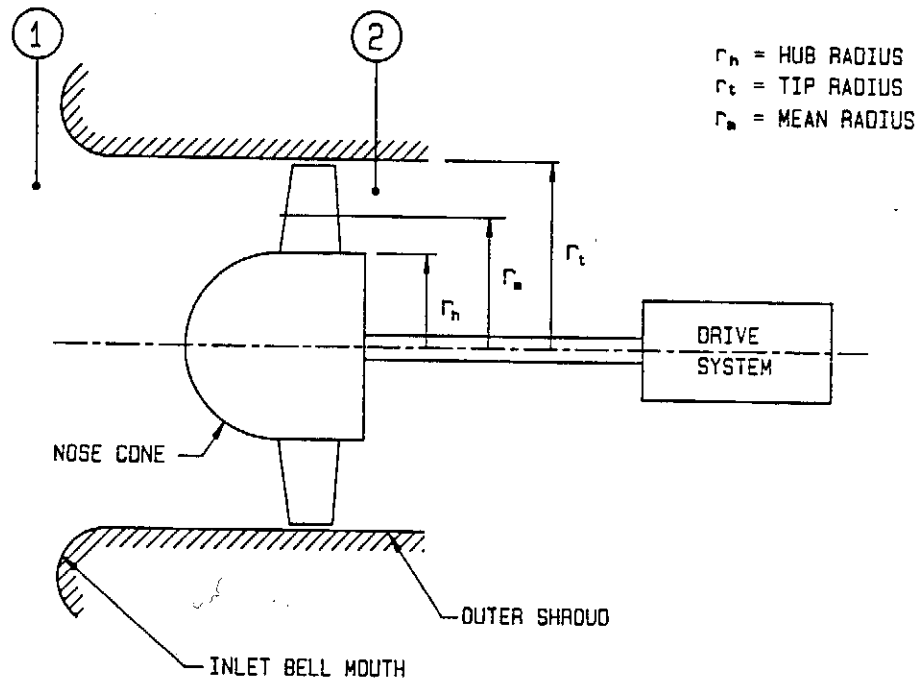
Figure 2.2 Rotor-only fan arrangement

77

INLET GUIDE VANES

ROTOR

FLOW-STRAIGHTNER
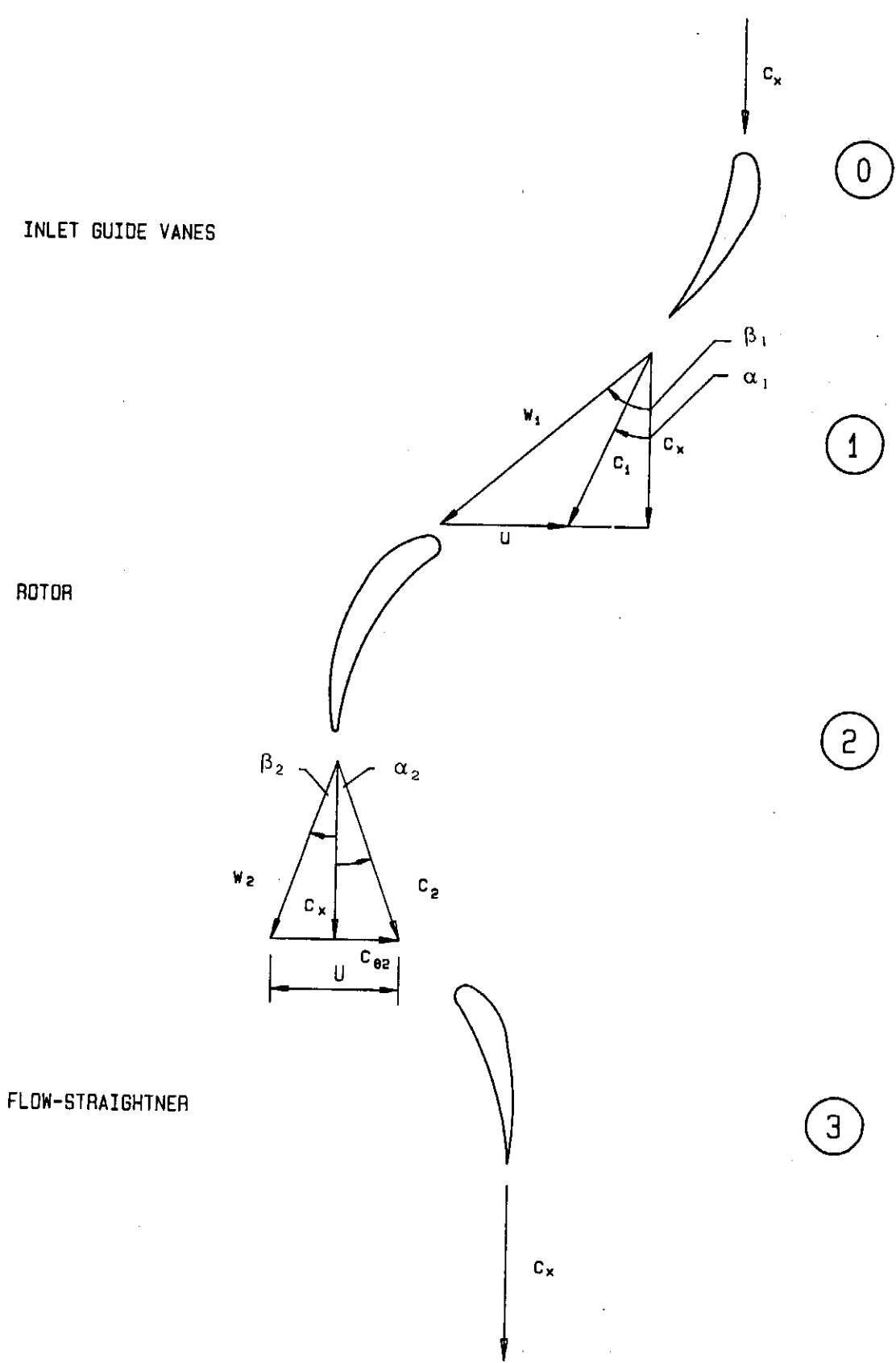
Figure 2.3 Velocity diagrams for general fan arrangement
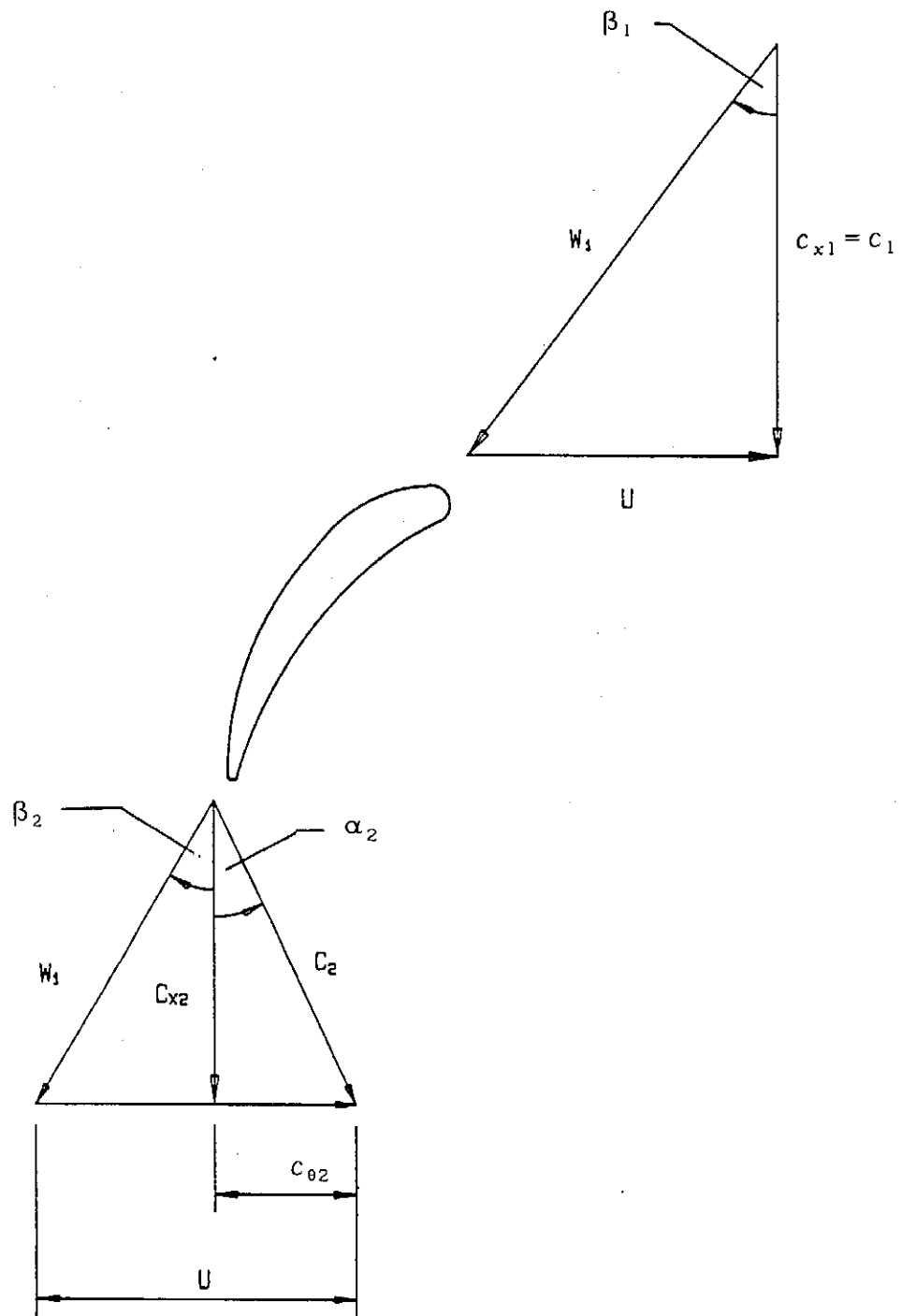
Figure 2.4 Velocity diagram for rotor-only arrangement

Absolute flow angle	$\alpha_{1,2}$
Relative flow angle	$\beta_{1,2}$
Blade speed	U
Absolute velocity	$c_{1,2}$
Relative velocity	$w_{1,2}$
Swirl velocity	$c_{\theta_{1,2}}$
Axial velocity	$c_{x_{1,2}}$

Table 2.1 Velocity triangle nomenclature
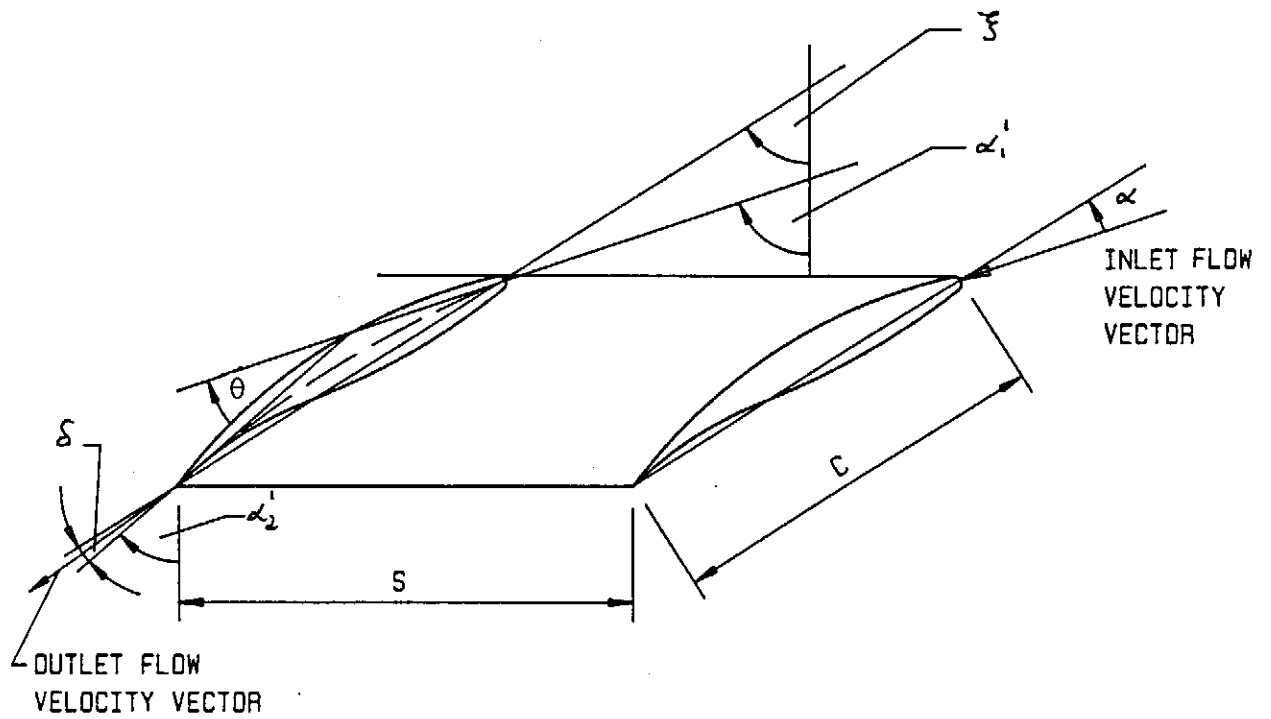
Figure 2.5 Cascade nomenclature

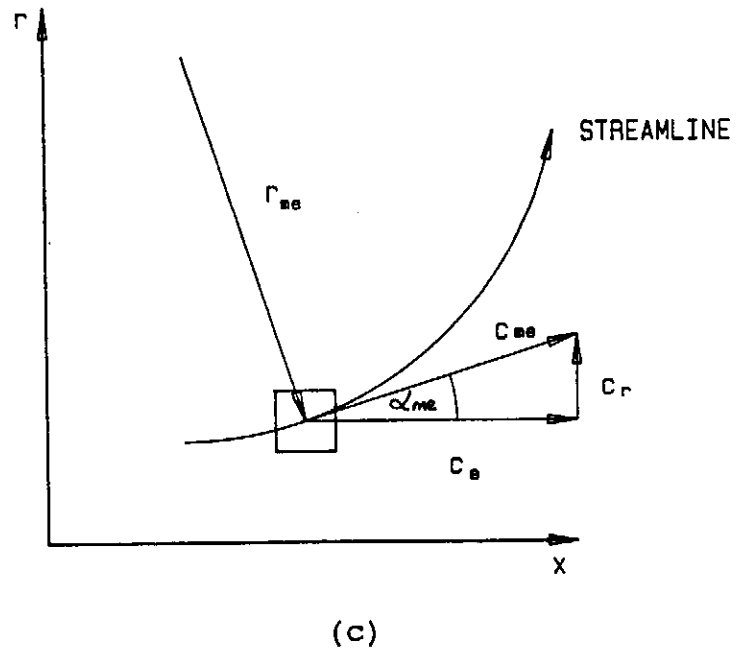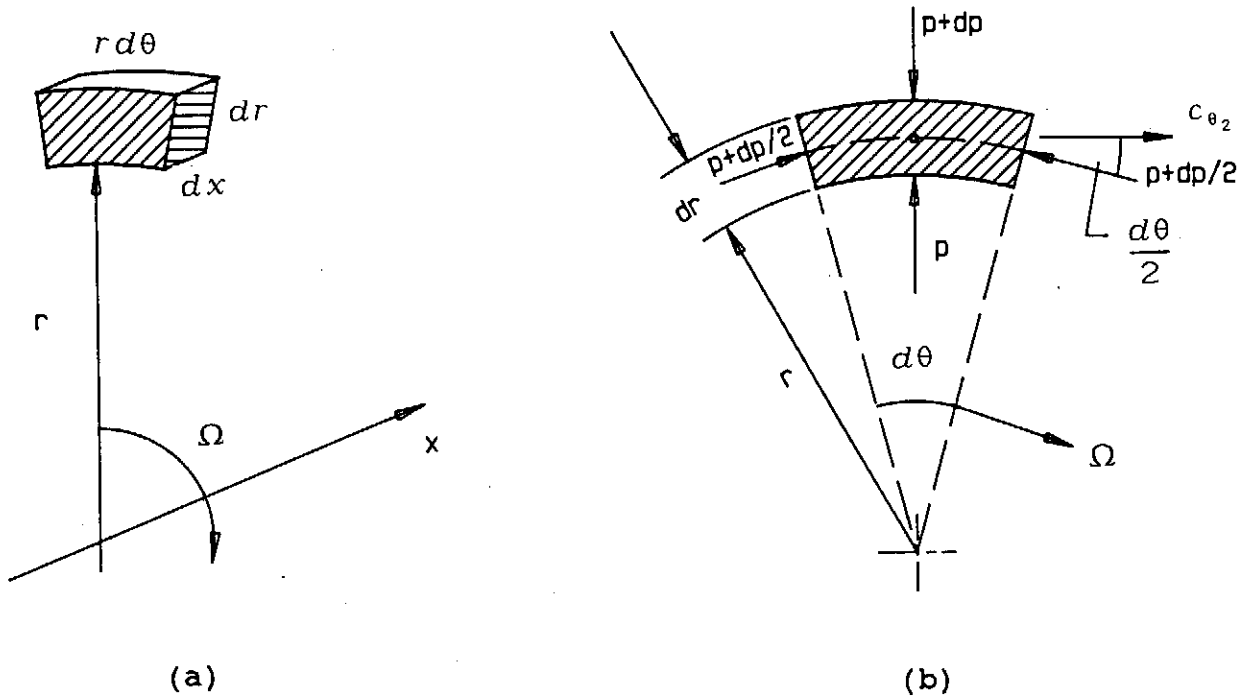| Chord	c
Pitch	s
Stagger angle	ξ
Deviation angle	δ
Angle of attack	α
Camber line inlet angle	α'_1
Camber line exit angle	α'_2
Camber angle	θ

Table 2.2   Cascade nomenclature

Figure 3.1 Radial equilibrium factors

(a) fluid element in turbomachine flow field

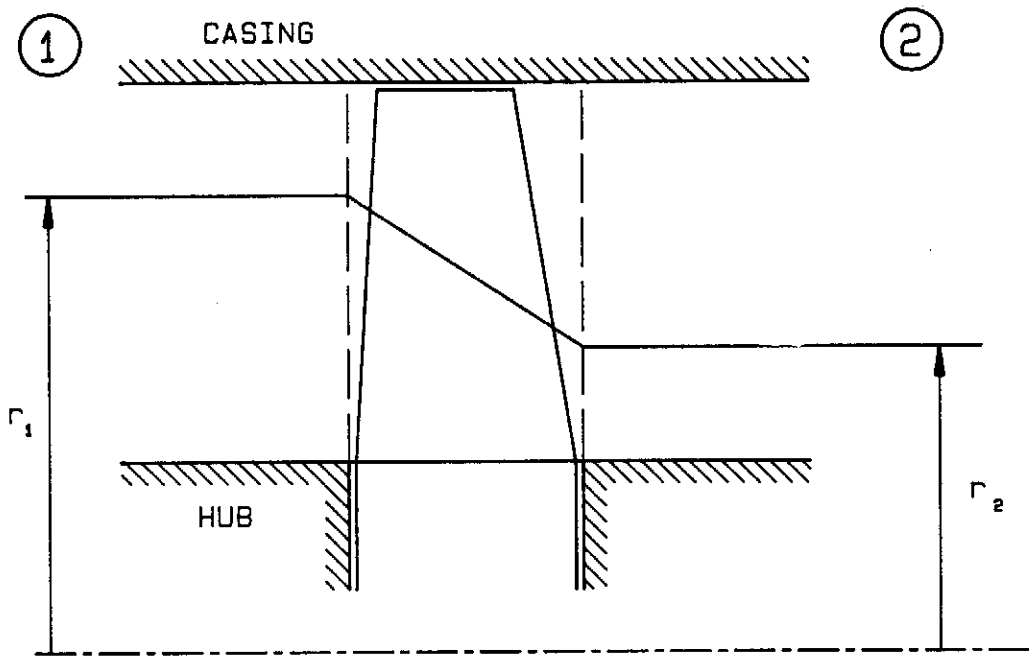(b) rotational plane $(r - \theta)$

(c) meridional plane $(r - x)$
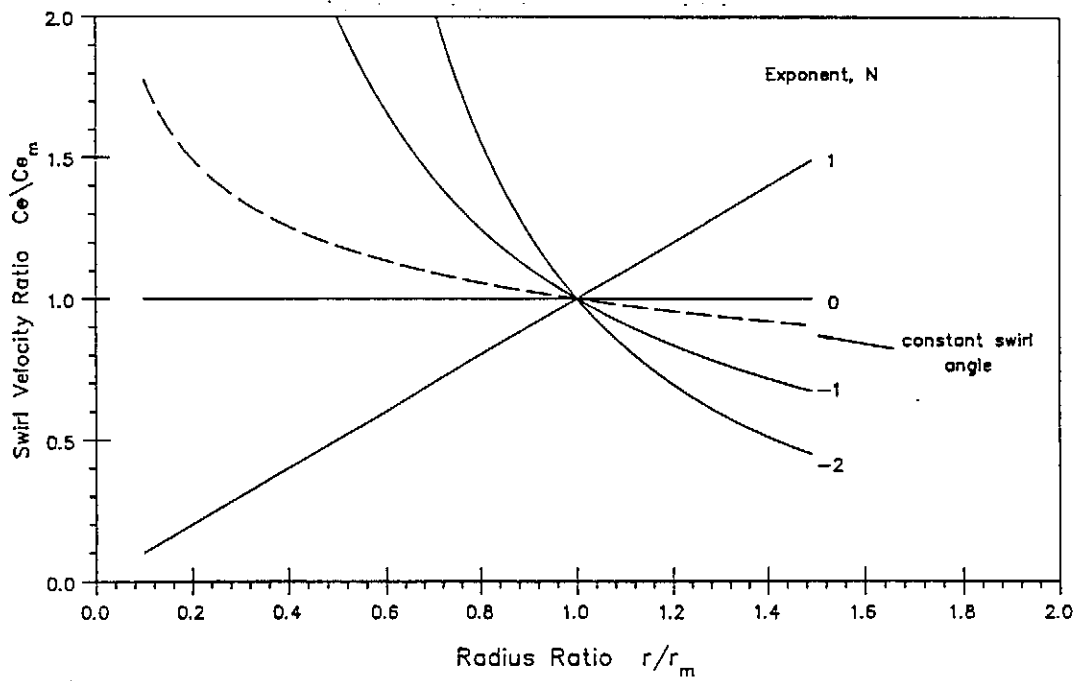
Figure 3.2 Radial flow assumption

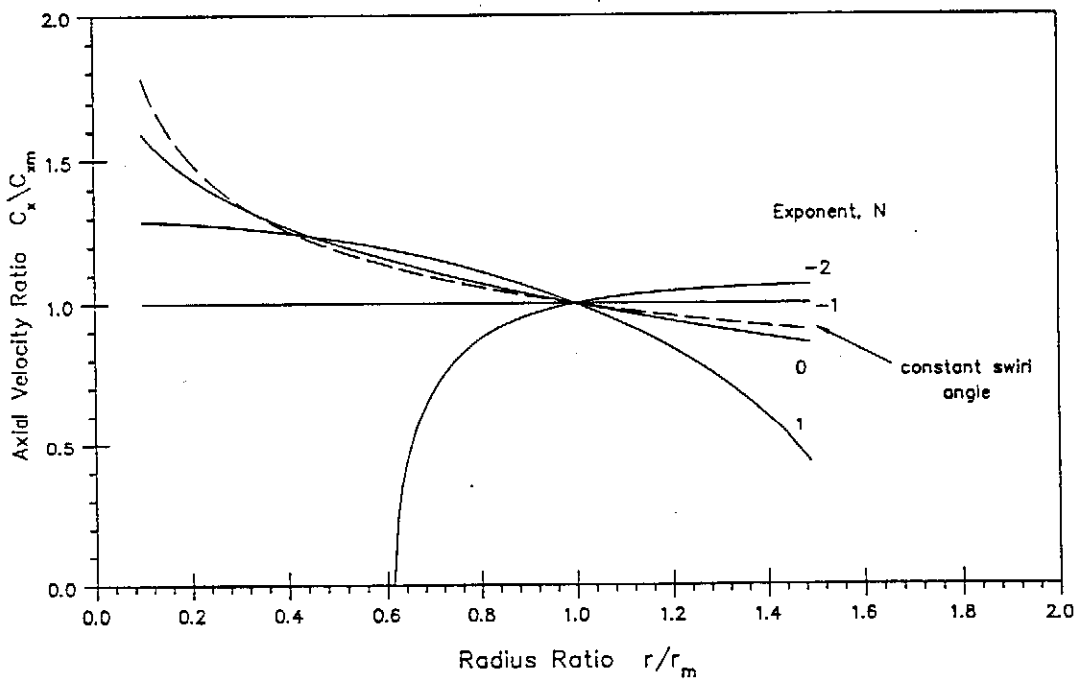Figure 3.3 Velocity triangle variation : Swirl velocity
vs Radius ratio

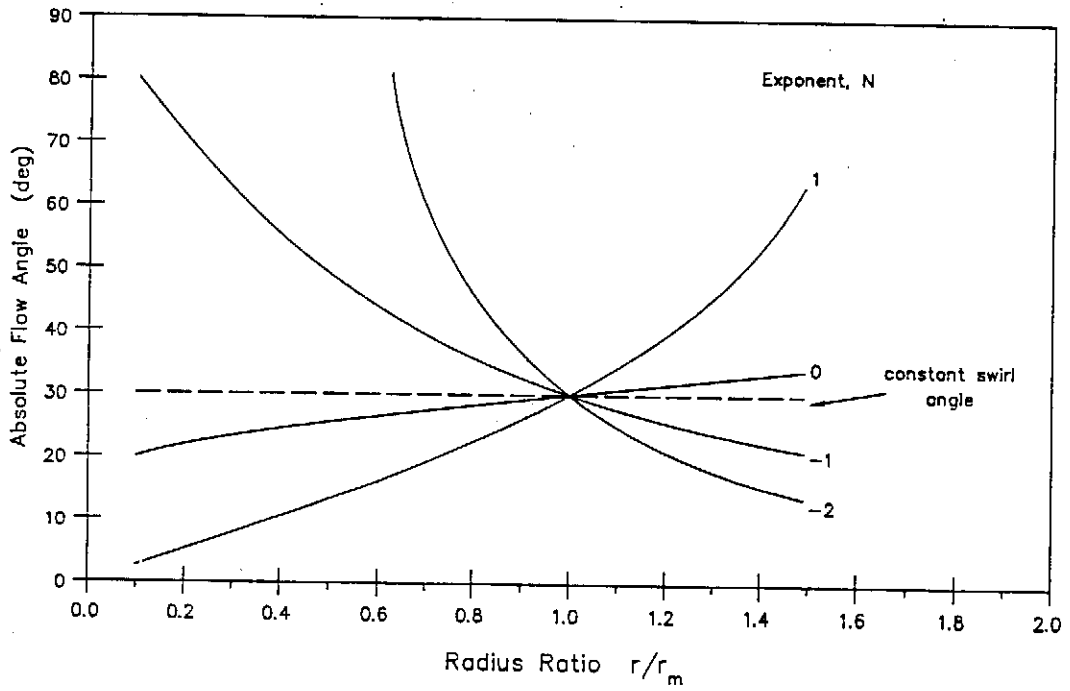Figure 3.4 Velocity triangle variation : Axial velocity
vs Radius ratio

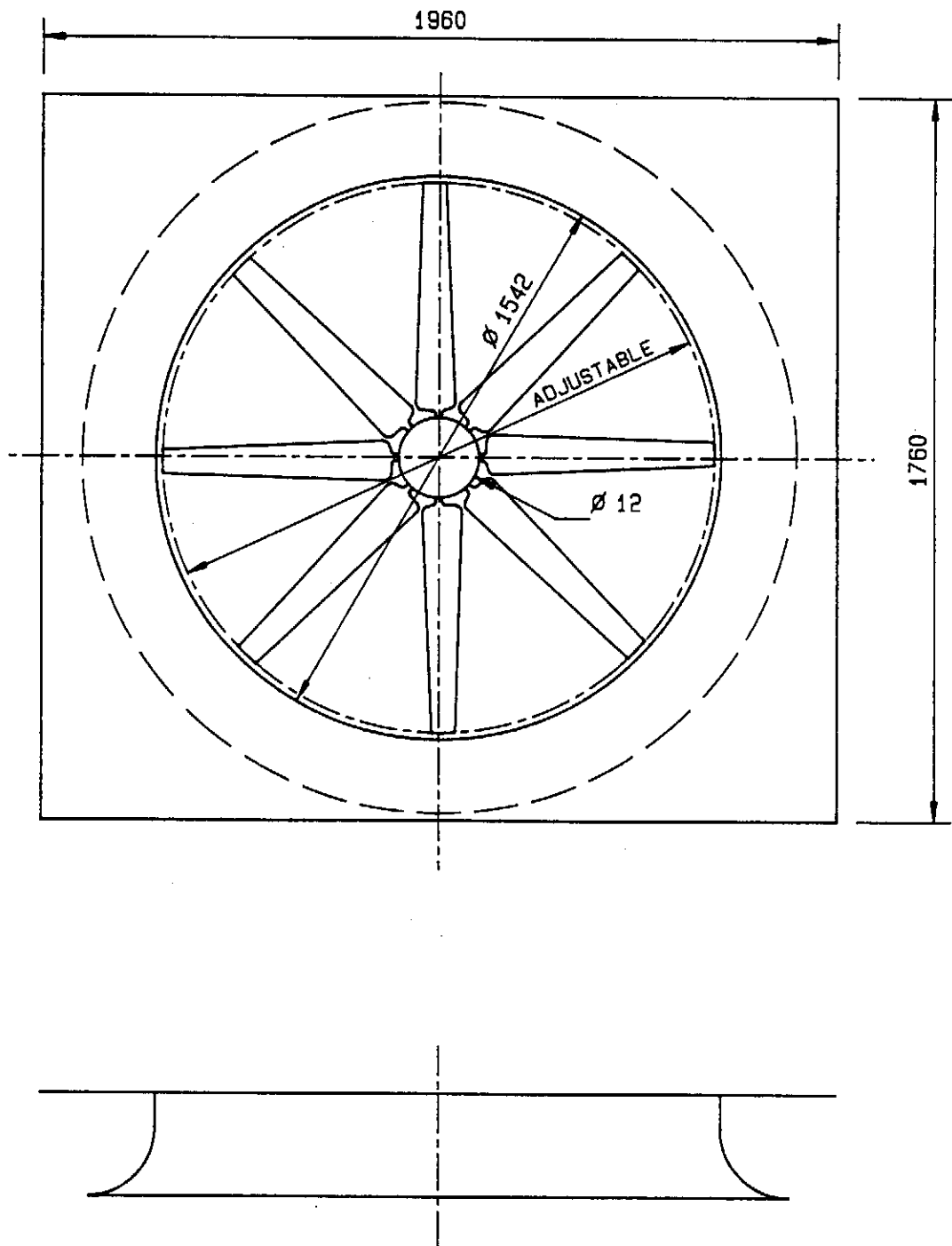Figure 3.5 Velocity triangle variation : Absolute flow angle vs Radius ratio

1960

1760

Ø 1542

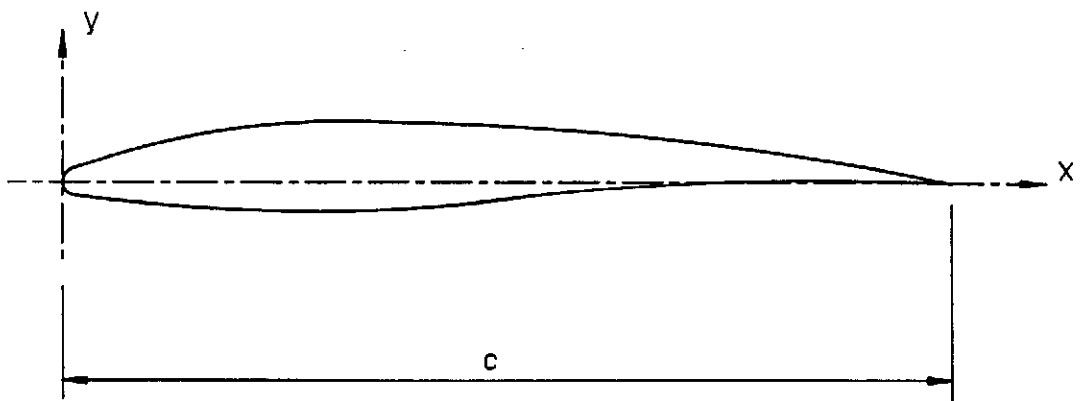ADJUSTABLE

Ø 12

Figure 4.1 V Fan rotor

571mm
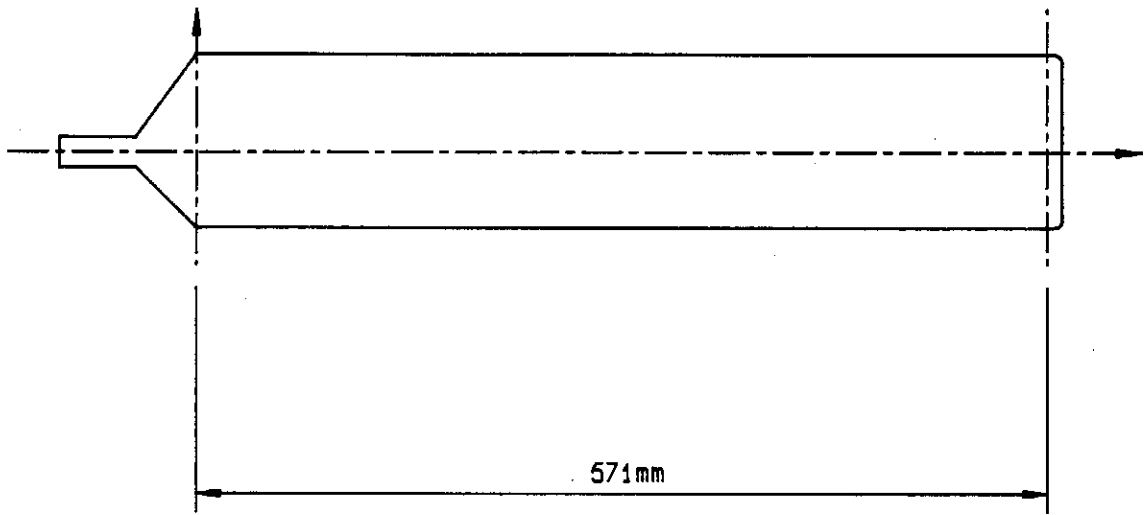
Figure 4.2 V Fan blading profile and planform

n_b	8
d	1.542 m
p_{FS}	210 Pa
$\dot{Q}$	16 m^2/s
P_{fan}	6000 W
N	750 rpm

Table 4.1 Design point specification

Blade speed	$U = \Omega r$
Relative inlet flow angle	$\tan \beta_1 = c_{x_1}/U$
Inlet absolute flow angle	$\alpha_1 = 0$
Inlet absolute velocity	$c_1 = c_{x_1}$
Inlet relative velocity	$w_1 = \sqrt{U^2 + c_{x_1}^2}$
Exit absolute flow angle	$\tan \alpha_2 = c_{\theta_2}/c_{x_2}$
Exit absolute velocity	$c_2 = \sqrt{c_{\theta_2}^2 + c_{x_2}^2}$
Exit relative velocity	$w_2 = c_{x_2}/\cos \beta_2$

Table 4.2   Velocity vector and angle relationships
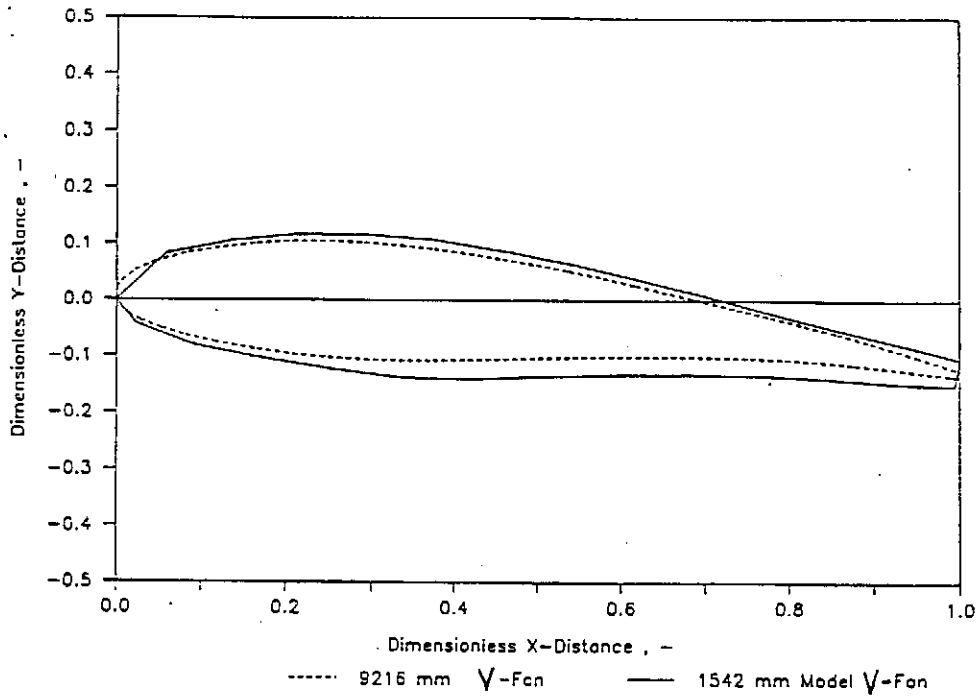
Figure 4.3 V Fan blading differences between model and
full scale - root section (from Venter
(1990))
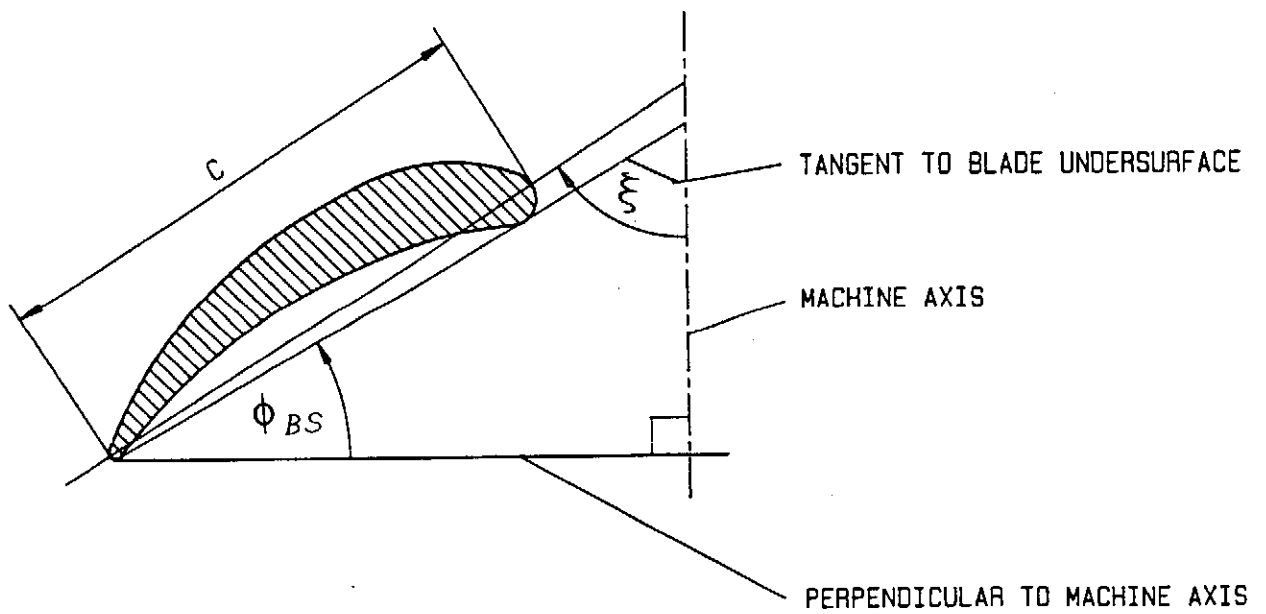
Figure 4.4 Blade setting angle and stagger angle
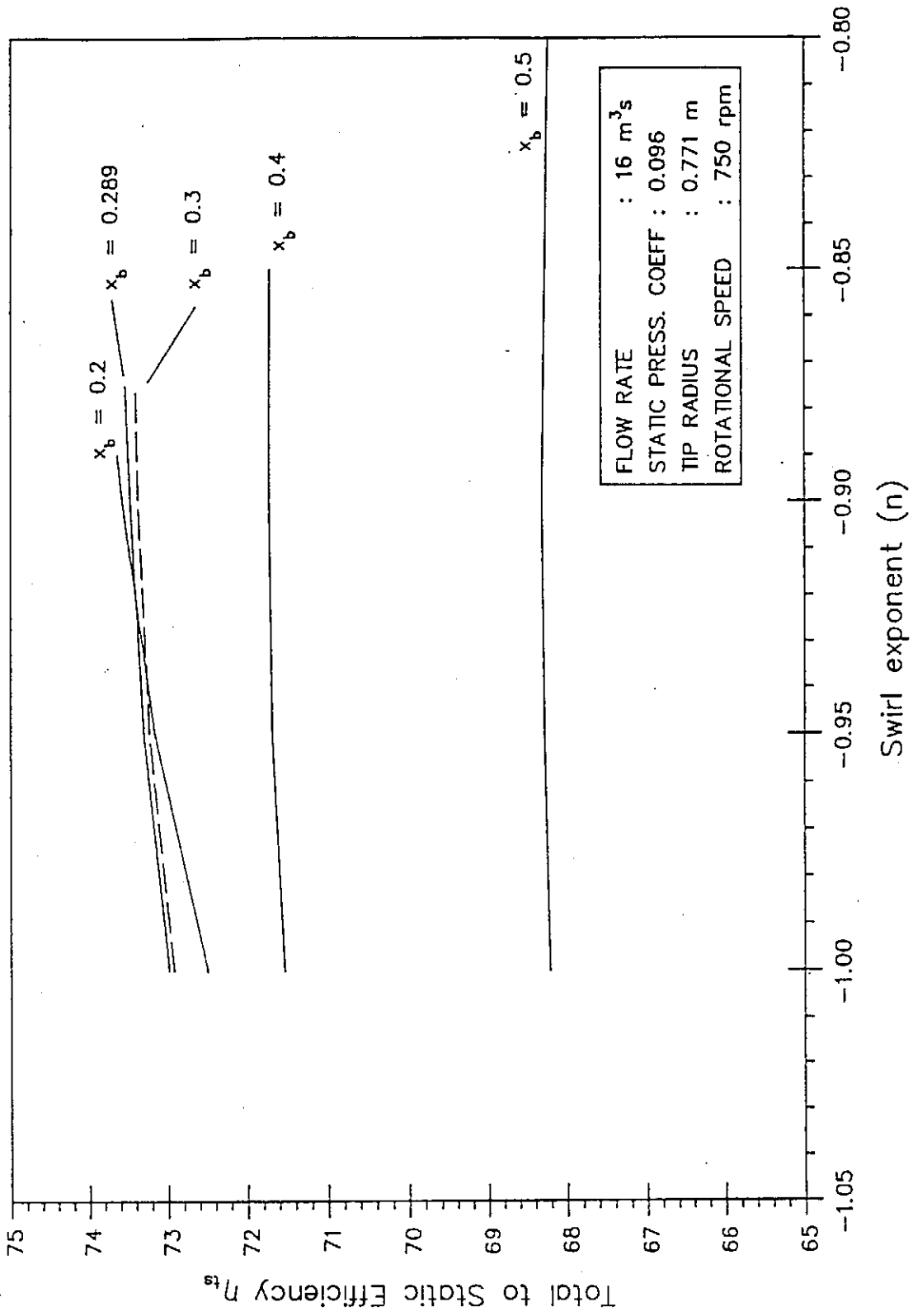
Figure 4.5 Fan total to static efficiency vs swirl exponent (FANVTX)

90
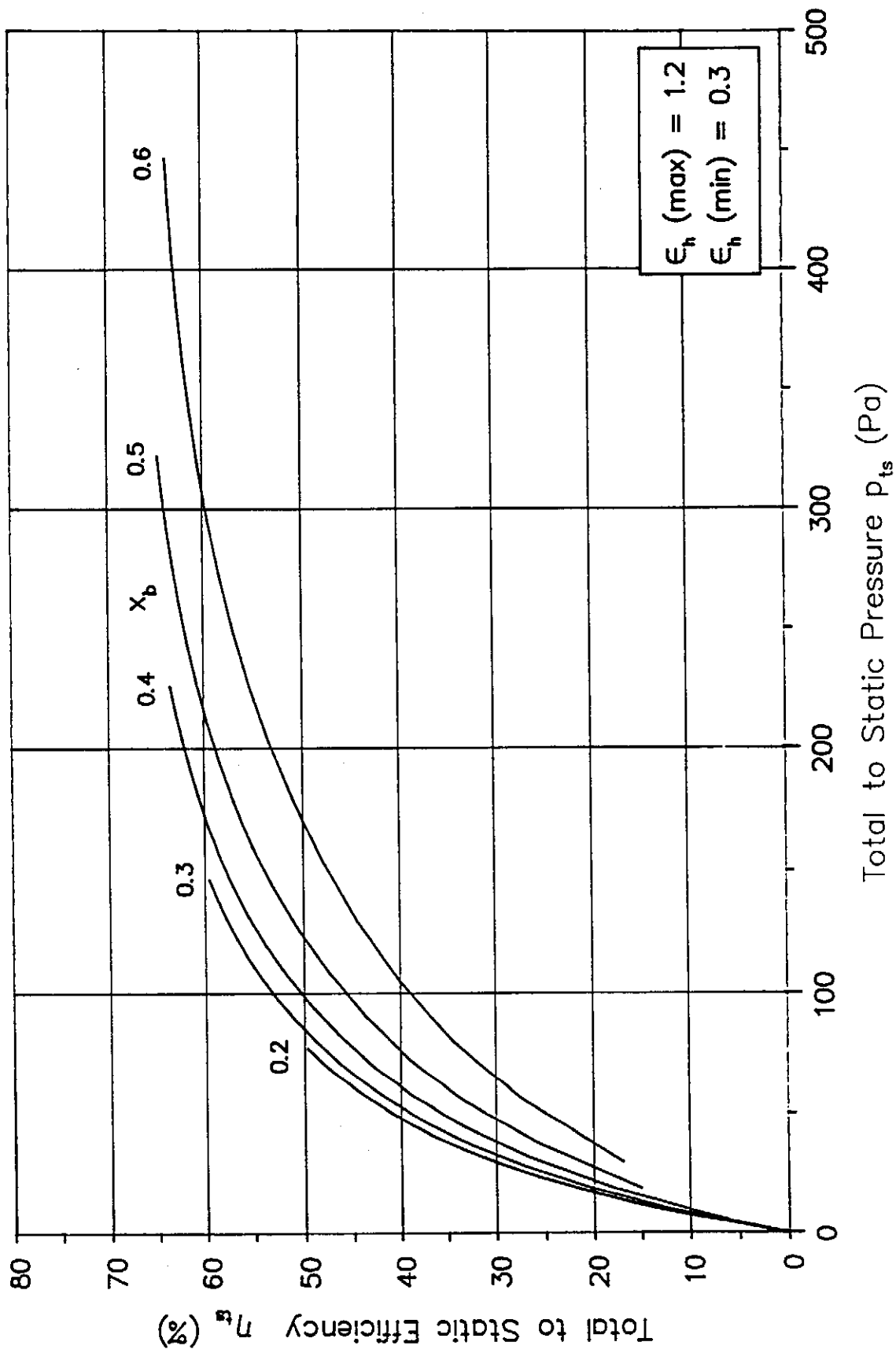
Figure 4.6. Total to static efficiency vs total to static pressure (FANOPT)
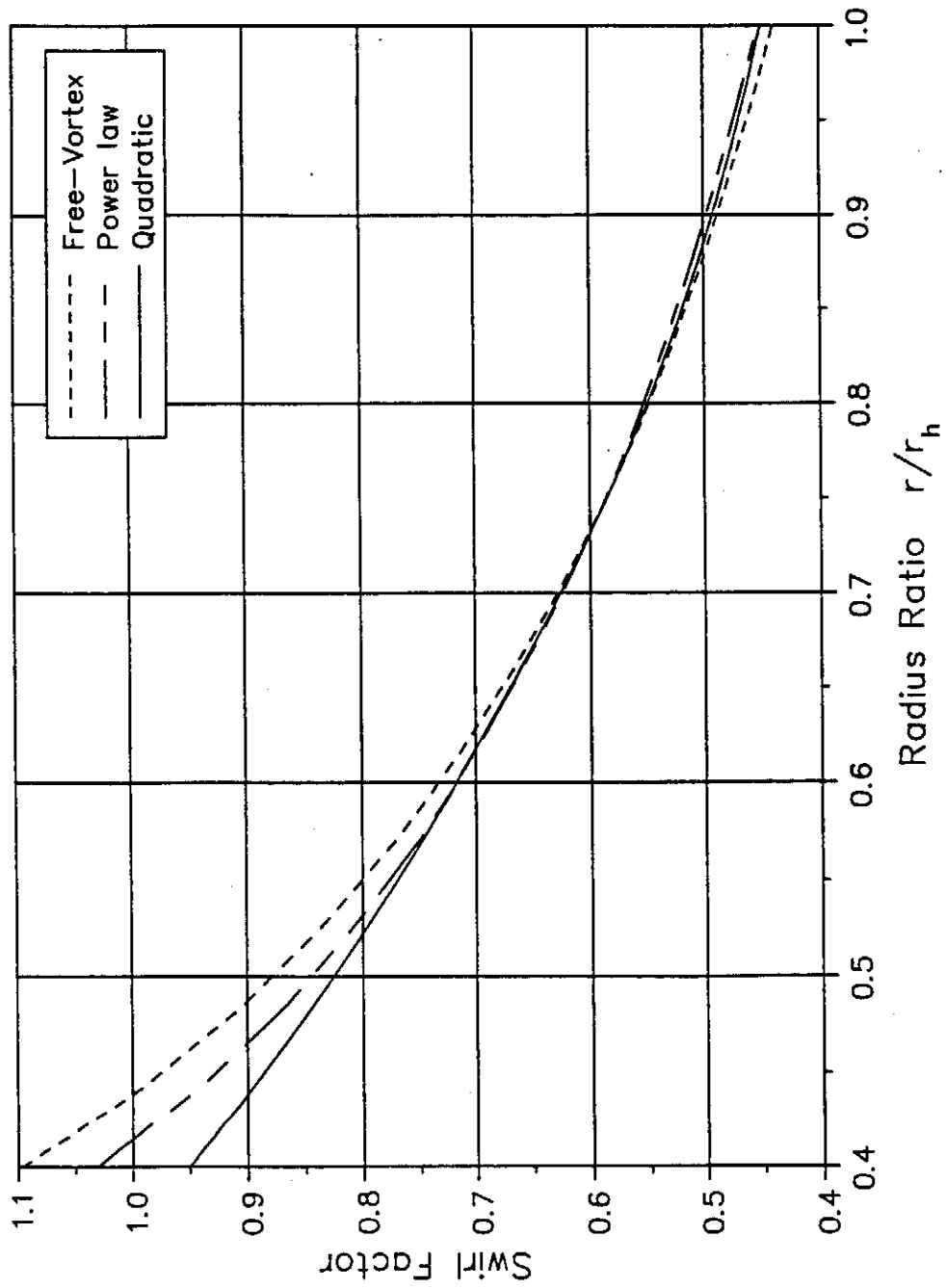
Figure 4.7 Swirl factor distribution
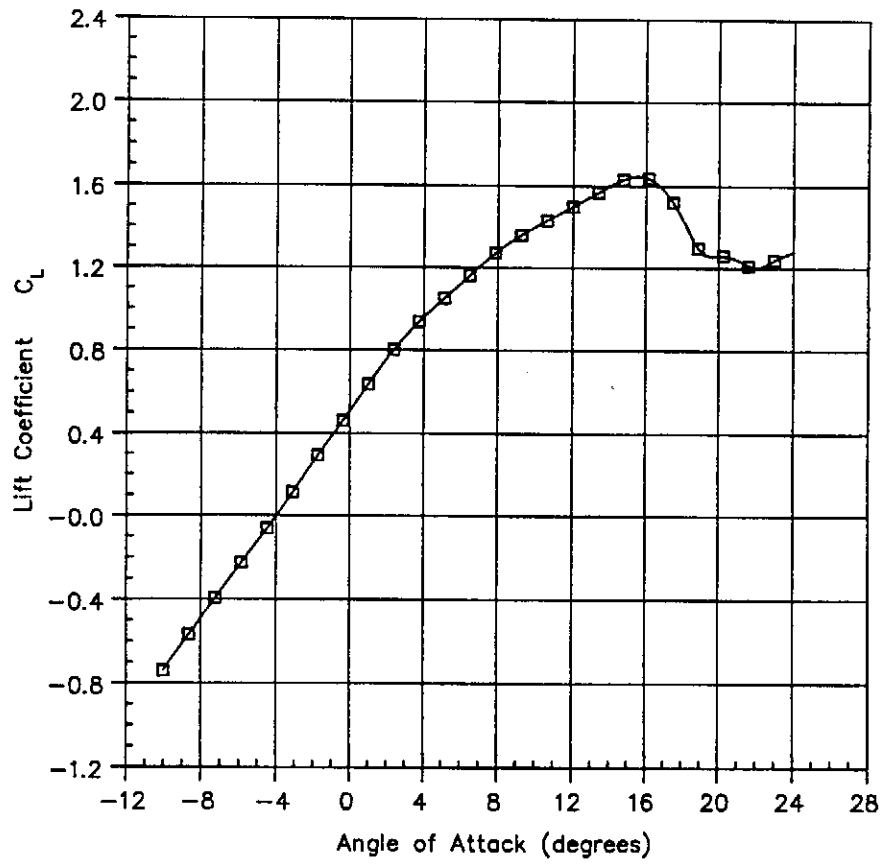
Figure 4.8 Lift coefficient vs angle of attack (NASA
LS profile)
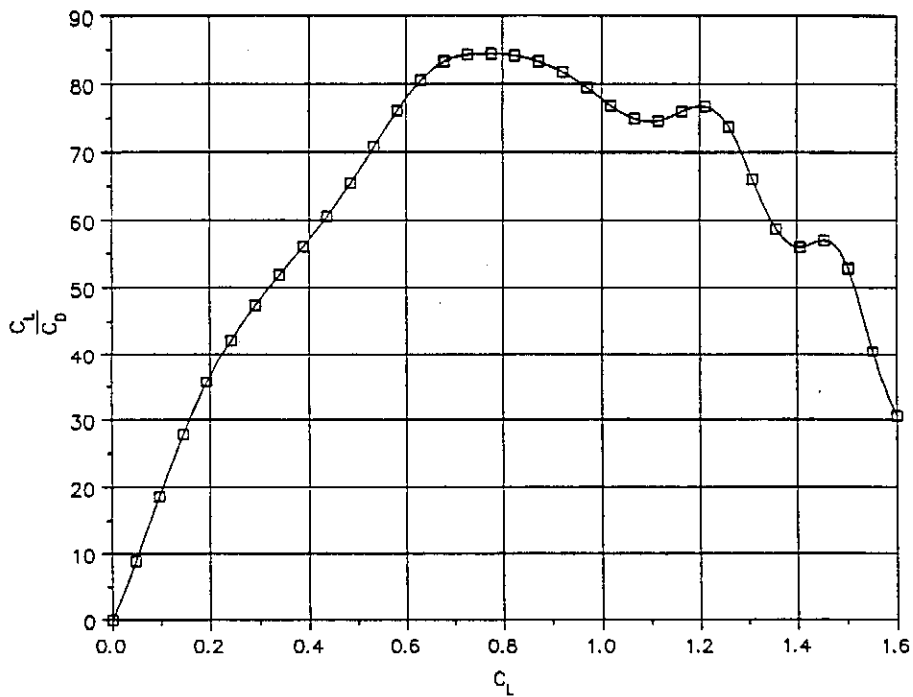
Figure 4.9 Lift/drag ratio (NASA LS profile)
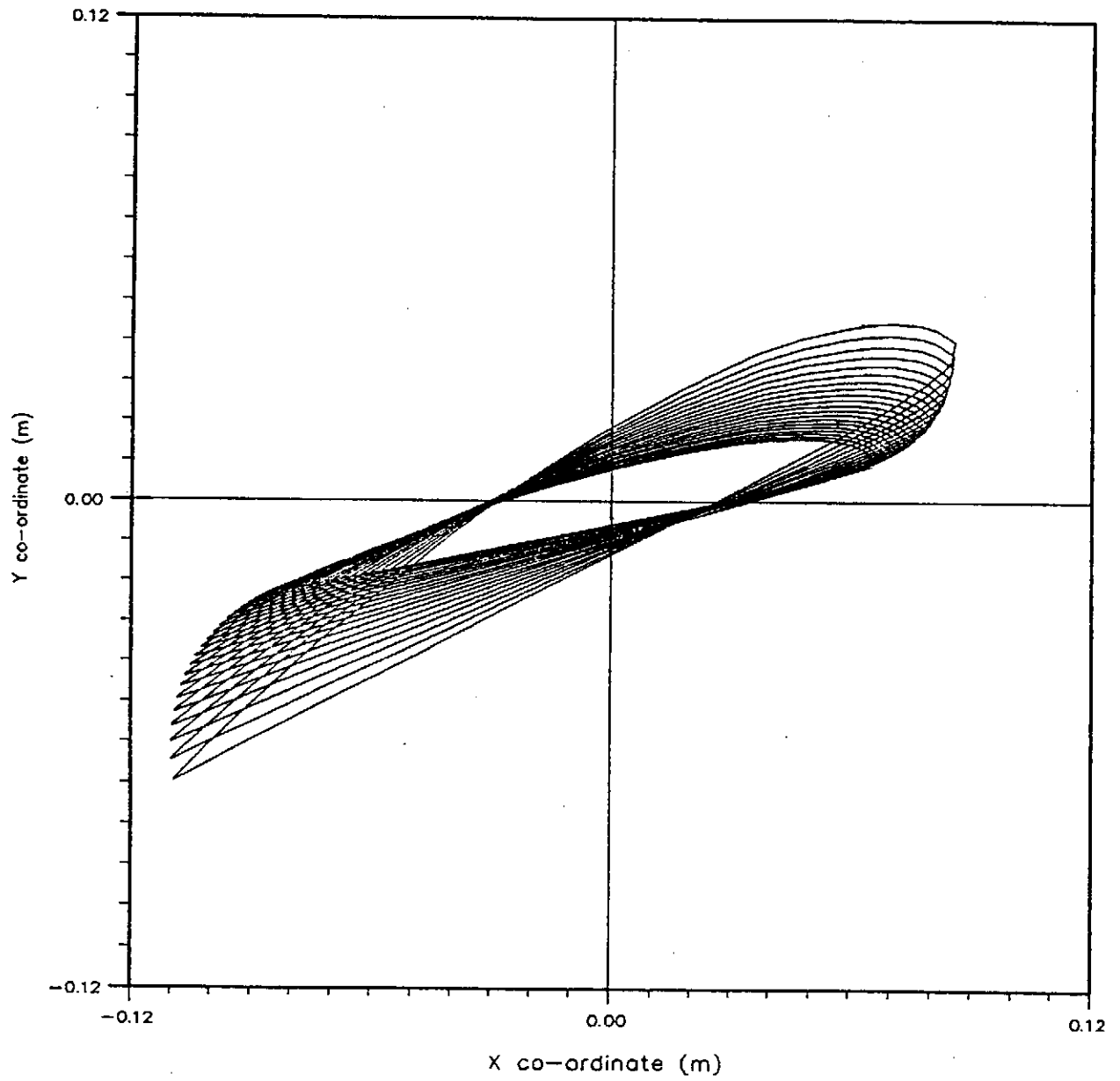
Figure 4.10 B1 fan stacked profile sections (Clark-Y profile)
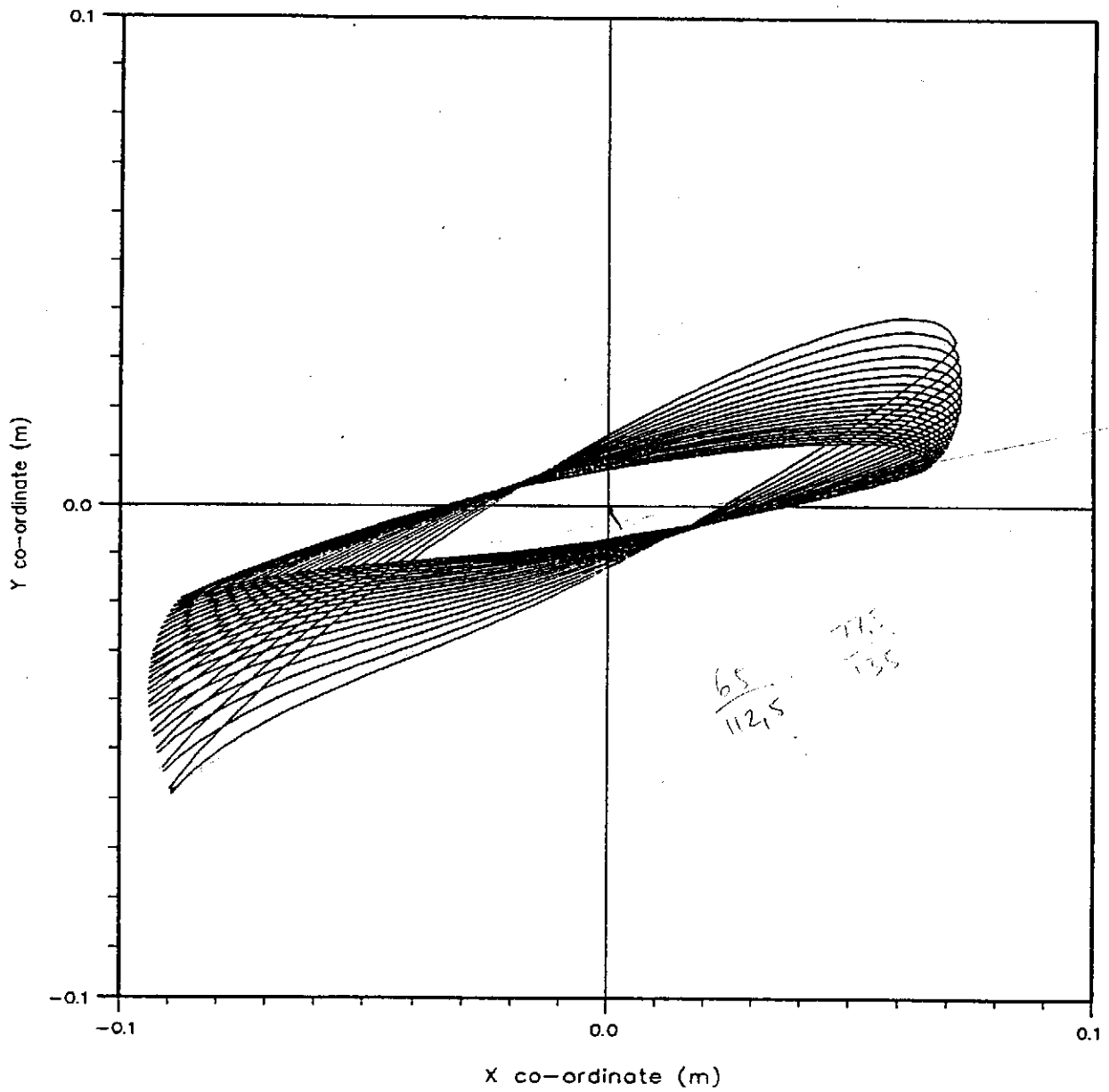
Figure 4.11 B2 fan stacked profile sections (NASA LS
        profile)
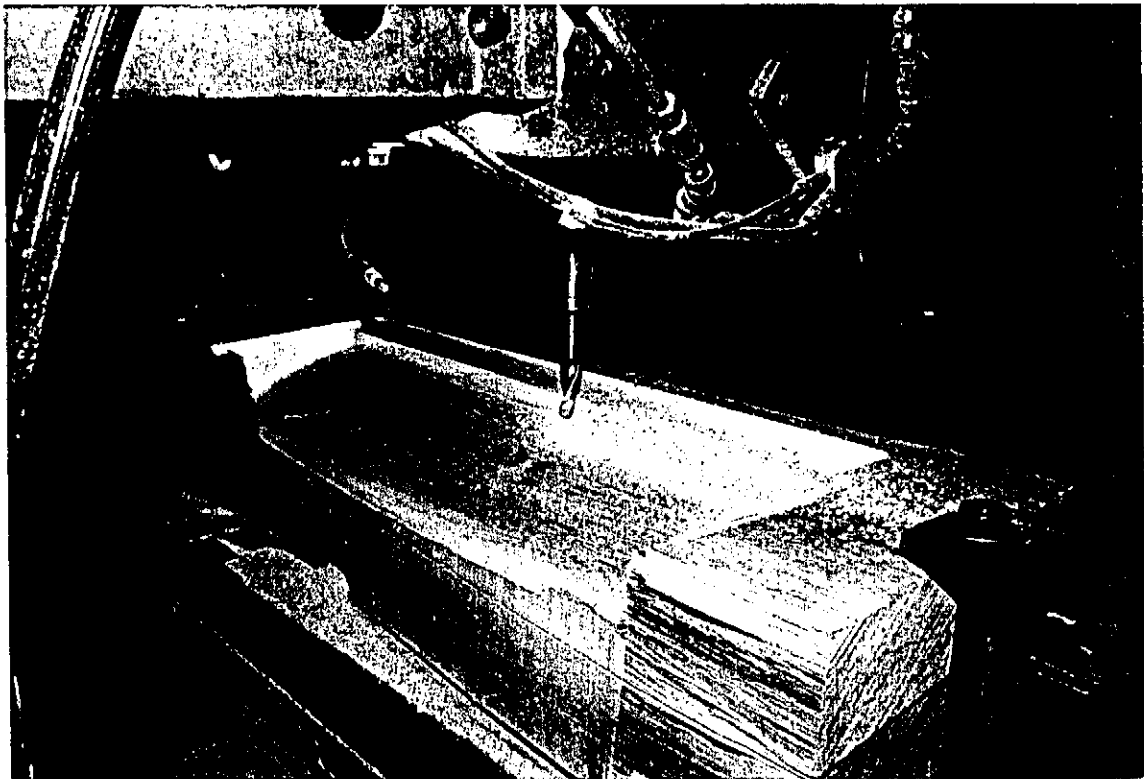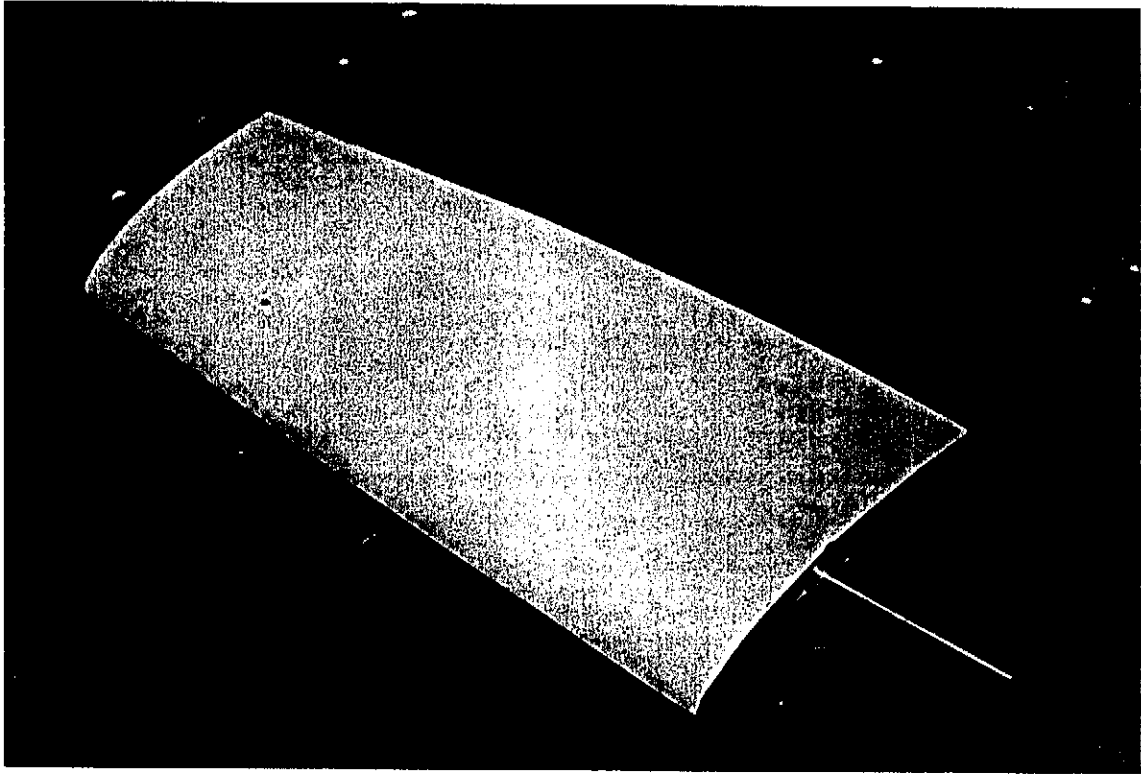
Figure 4.12 Wood master blades and moulds

ROOT SEAL

HUB SHROUD
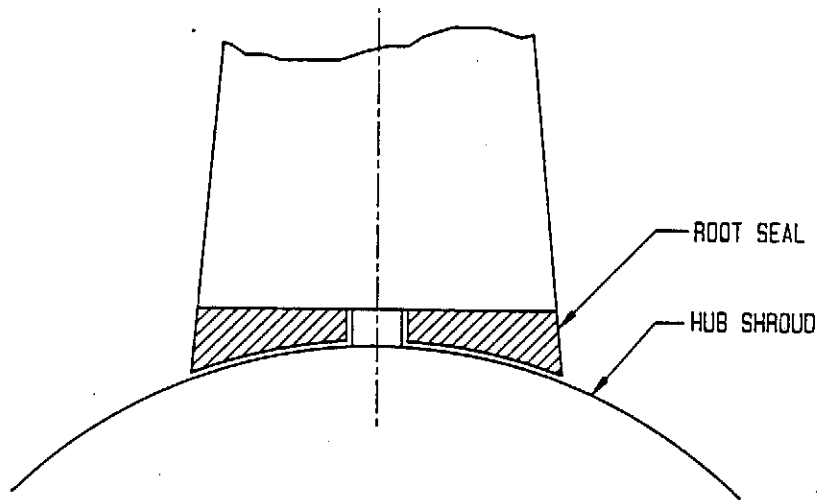
Figure 4.13 B fan root seals

CONTOURED PERSPEX BASE PLATE — CHORD LINE

BLADE ROOT SECTION

SHAFT LOCKING RING

PROTRACTOR

MACHINE AXIS
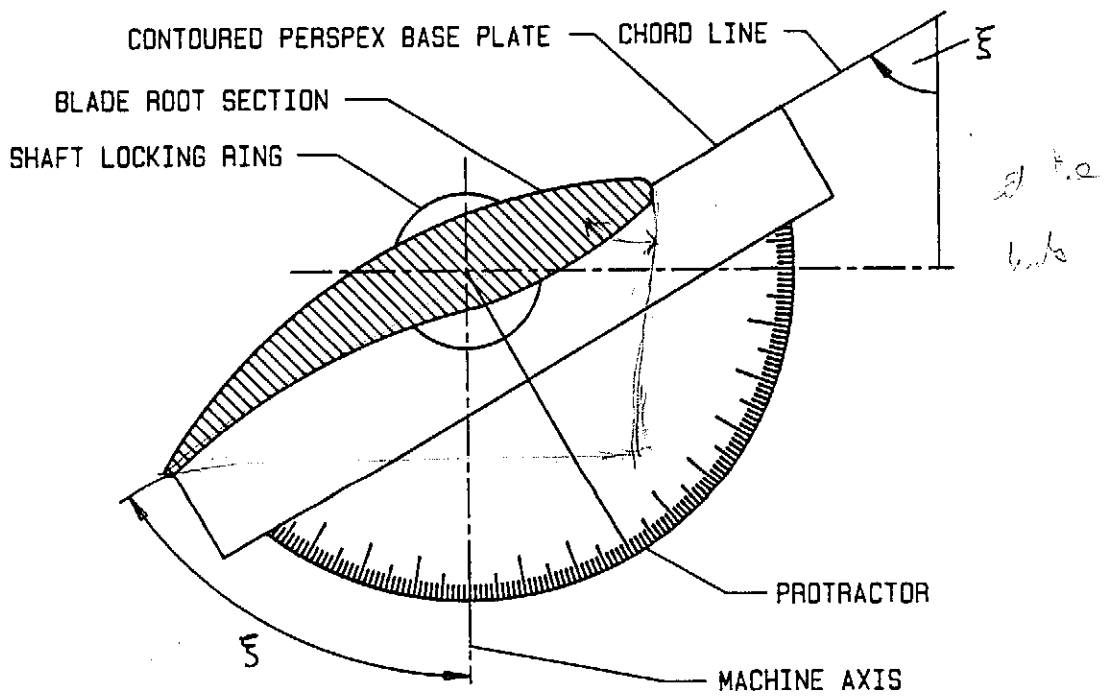
Figure 4.14 Protractors for setting B fan stagger angles

97
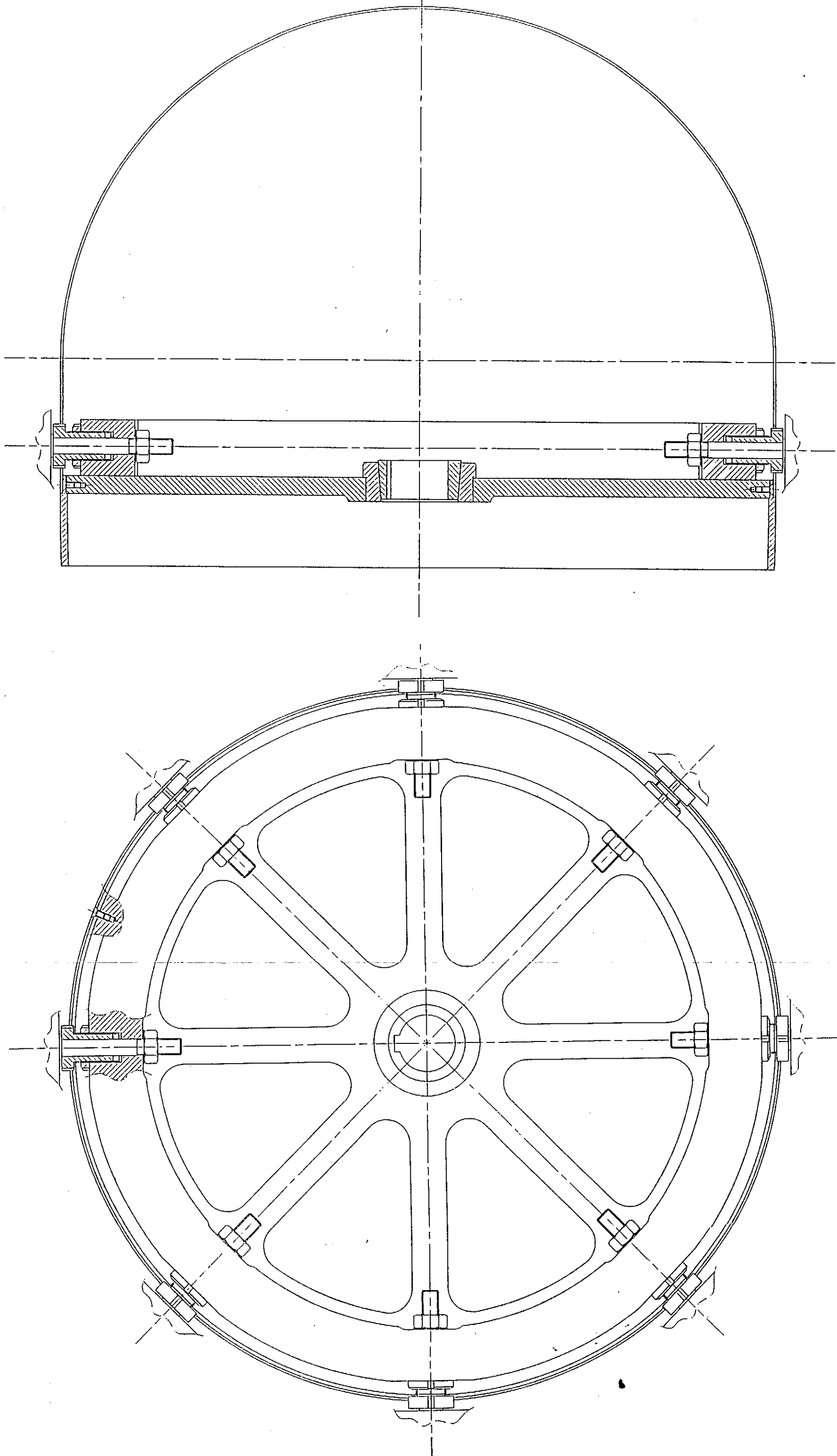
Figure 4.15 B fan hub and nose cone
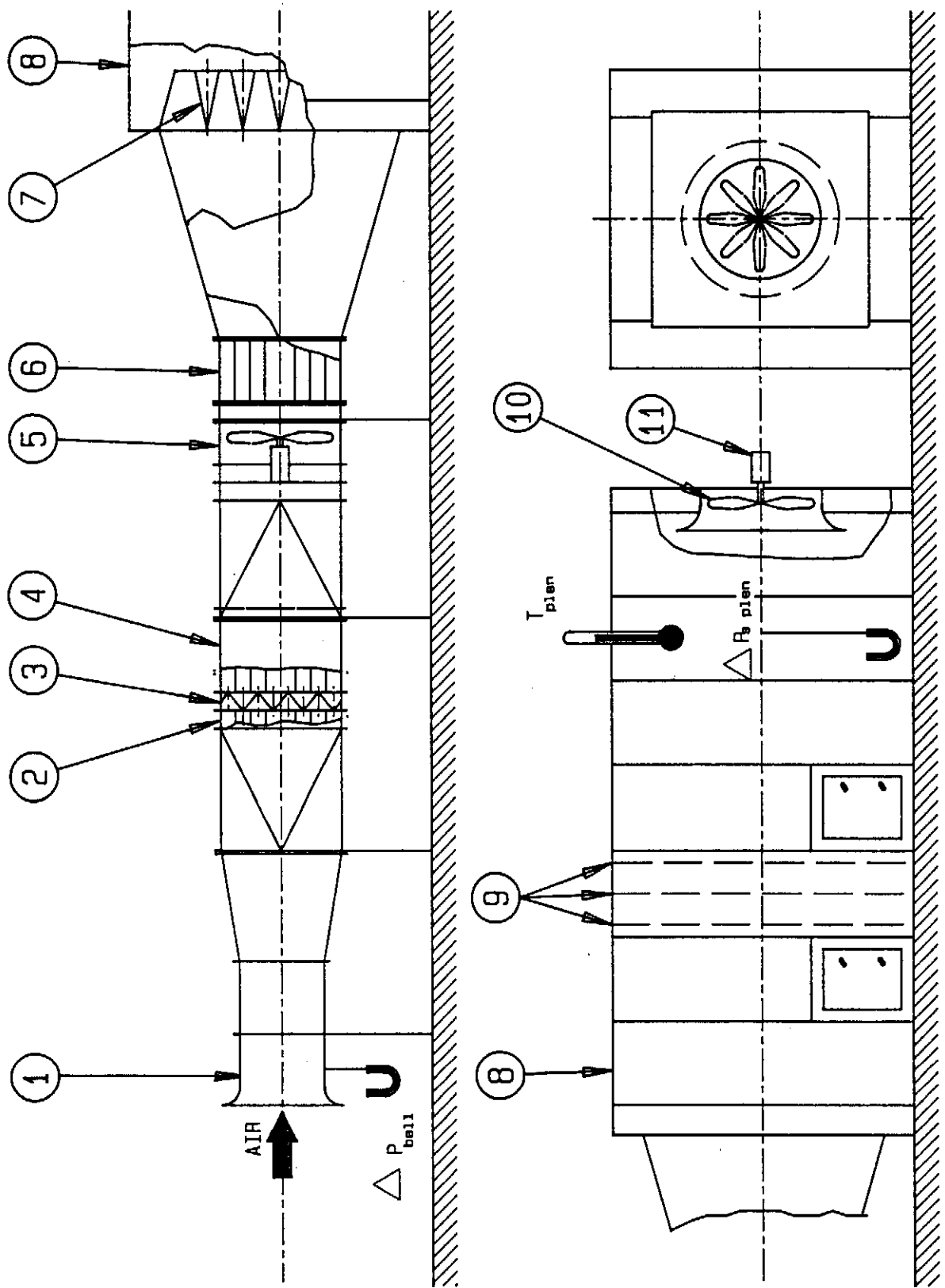
Figure 5.1 Test facility schematic (from Venter (1990))
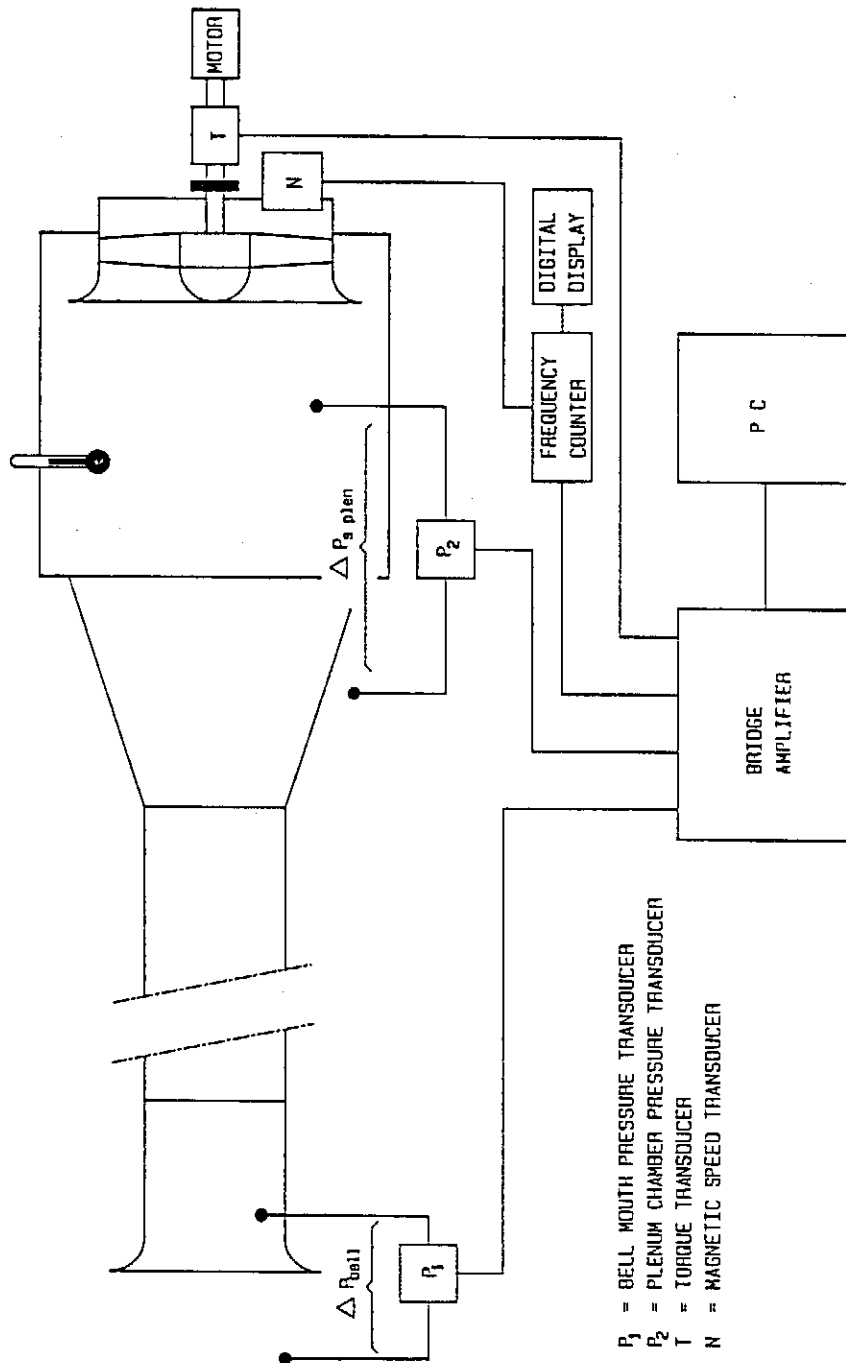
Figure 5.2 Test instrumentation schematic

P_1 = BELL MOUTH PRESSURE TRANSDUCER
P_2 = PLENUM CHAMBER PRESSURE TRANSDUCER
T = TORQUE TRANSDUCER
N = MAGNETIC SPEED TRANSDUCER

MOTOR

T

N

DIGITAL
DISPLAY

FREQUENCY
COUNTER

P C

BRIDGE
AMPLIFIER

$\triangle P_{s\,plen}$

P_2

$\triangle P_{bell}$

P_1

Ø = BLADE SETTING ANGLE

V-FAN HUB

FAN BLADE

VISE

VISE

SETTING PLATE

MEASURING TABLE
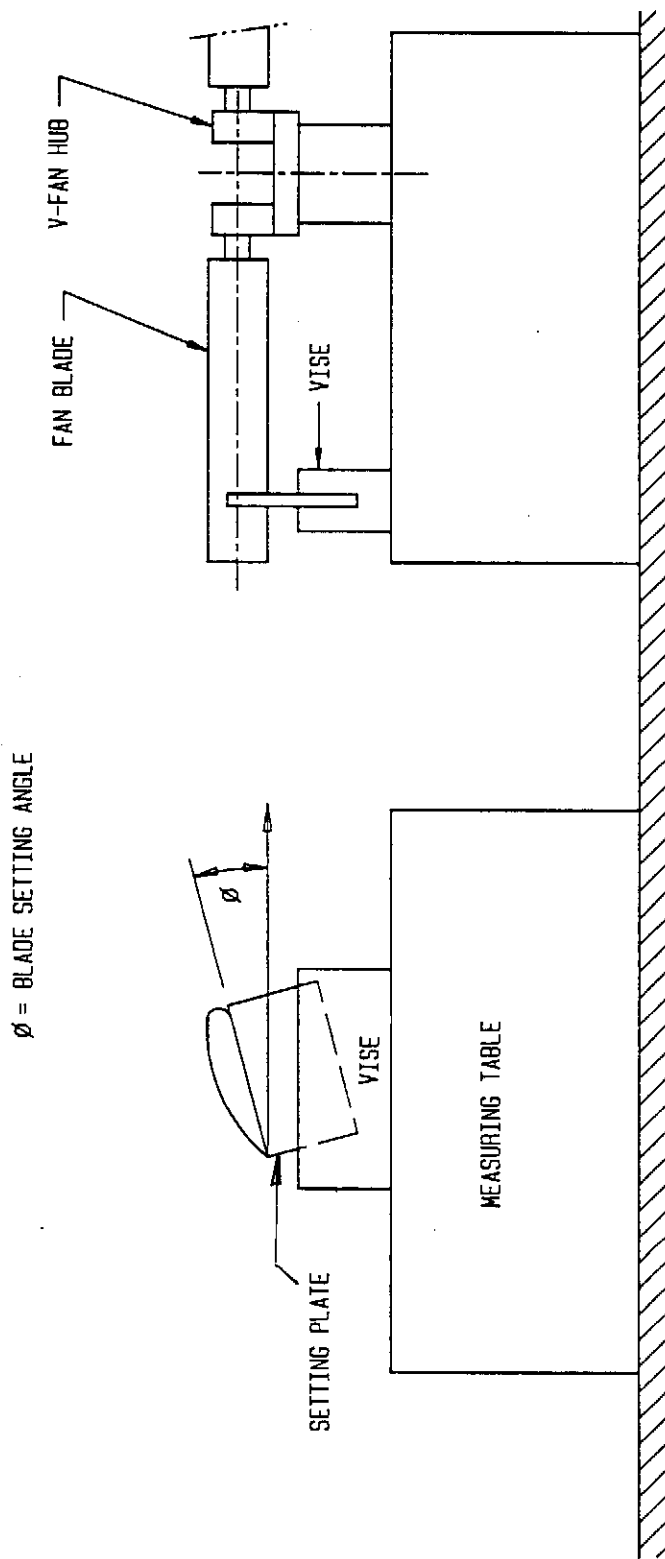
Figure 5.3 V fan blade angle setting

101
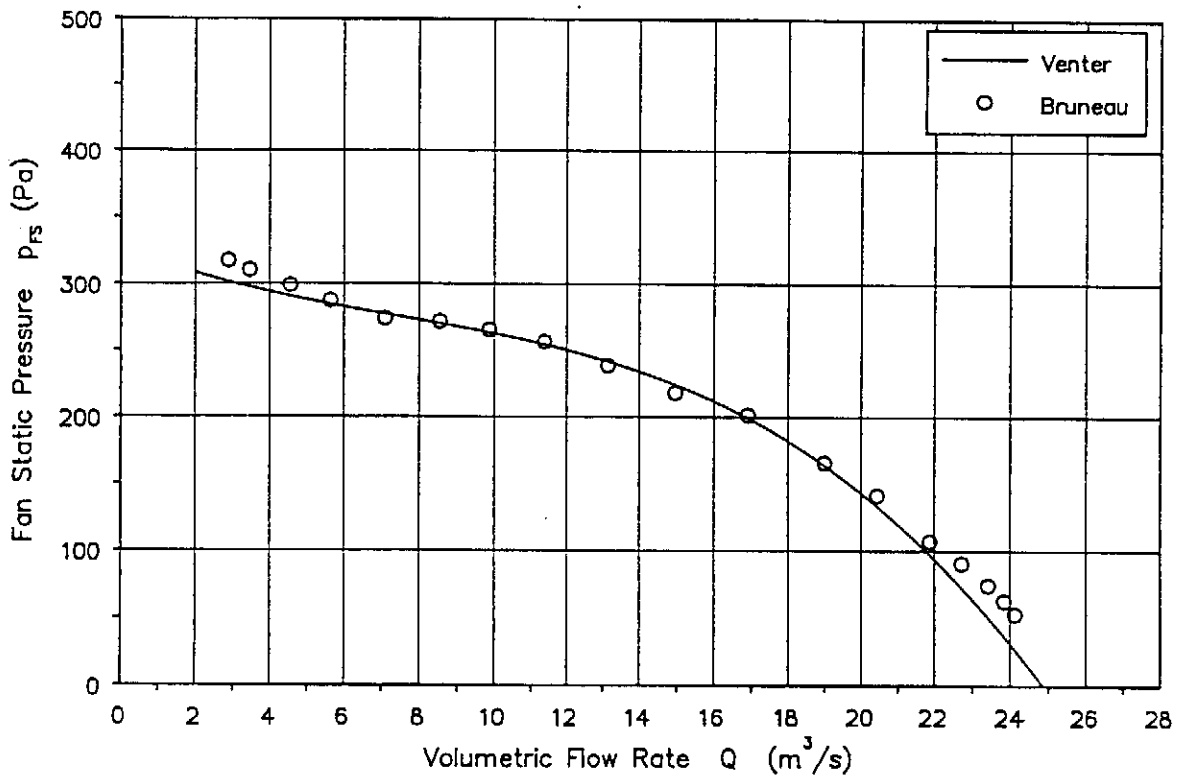
Figure 5.4 V fan pressure characteristic (no hub plate)
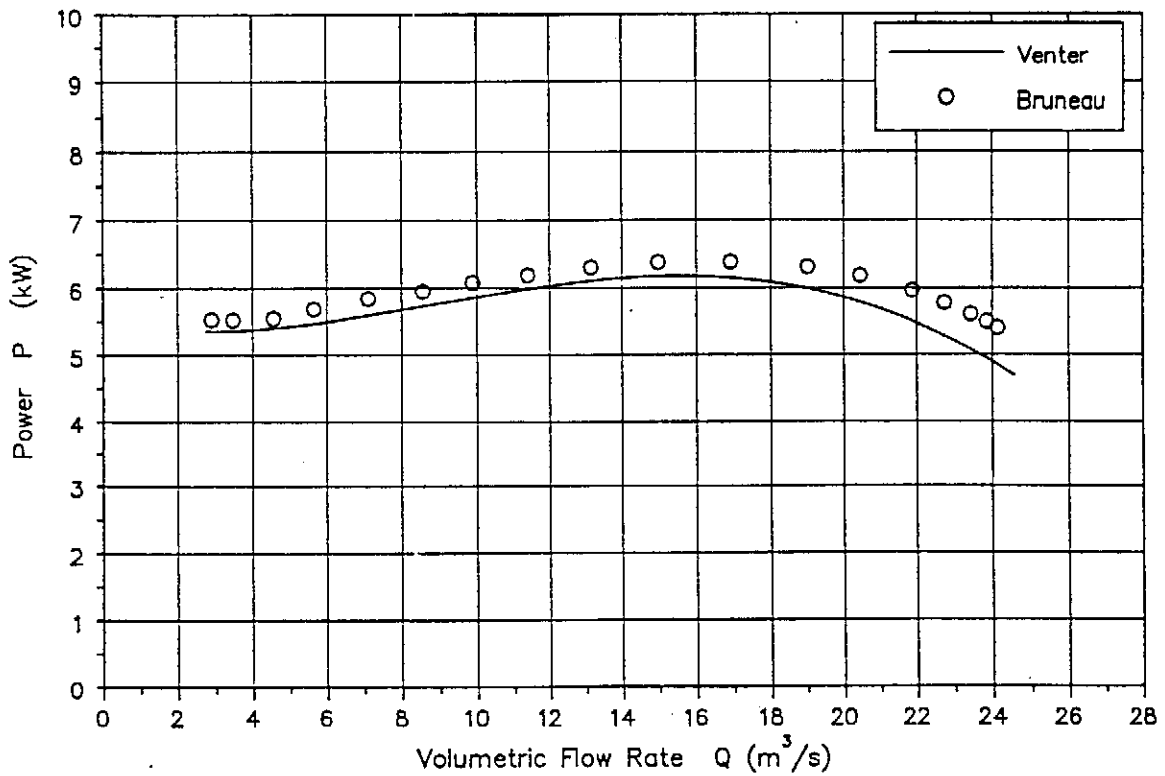
Figure 5.5 V fan power characteristic (no hub plate)
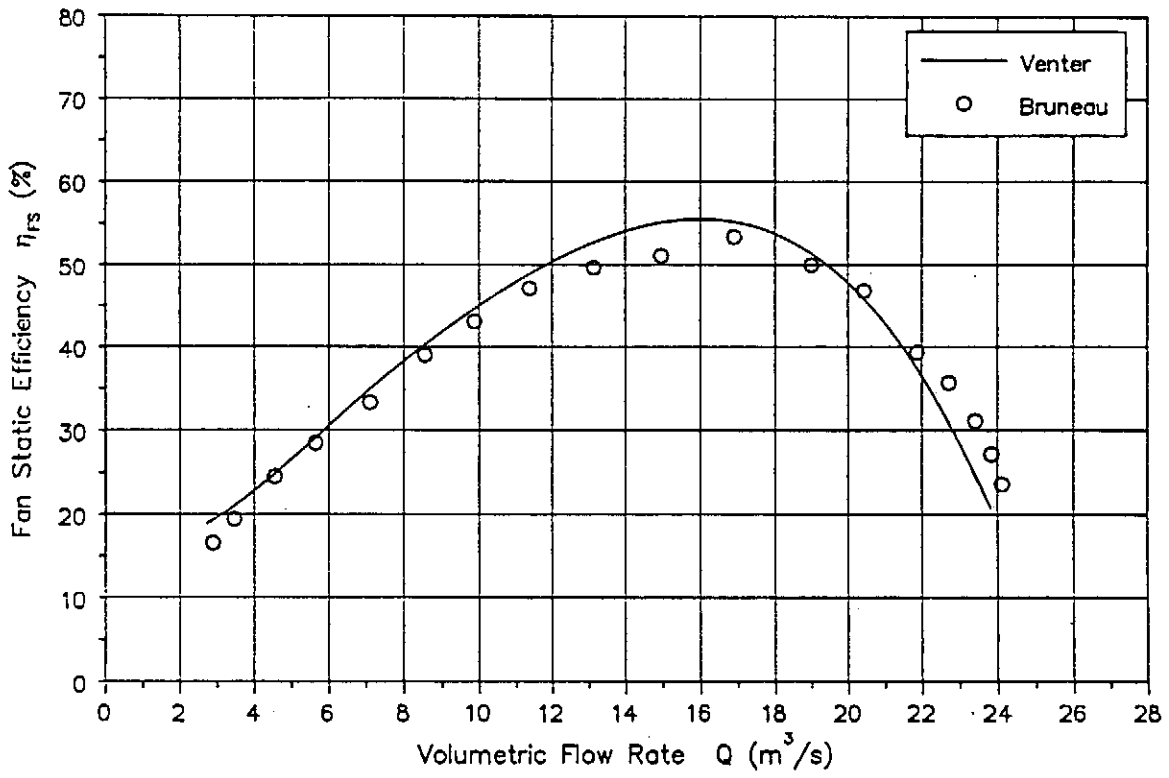
Figure 5.6 V fan efficiency characteristic (no hub plate)
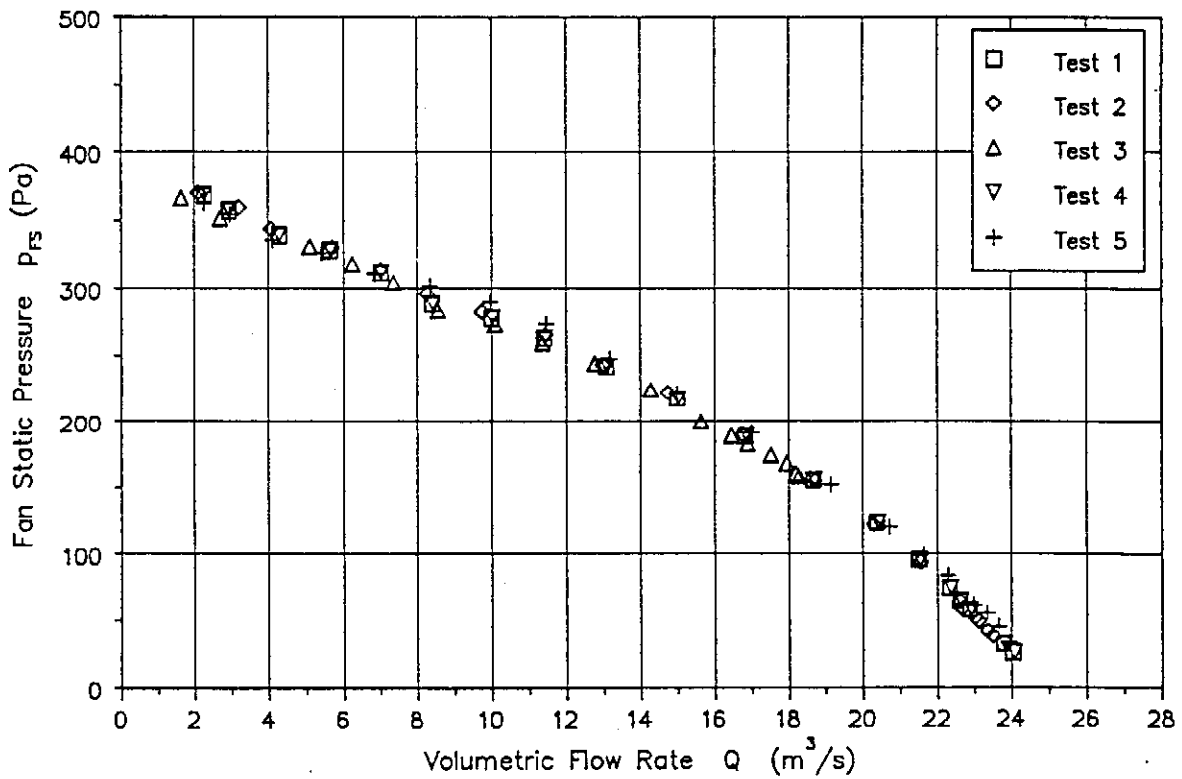
Figure 5.7 V fan pressure characteristic (hub plate)

103
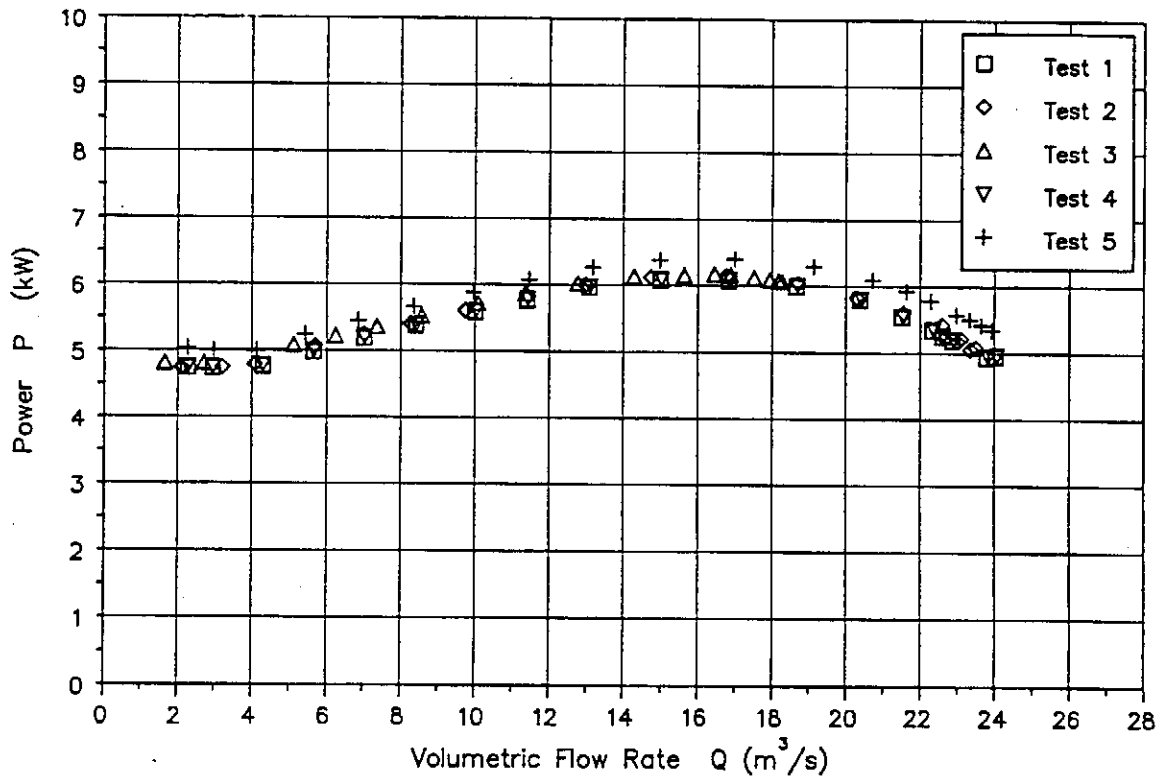
Figure 5.8 V fan power characteristic (hub plate)
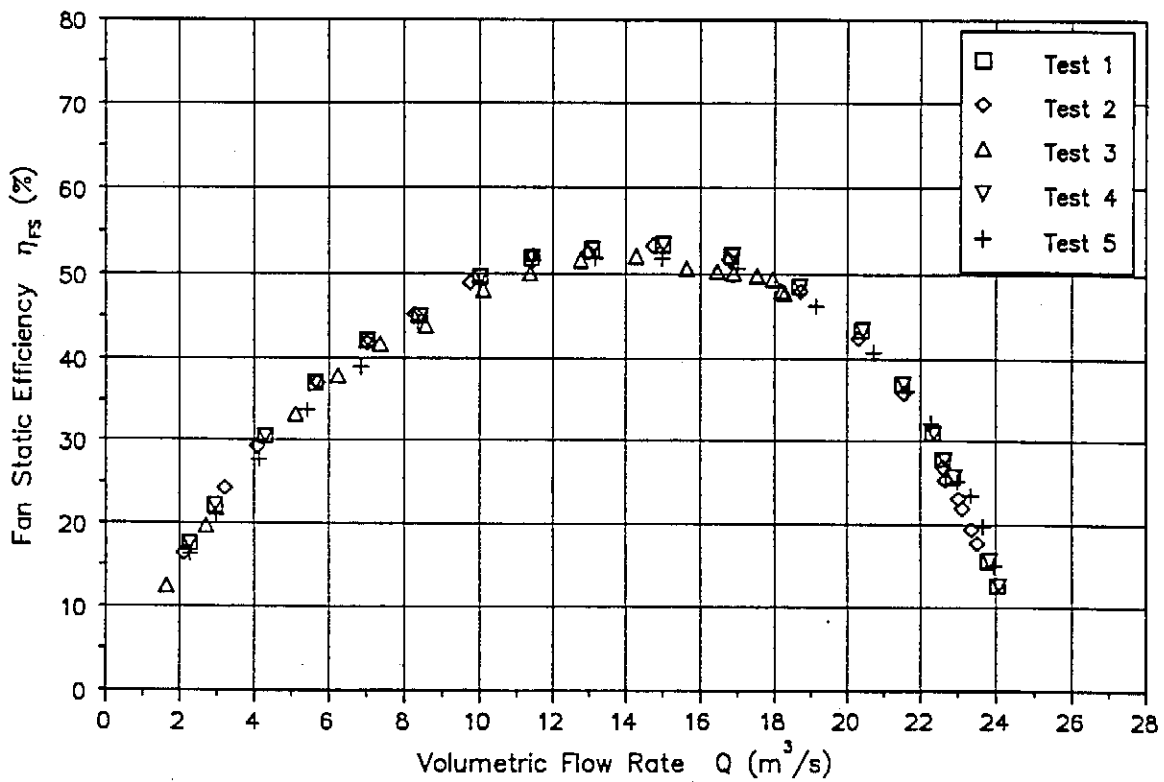
Figure 5.9 V fan efficiency characteristic (hub plate)
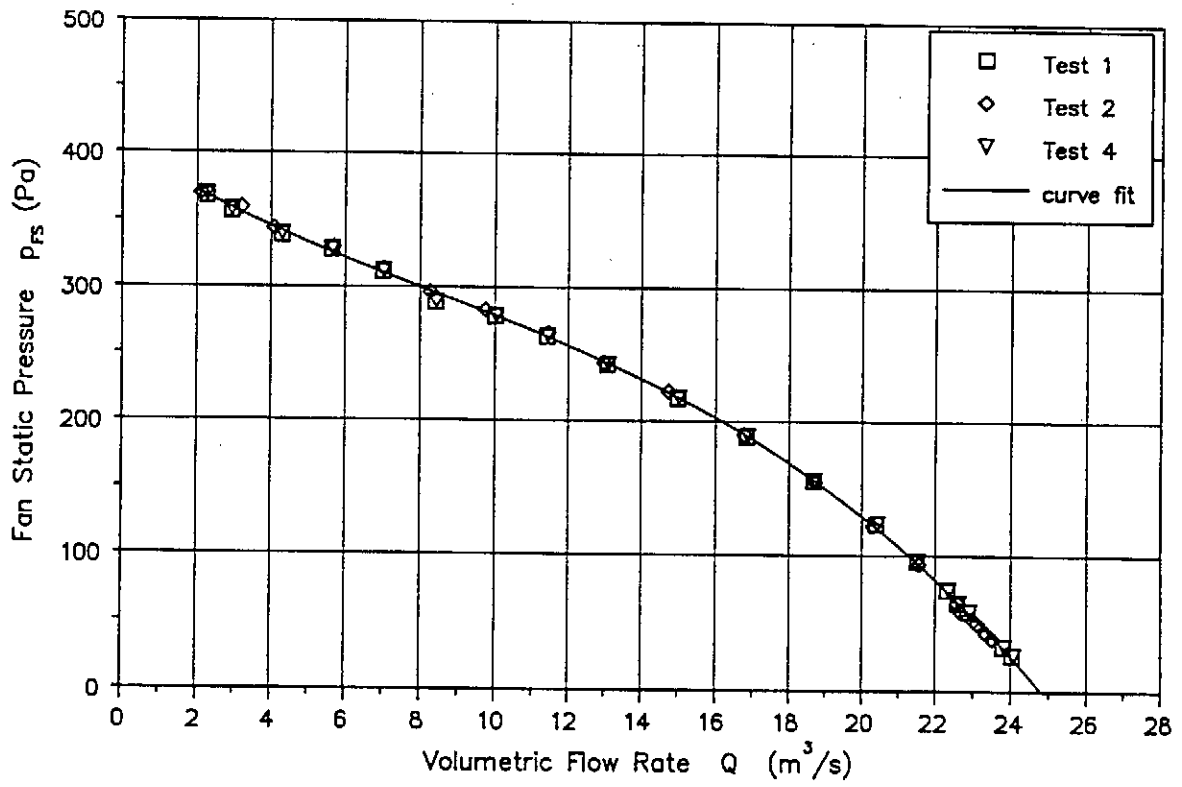
Figure 5.10 V fan pressure characteristic (datum)
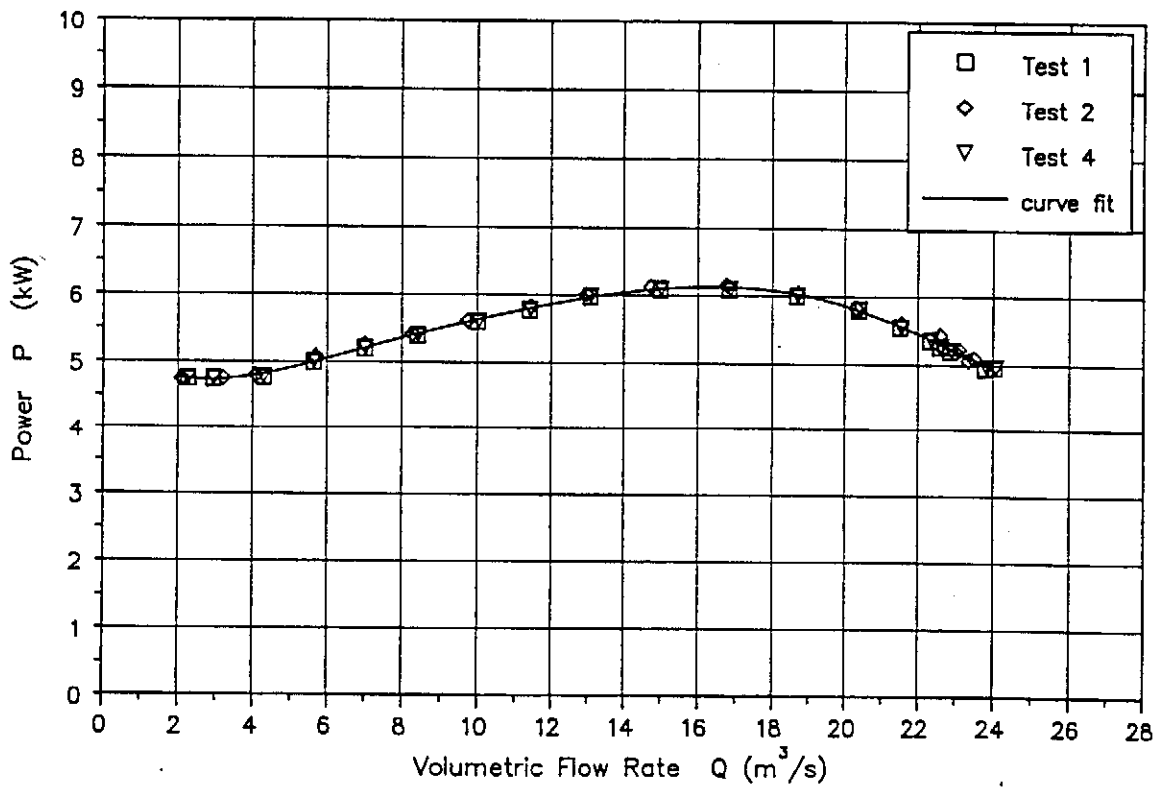
Figure 5.11 V fan power characteristic (datum)
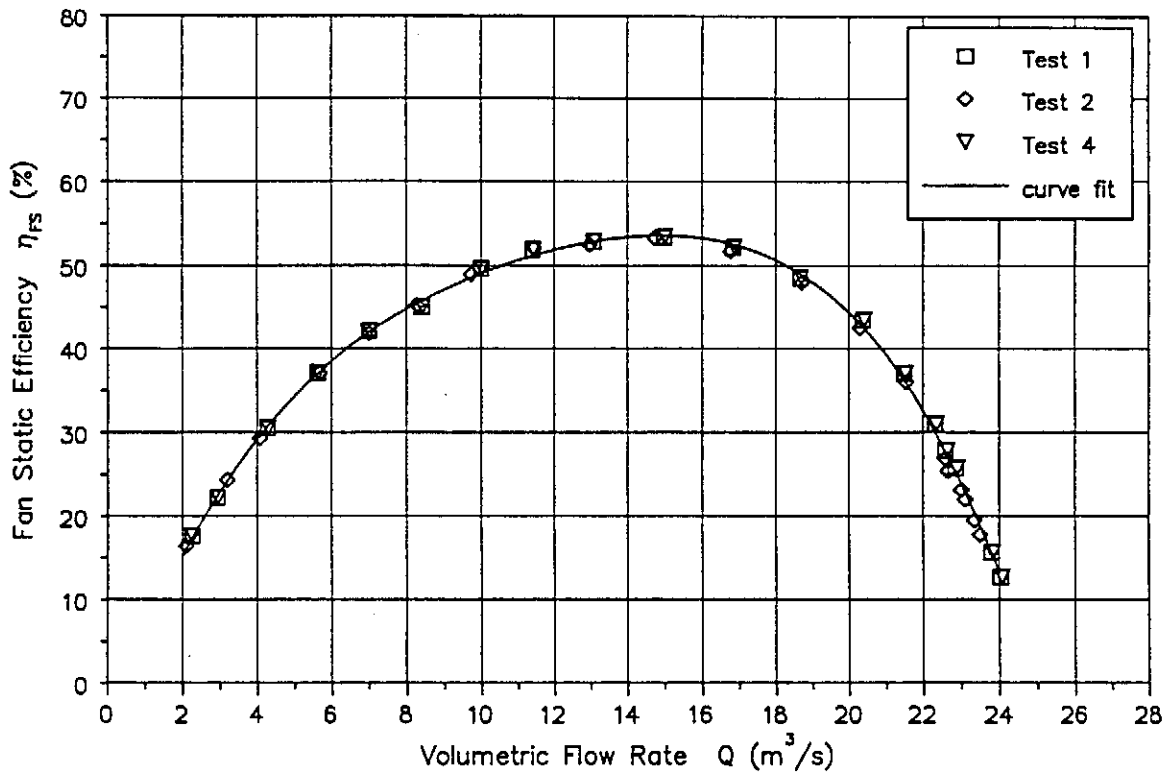
Figure 5.12 V fan efficiency characteristic (datum)
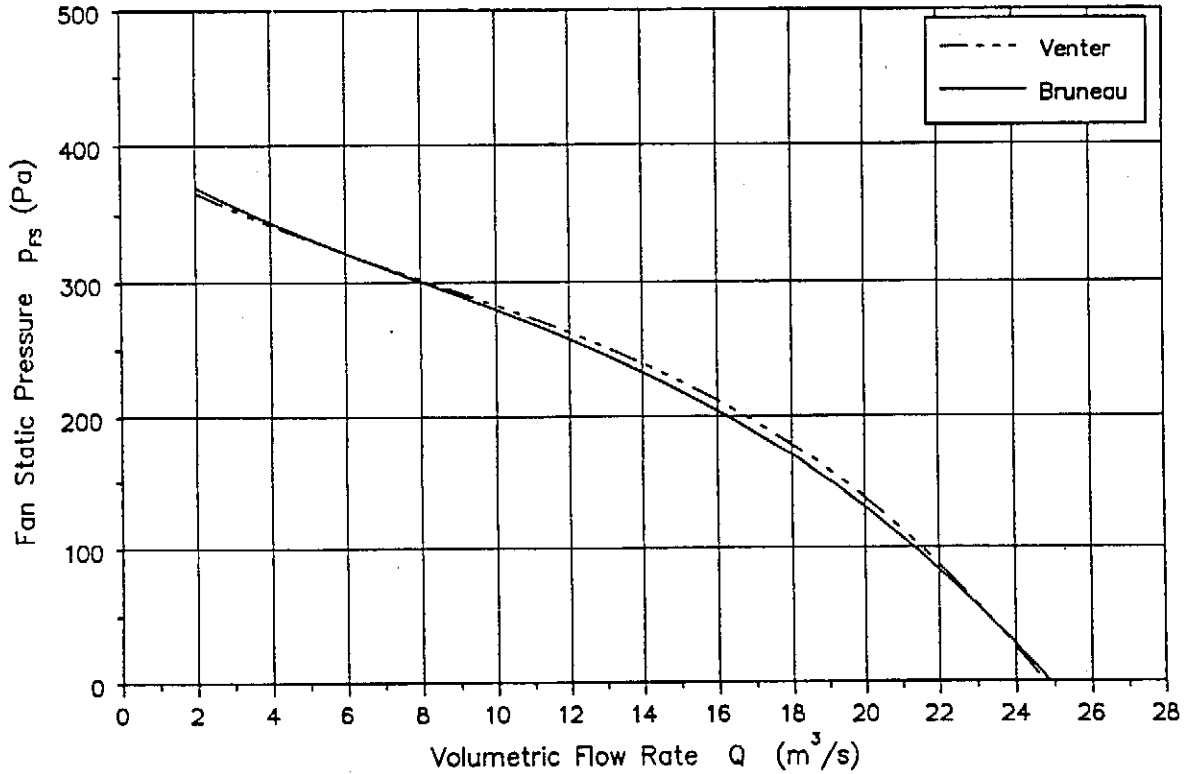
Figure 5.13 V fan pressure characteristic comparison
(Venter, Bruneau)
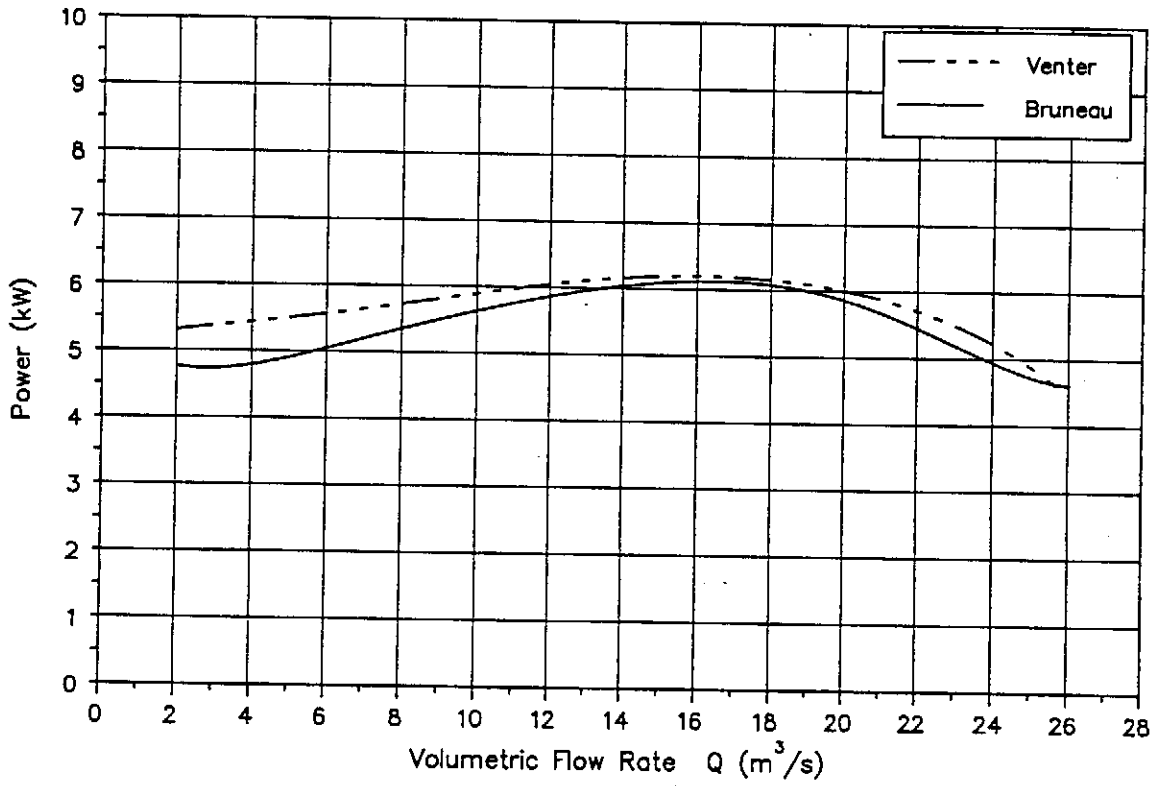
Figure 5.14 V fan power characteristic comparison
(Venter, Bruneau)
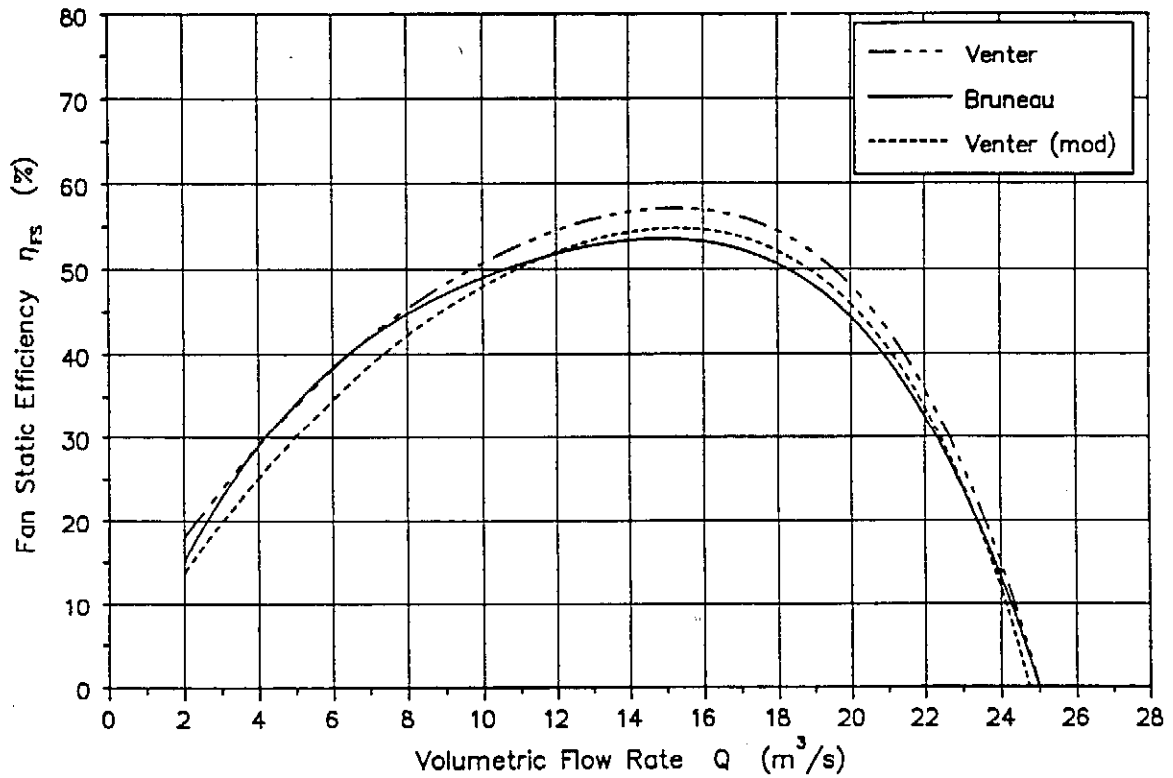
Figure 5.15 V fan efficiency characteristic comparison
(Venter, Bruneau)
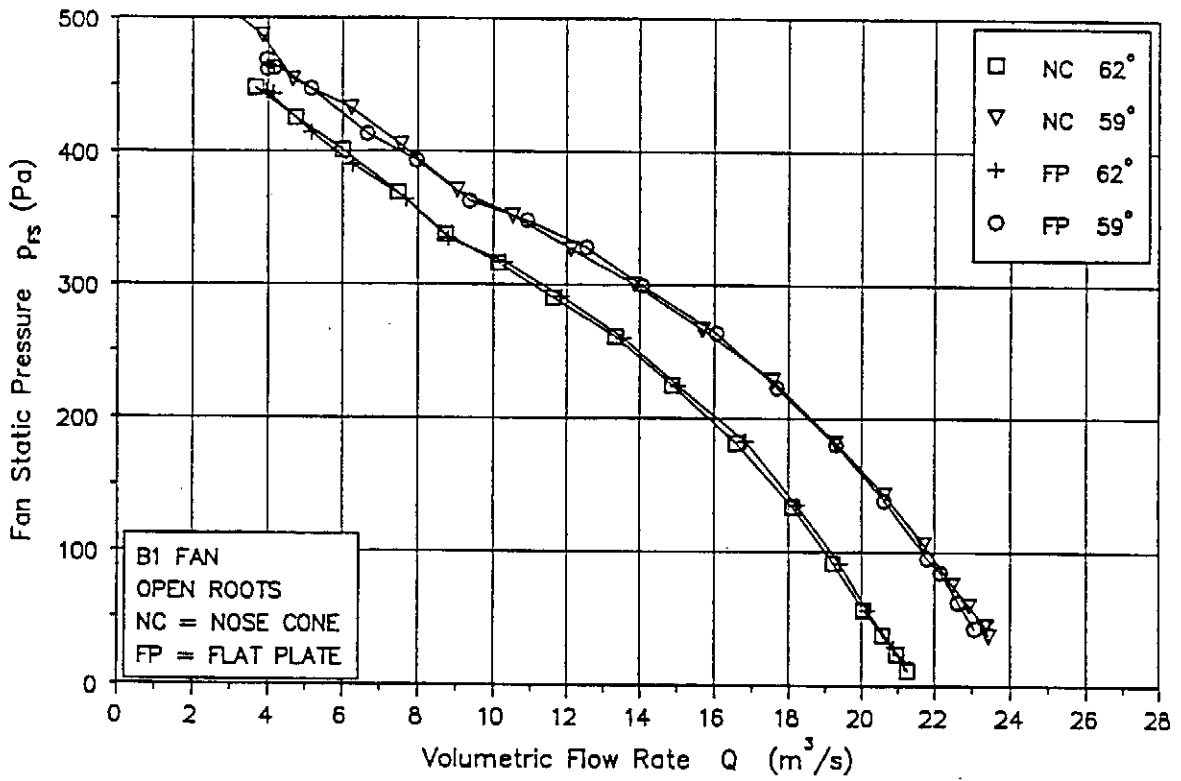
Figure 5.16 Effects of nose cone, B1 pressure characteristic
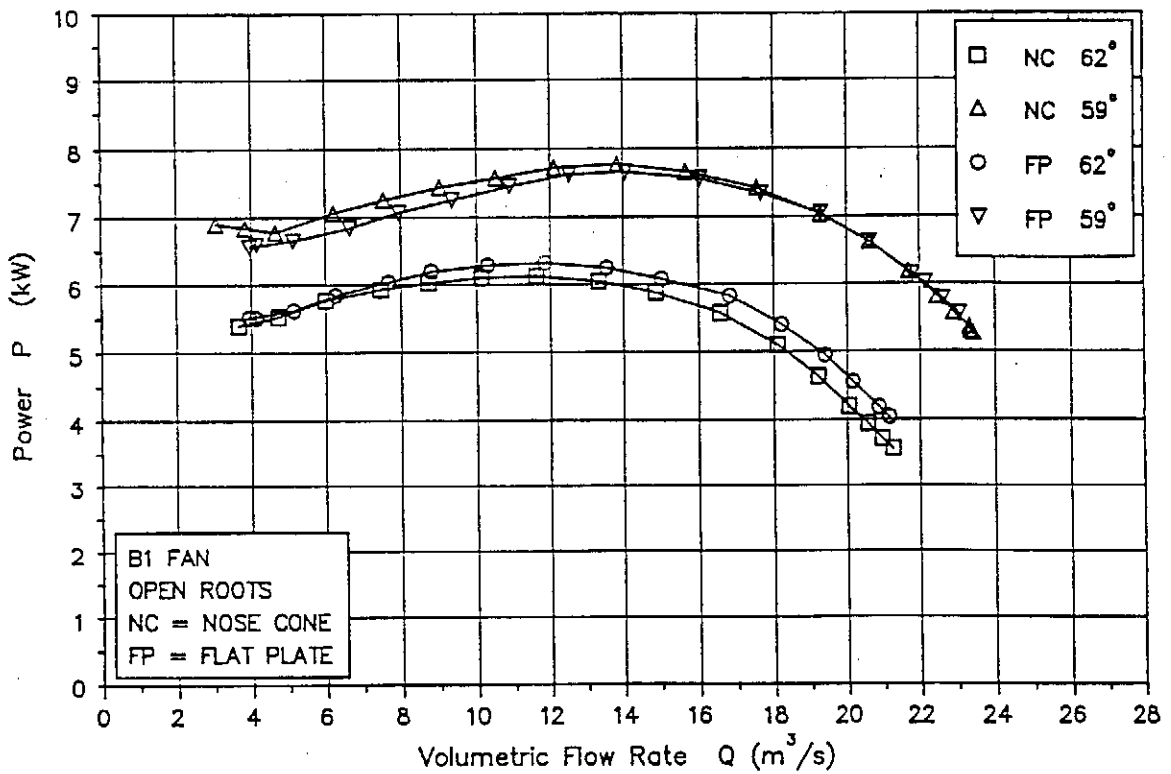
Figure 5.17 Effects of nose cone, B1 power characteristic
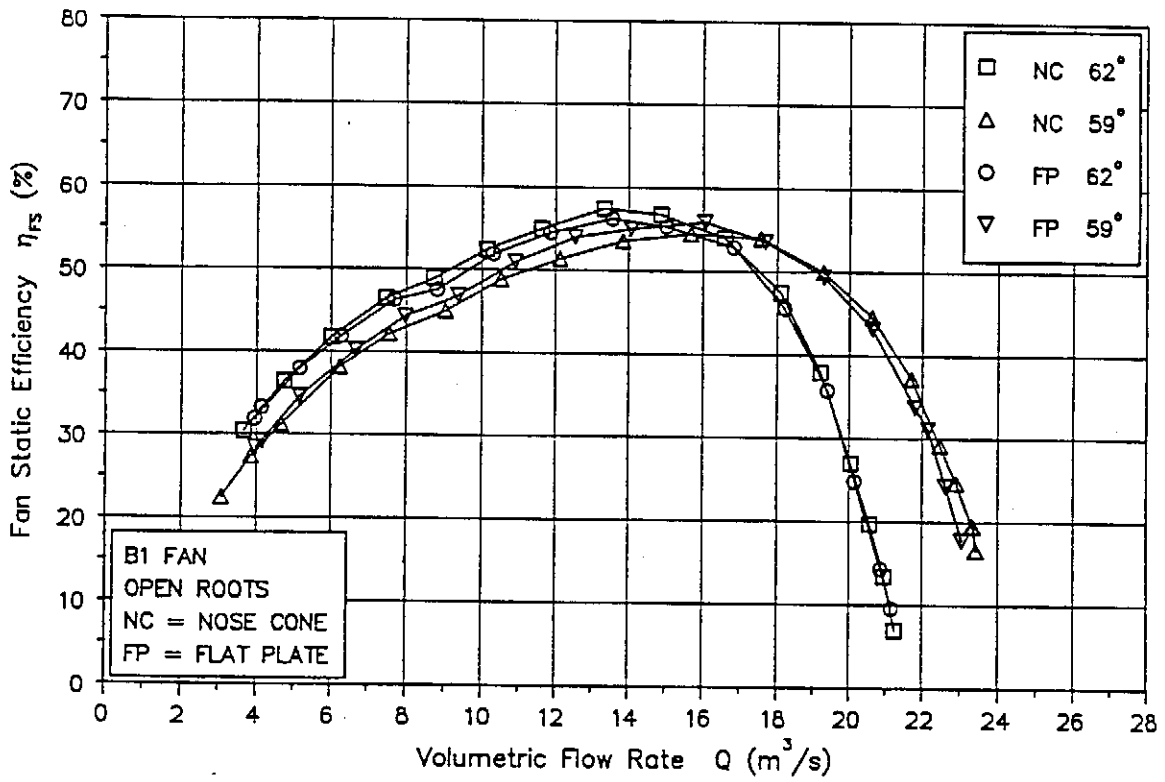
Figure 5.18   Effects of nose cone, B1 efficiency characteristic
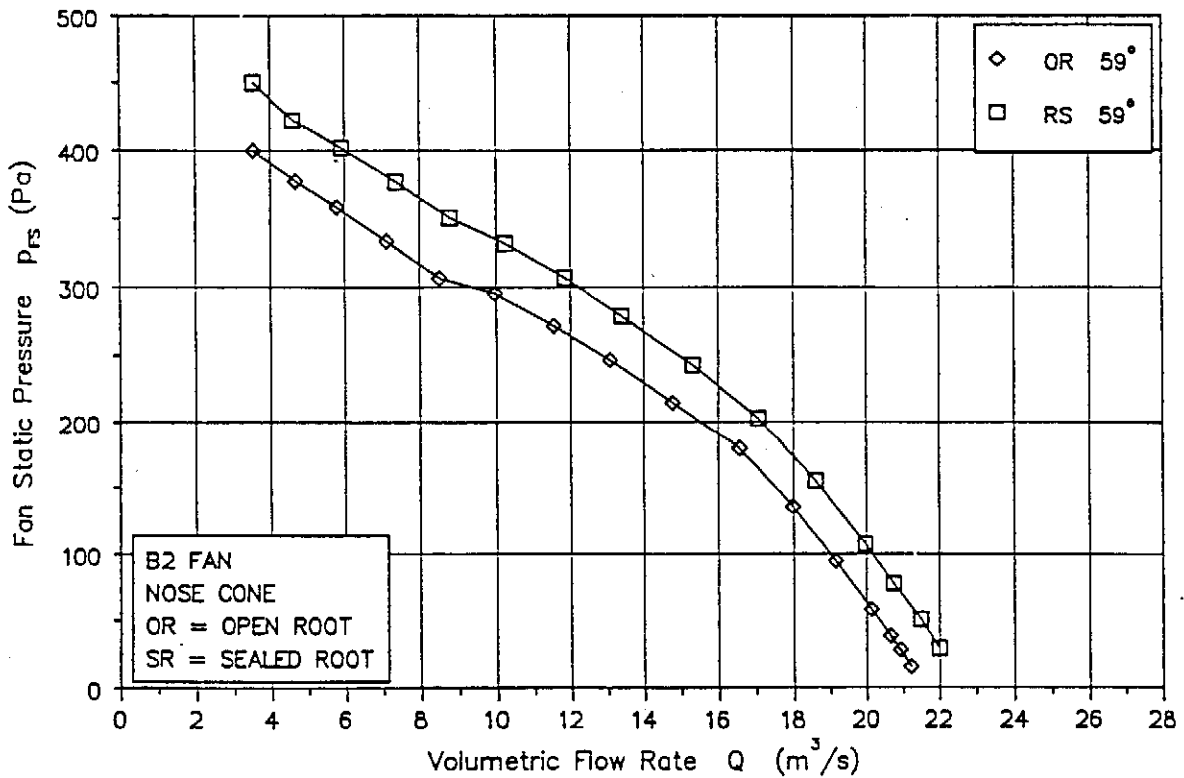
Figure 5.19   Effects of root seals, B2 pressure characteristic
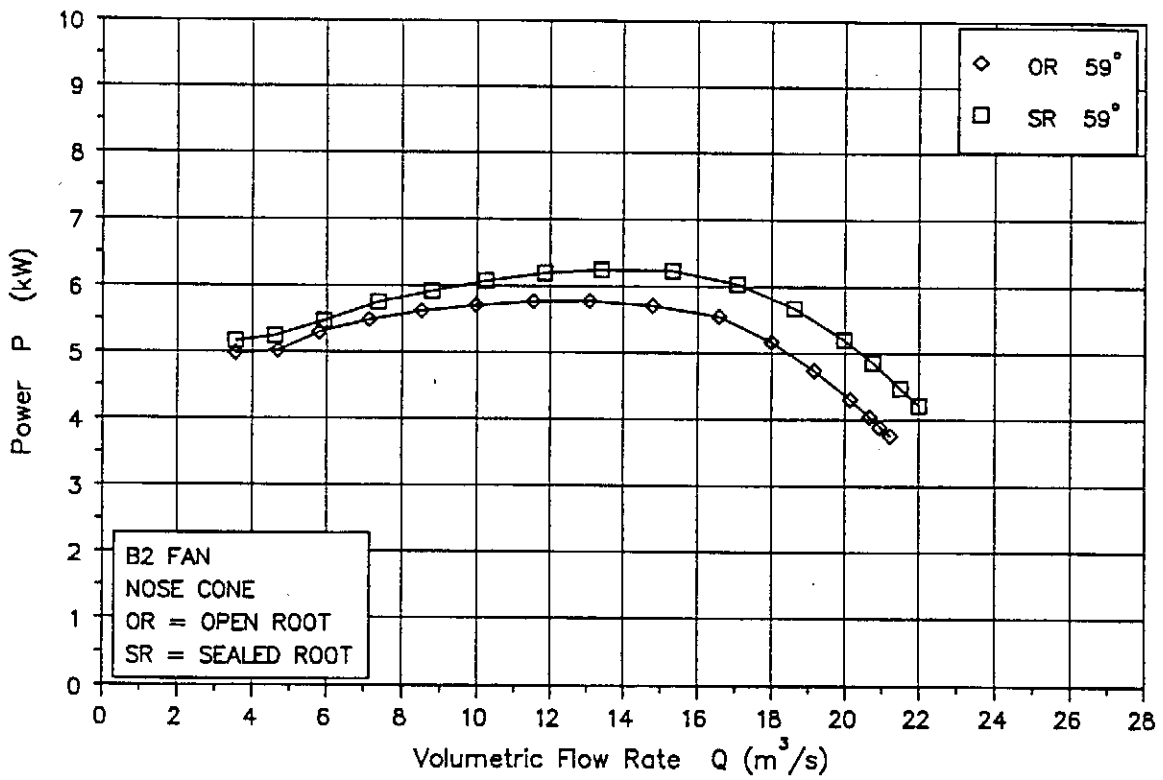
Figure 5.20 Effects of root seals, B2 power characteristic
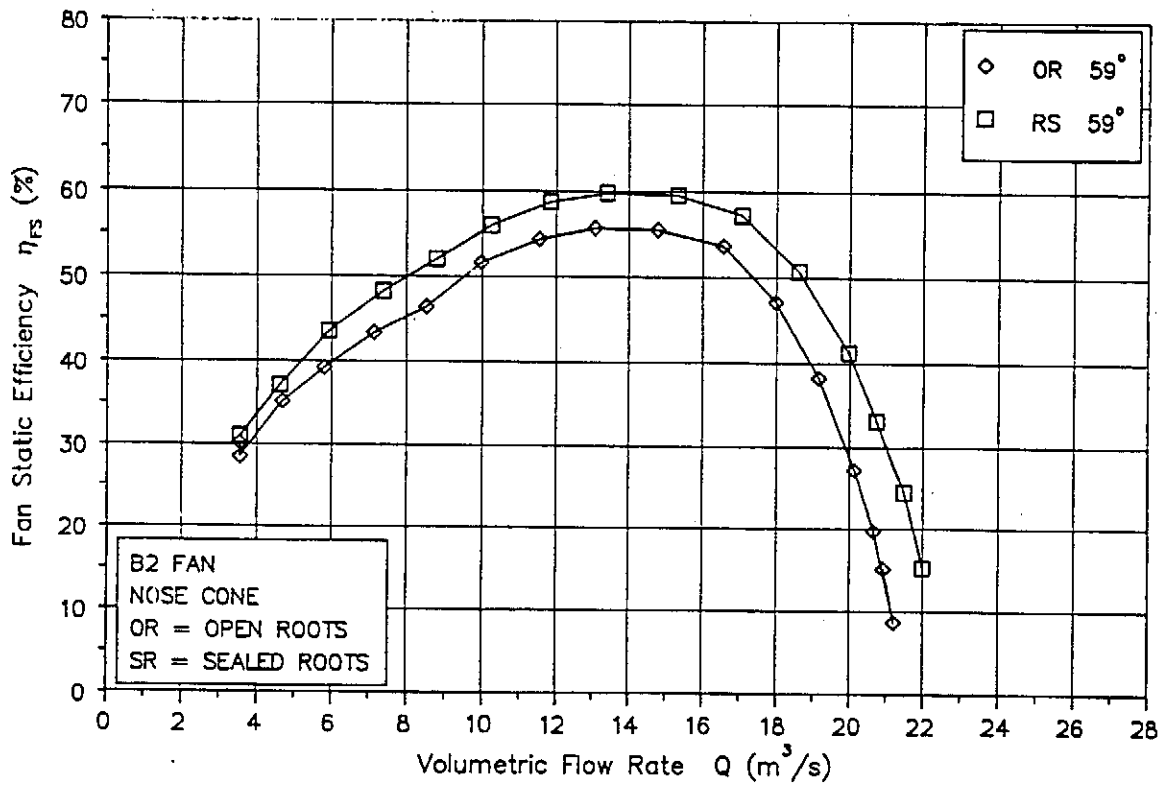
Figure 5.21 Effects of root seals, B2 efficiency characteristic
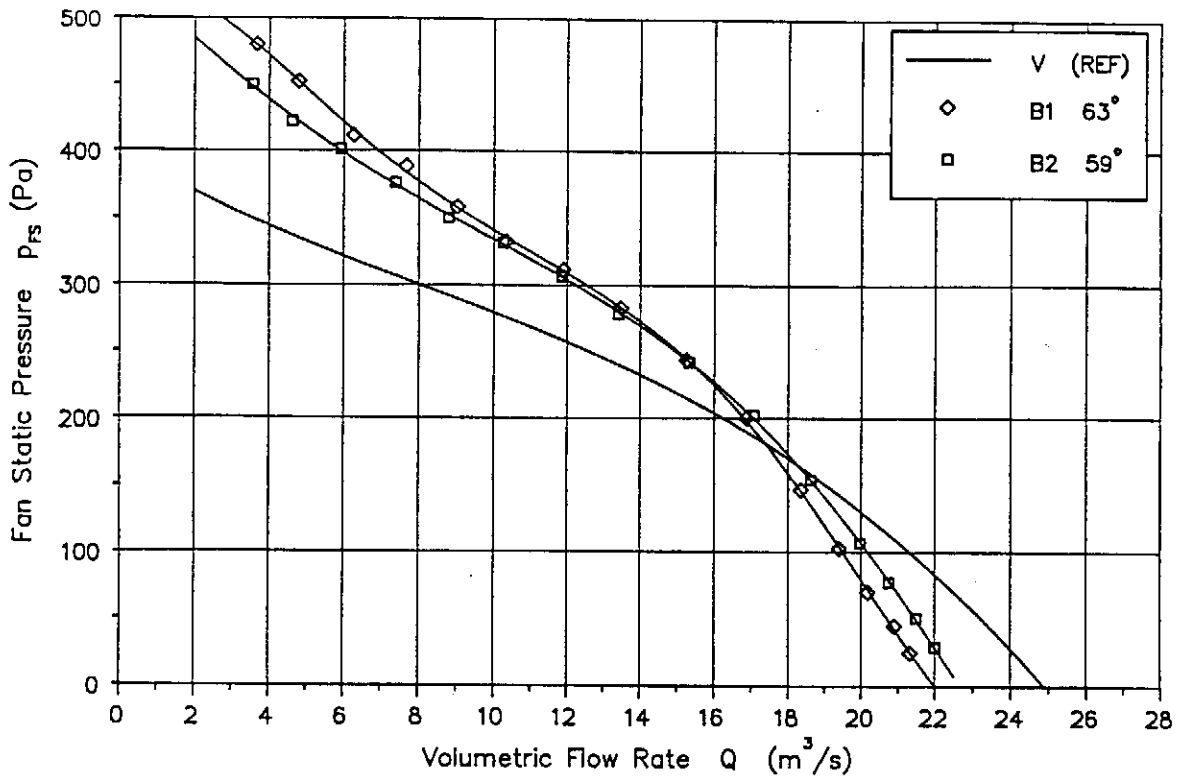
Figure 5.22 V, B1 and B2 comparison, pressure charac-
teristic
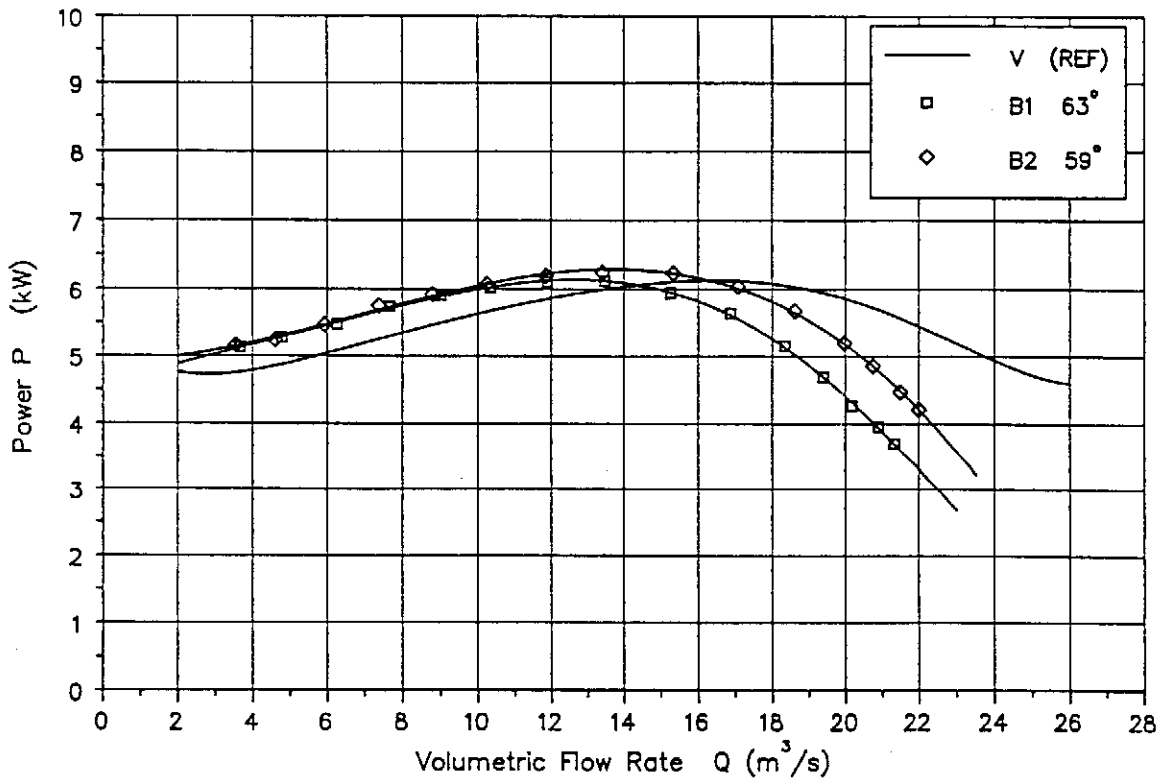
Figure 5.23 V, B1 and B2 comparison, power character-
istic
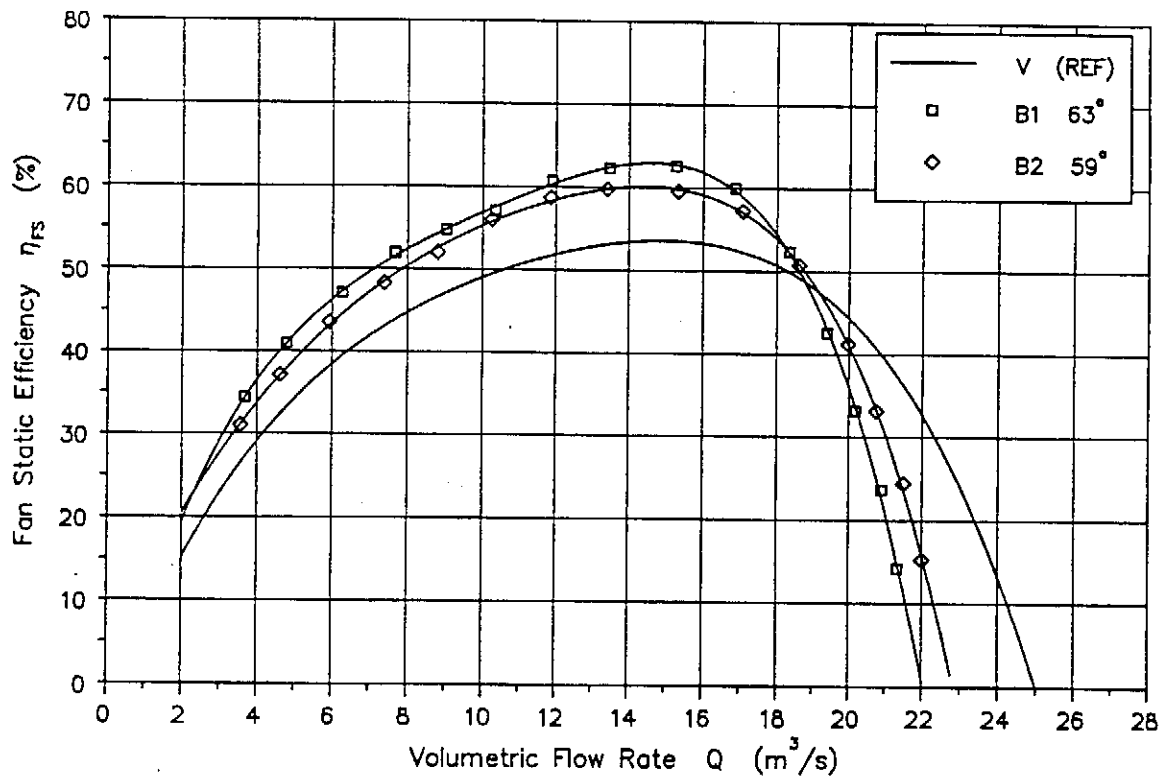
Figure 5.24 V, B1 and B2 comparison, efficiency char-
acteristic
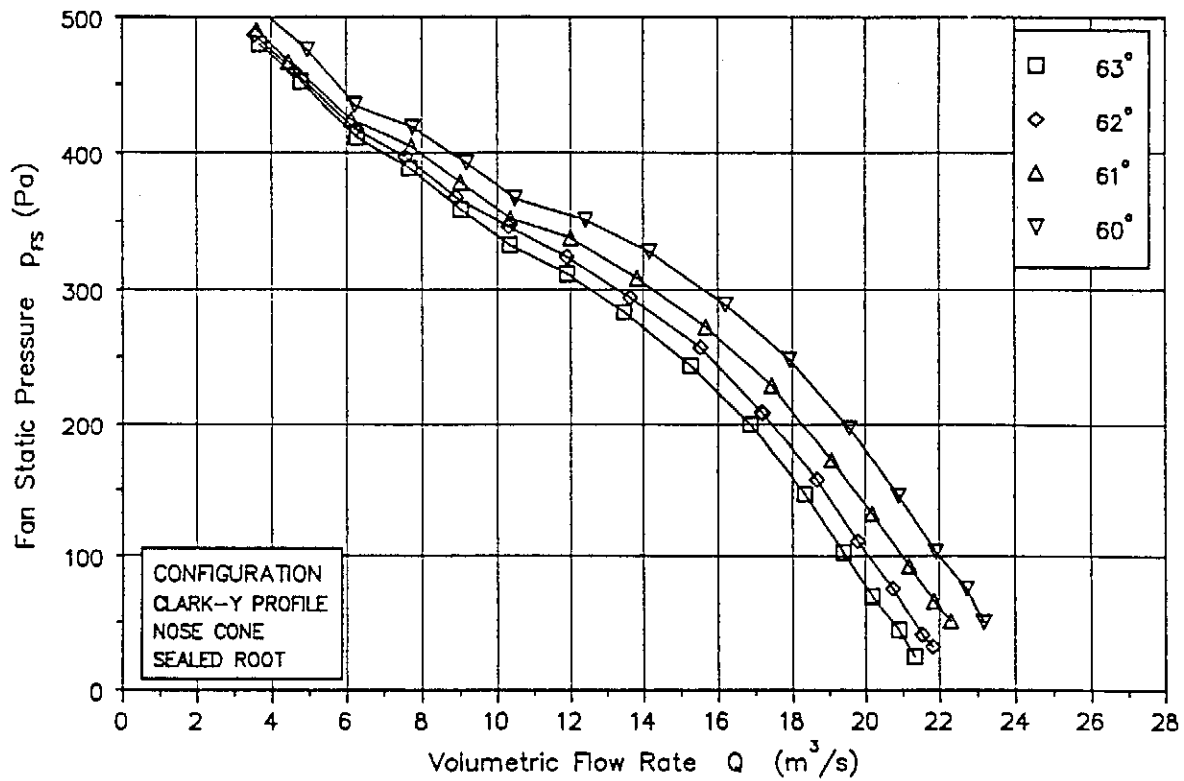
Figure 5.25 B1 pressure characteristic, sealed root
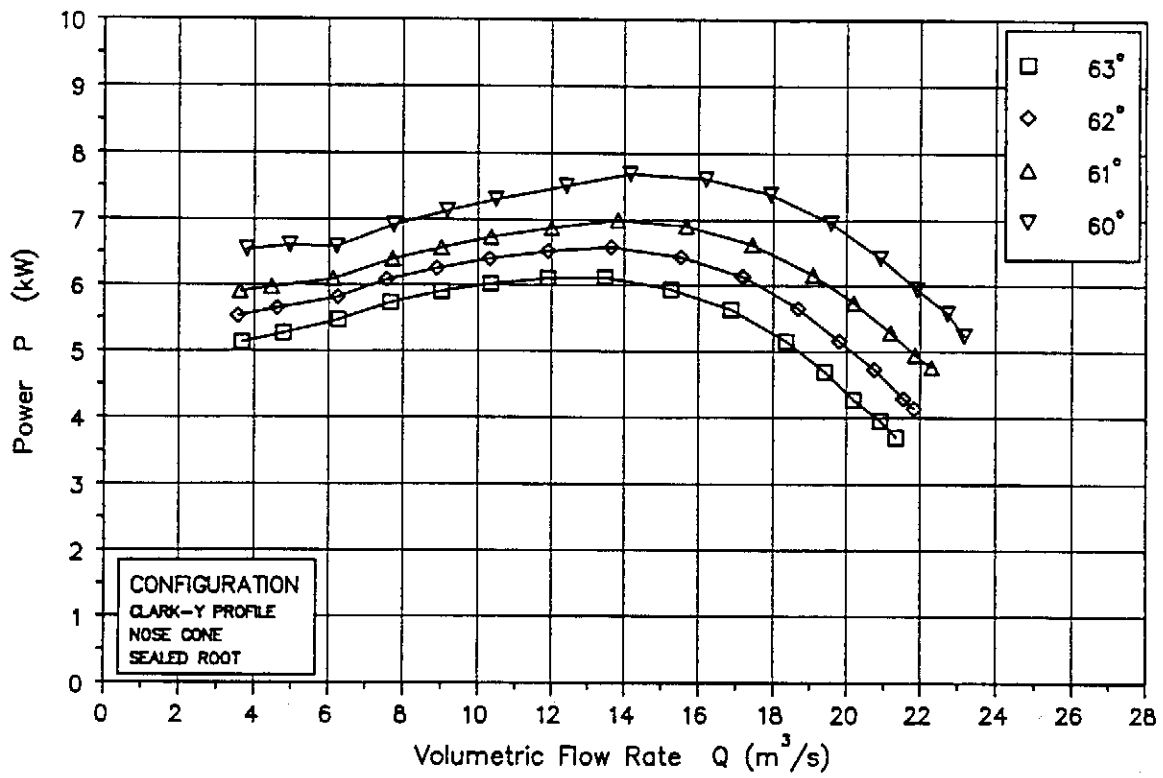
Figure 5.26 B1 power characteristic, sealed root
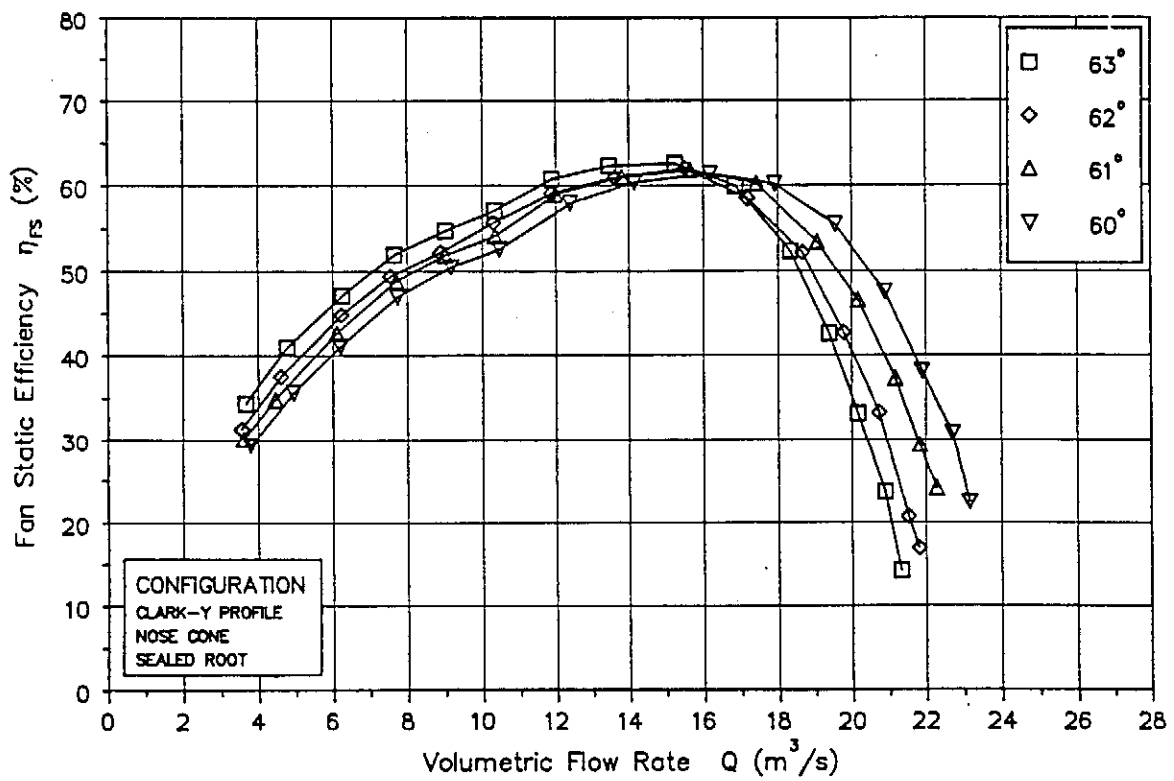
Figure 5.27 B1 efficiency characteristic, sealed root
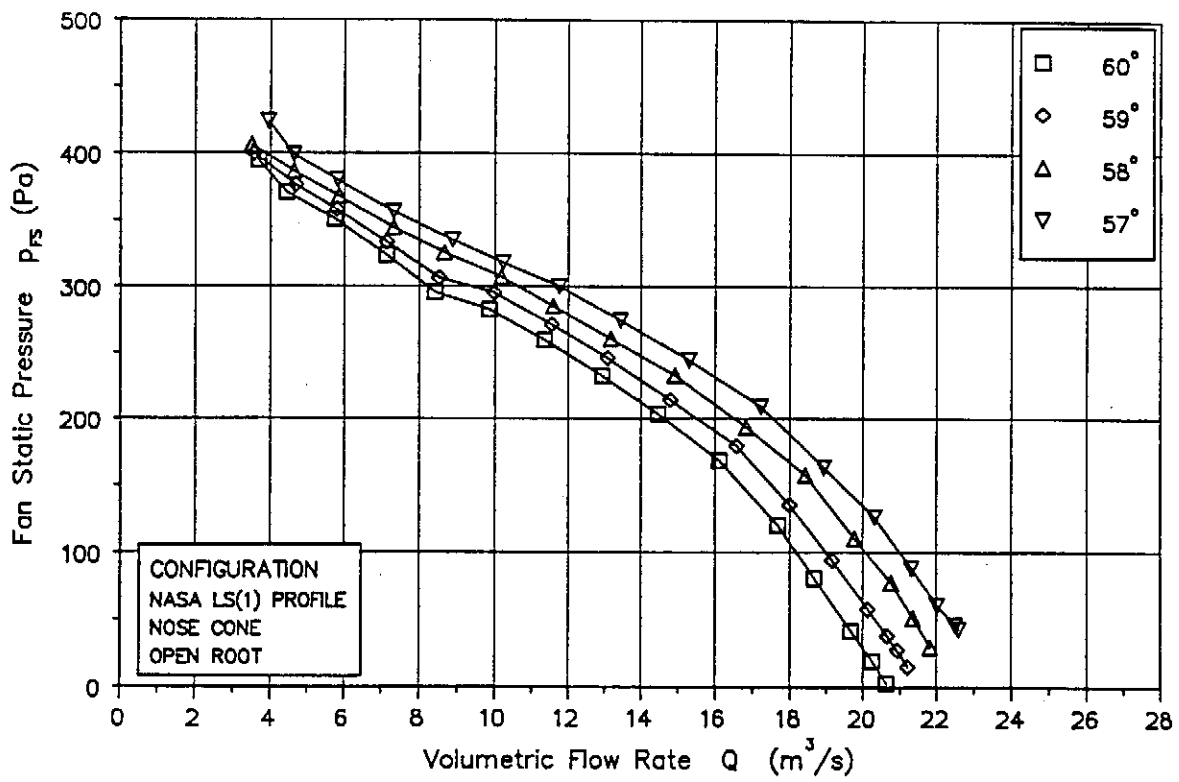
Figure 5.28 B2 pressure characteristic, open root
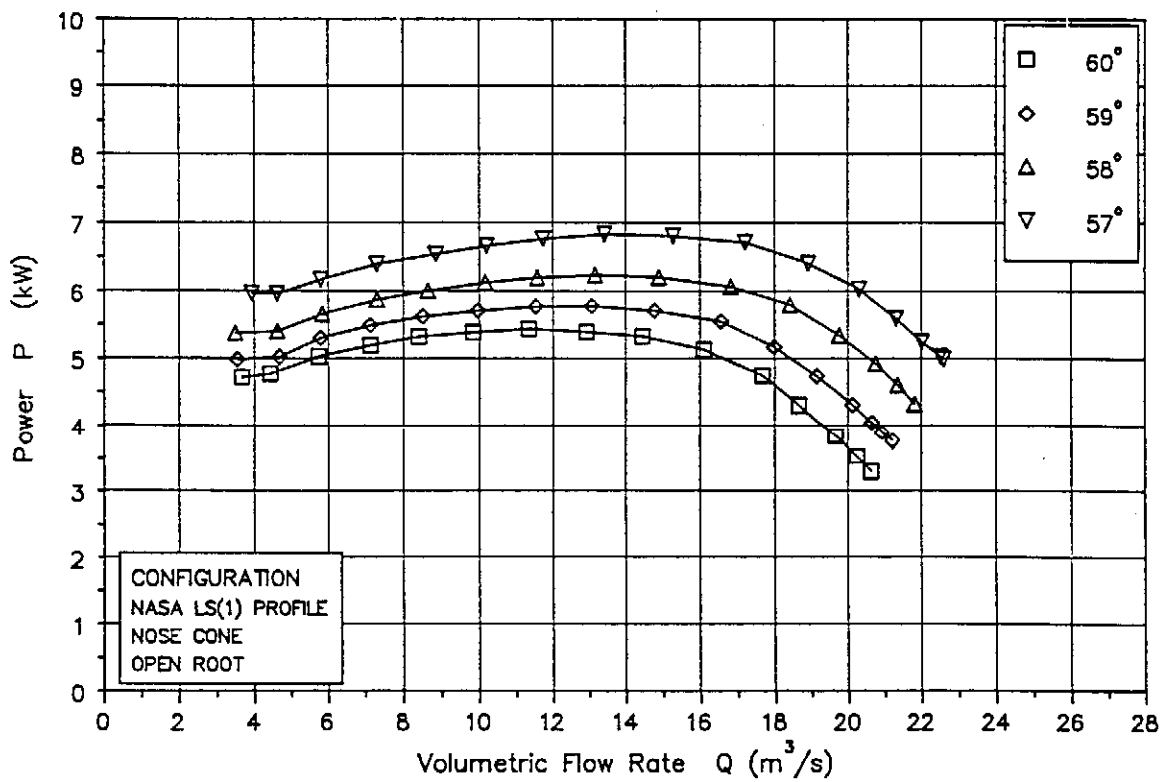
Figure 5.29 B2 power characteristic, open root
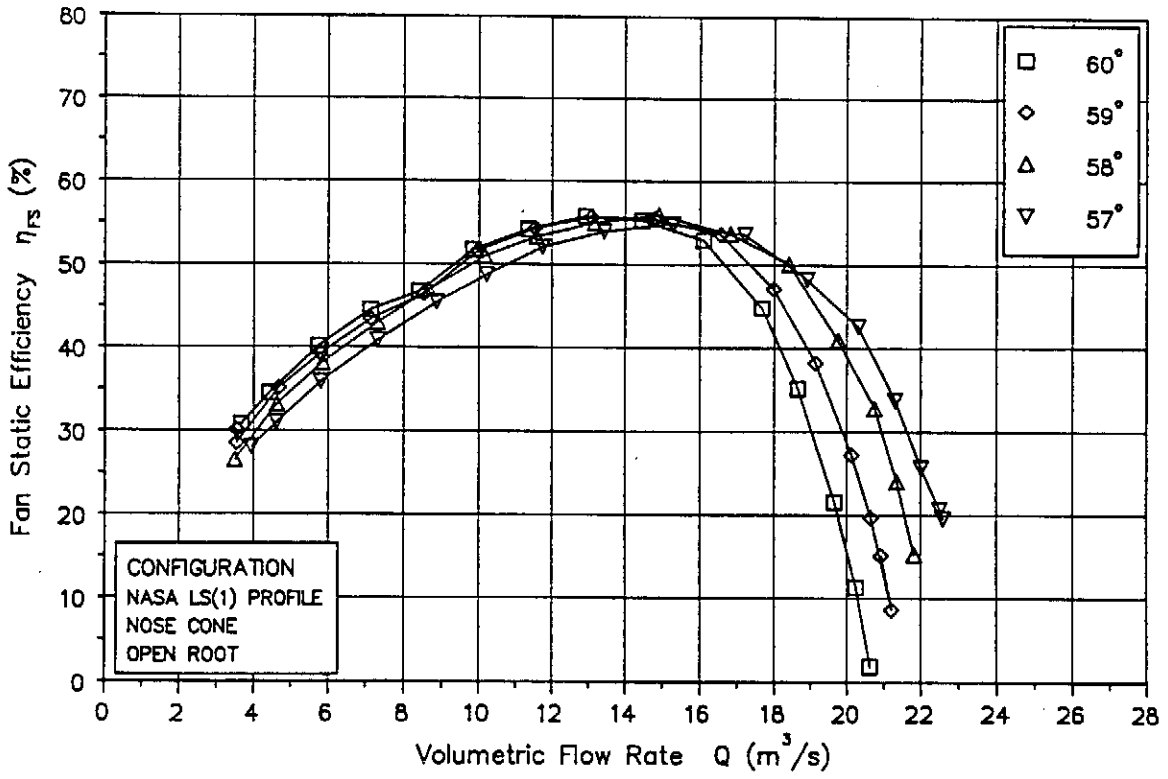
Figure 5.30 B2 efficiency characteristic, open root
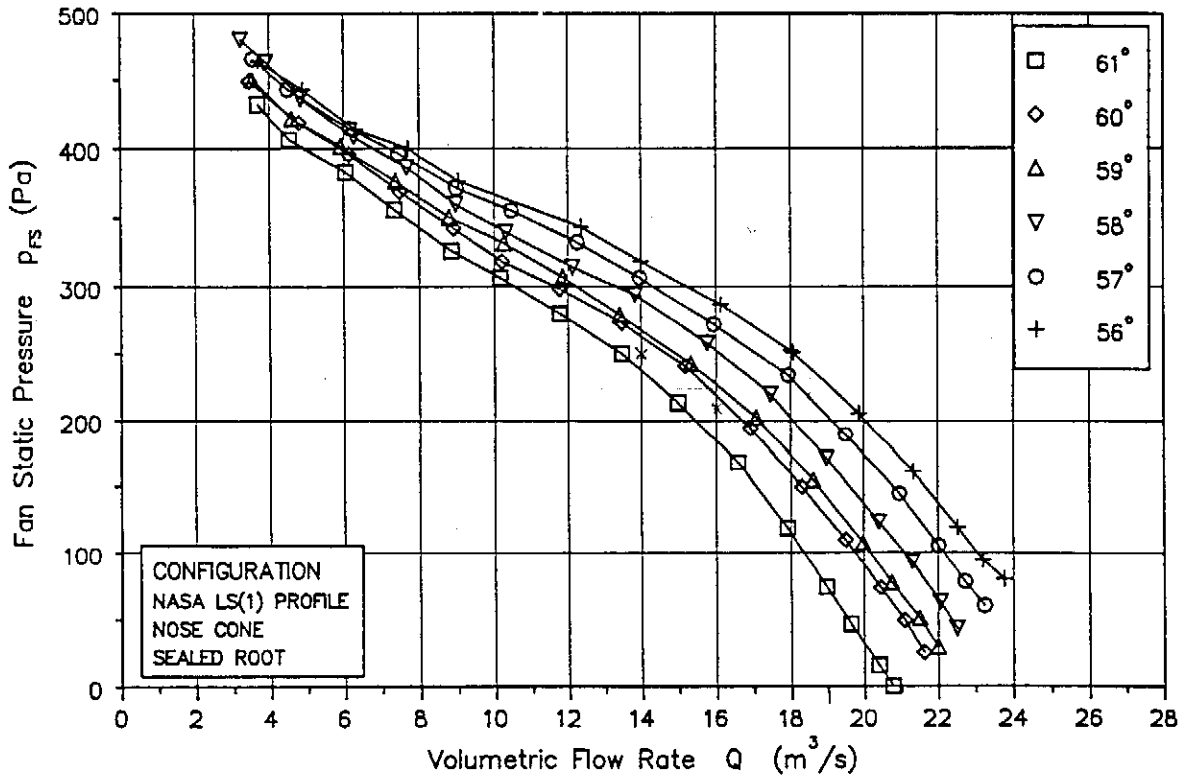
Figure 5.31 B2 pressure characteristic, sealed root

115
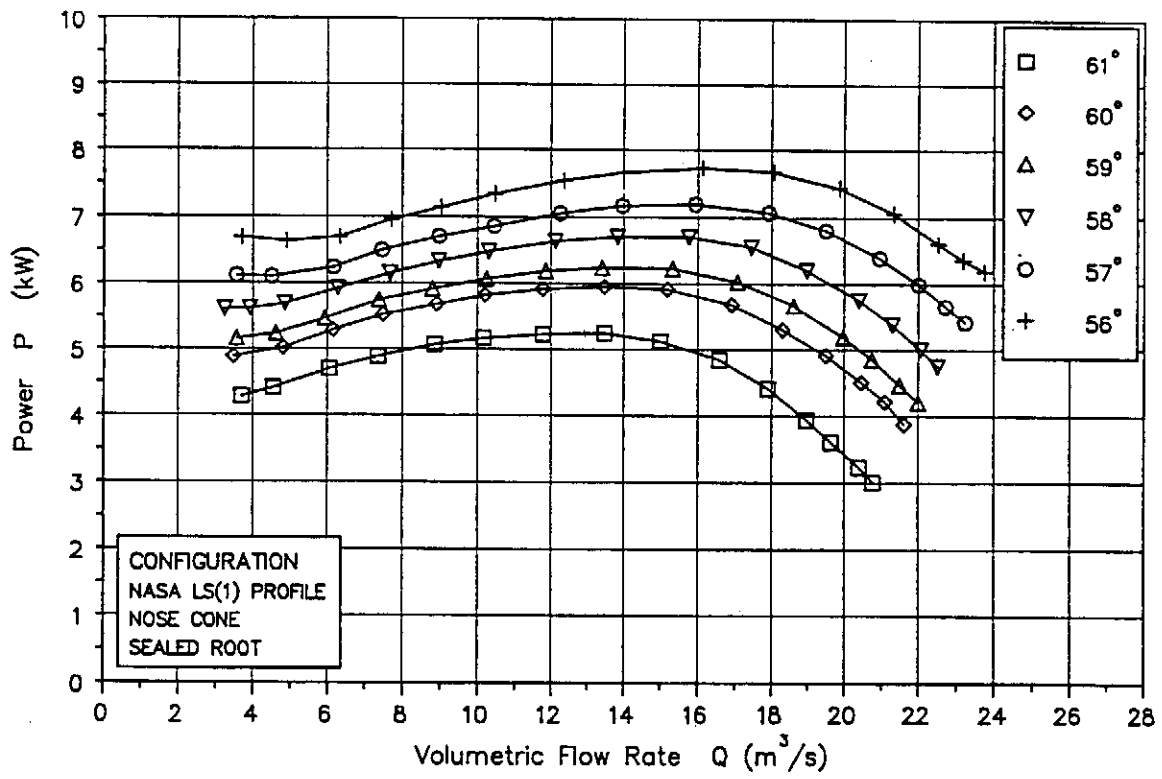
Figure 5.32 B2 power characteristic, sealed root
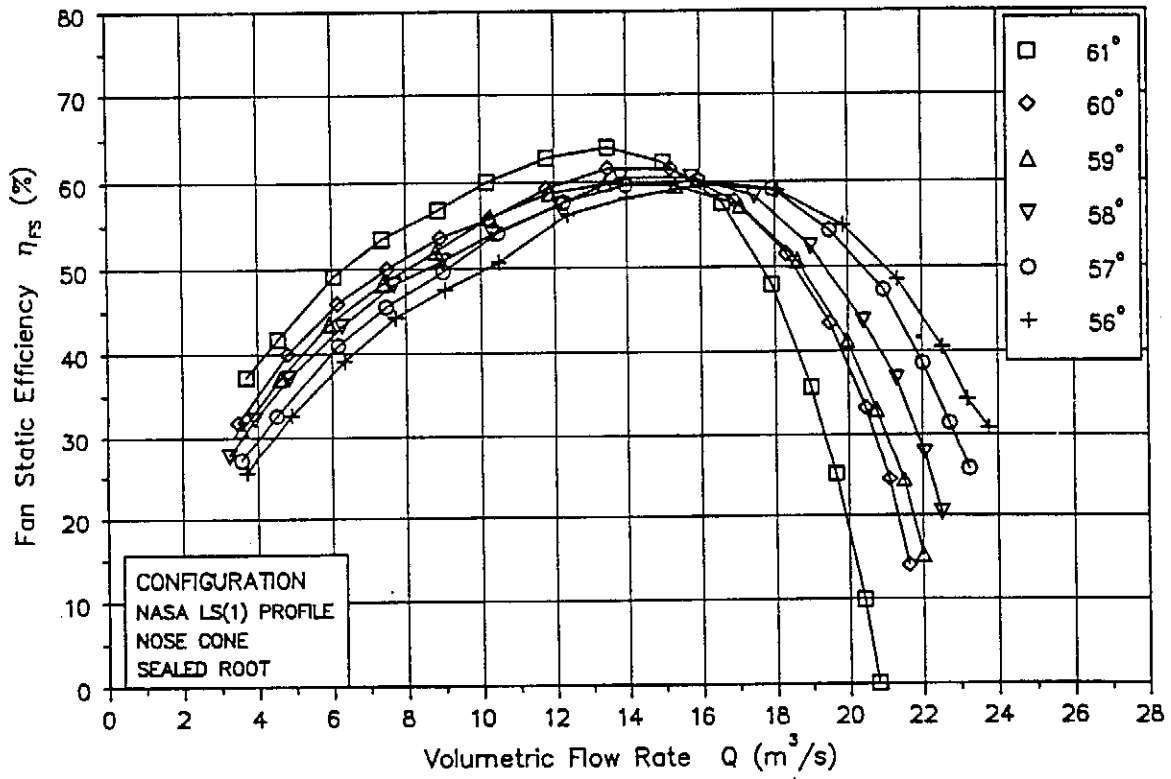
Figure 5.33 B2 efficiency characteristic, sealed root

116

APPENDIX A. DERIVATION OF THE EXIT AXIAL VELOCITY EQUATION

The indirect design approach requires the specification of an exit swirl distribution after which the SREE is solved for the axial exit velocity distribution. When the swirl and axial exit velocity distributions are known, all velocity triangle components and averaged performance parameters may be deduced therefrom.

Substituting the assumption of the general exponential swirl distribution

$$c_{\theta_2} = a r^n \qquad\qquad \text{A 1}$$

into SREE(3),

$$\frac{1}{\rho}\frac{dp_o}{dr} = \frac{c_\theta}{r}\frac{d}{dr}(r c_\theta) + c_x \frac{dc_x}{dr} \qquad\qquad \text{A 2}$$

yields the following expression :

$$\frac{1}{\rho} dp_o = a^2(n+1) r^{2n-1} dr + c_{x_2} dc_{x_2} \qquad\qquad \text{A 3}$$

Assuming constant density and integrating between the limits r_h and r solving for c_{x_2} gives :

$$c_{x_2}(r) = \sqrt{2\left(\frac{p_{o2}(r) - p_{o2}(r_h)}{\rho}\right) - R(r)a^2(n+1) + c_{x_2}^2(r_h)} \qquad\qquad \text{A 4}$$

where

$$R(r) = \ln\left(\frac{r}{r_h}\right)^2 \qquad for \quad n = 0 \qquad\qquad \text{A 5}$$

A.1

$$R(r) = \frac{r^{2n} - r_h^{2n}}{n} \qquad for \quad n \neq 0$$

A 6

$c_{x_2}(r_h) =$ the axial exit velocity at the hub radius

A 7

$p_{o_2}(r_h) =$ the total pressure at the hub radius

A 8

At this point, neither the value of $c_{x_2}(r_h)$ nor the total pressure distribution $p_{o2}(r)$ are known.

The Euler work equation which relates the specific work done on a mass of fluid to the changes in radius and angular velocity is given by :

$$W = \Omega(r_2 c_{\theta_2} - r_1 c_{\theta_1})$$

A 9

where the subscripts 1 and 2 denote stations 1 and 2 in Figure 2.2 respectively. The Euler work equation applies along any streamline through the fan rotor and in the case of a rotor only fan, the absolute inlet velocity is assumed to be axial and constant across the inlet at station 1 and the swirl component is zero, ie

$$c_1 = c_{x_1} = constant$$

A 10

$$c_{\theta_1} = 0$$

A 11

The specific work may also be expressed in terms of the total enthalpy change

$$W = h_{o_2} - h_{o_1}$$

A 12

which on expansion provides

$$W = u_2 + \frac{p_2}{\rho} + \frac{1}{2}c_2^2 \quad - \quad u_1 - \frac{p_1}{\rho} - \frac{1}{2}c_1^2$$

A 13

Since the flow through the fan is assumed incompressible and isentropic, there are no sensible changes in static temperature and the internal energies u_1 and u_2 are identical. Therefore,

$$W = \frac{p_{o_2} - p_{o_1}}{\rho}$$

A 14

Combining equations A.9 and A.14 gives

$$\frac{p_{o_2}}{\rho} = \frac{p_{o_1}}{\rho} + \Omega r c_{\theta_2}$$

A 15

Thus, at the hub radius,

$$W = \frac{p_{o_2}(r) - p_{o_2}(r_h)}{\rho} = \Omega(r c_{\theta_2}(r) - r_h c_{\theta_2}(r_h)) = \Omega a (r^{n+1} - r_h^{n+1})$$

A 16

Substituting into the expression for the axial exit velocity, Equation A.4 yields :

$$c_{x_2} = \sqrt{2 a \Omega (r^{n+1} - r_h^{n+1}) - R(r) a^2 (n+1) + c_{x_2}^2(r_h)}$$

A 17

This expression is written in terms of known parameters but must be solved iteratively because of the inclusion of $c_{x_2}(r_h)$ under the square root. A value for $c_{x_2}(r_h)$ is guessed and the corresponding radial distribution of c_{x_2} is calculated. The

correct value of $c_{x_2}(r_h)$ (and the ensuing radial distribution of axial exit velocity) is obtained when compatibility with the continuity relationship is achieved, ie

$$\frac{\dot{m}}{2\pi\rho} = \int_{r_h}^{r_t} c_{x_2} r \, dr \qquad \text{A 18}$$

APPENDIX B. FAN OPTIMISATION

1.1 Van Niekerks Optimisation Method

Van Niekerk (1958) presents a method for optimising the design of axial flow fans of the inlet guide vane and flow straightener type. The primary limitations and assumptions are that of a free vortex swirl distribution and the absence of interference effects, this latter condition implying that the solidity of the fan blading is sufficiently low everywhere to permit the use of free aerofoil lift/drag data. Van Niekerk does however suggest that the method can be extended to the arbitrary swirl distribution and high solidity cases. In his paper, Van Niekerk presents his method in terms of both the inlet guide vane and flow straightener configurations although here, only the flow straightener method is described because of its direct application to the rotor only configuration of interest in this study.

Considering a fan blade to be made up from an infinite number of two dimensional profile sections (or blade elements) and utilising the momentum theorem, Van Niekerk initially derives a blade element efficiency of the form

$$(1 - \eta_b) = \frac{\tan \gamma}{1 + \tan \beta_m \tan \gamma} \cdot \left[\frac{U}{c_x} - \frac{c_{\theta_2}}{c_x} + \frac{c_x}{U} \right] \qquad \text{B 1}$$

which, as shown below, is equivalent to that derived by Dixon (1978), namely

$$\eta_b = \left(\frac{c_x}{U} \right) \tan (\beta_m - \gamma) + \left(\frac{c_{\theta_2}}{2U} \right) \qquad \text{B 2}$$

Equation B2 can be rewritten

$$1 - \eta_b = \left(1 - \frac{c_{\theta_2}}{2U} \right) - \left(\frac{c_x}{U} \right) \tan(\beta_m - \gamma) \qquad \text{B 3}$$

and from the velocity triangle depicted in Figure B1, have that

$$\left(1 - \frac{c_{\theta_2}}{2U} \right) = \left(\frac{c_x}{U} \right) \tan \beta_m \qquad \text{B 4}$$

to give

$$(1 - \eta_b) = \left(\frac{c_x}{U} \right) [\tan \beta_m - \tan(\beta_m - \gamma)] \qquad \text{B 5}$$

The term in square brackets,

$$[\tan \beta_m - \tan(\beta_m - \gamma)] \qquad \text{B 6}$$

expands to

$$\frac{\tan \gamma (\tan^2 \beta_m + 1)}{1 + \tan \beta_m \tan \gamma} \qquad \text{B 7}$$

Now since

$$\tan \beta_m = \frac{U}{c_x} - \frac{c_{\theta_2}}{2 c_x} \qquad \text{B 8}$$

then

$$\tan^2 \beta_m + 1 = \left(\frac{U}{c_x} \right) \left[\frac{U}{c_x} - \frac{c_{\theta_2}}{c_x} + \left(\frac{c_x}{U} \right) \left(\frac{c_{\theta_2}}{2 c_x} \right)^2 + \frac{c_x}{U} \right] \qquad \text{B 9}$$

B.2

Van Niekerk neglects the product

$$\left(\frac{c_x}{U}\right)\left(\frac{c_{\theta_2}}{2c_x}\right)^2 \qquad \qquad \text{B 10}$$

stating that it is second order, to yield

$$\tan^2\beta_m + 1 \;=\; \left(\frac{U}{c_x}\right)\left[\frac{U}{c_x} - \frac{c_{\theta_2}}{c_x} + \frac{c_x}{U}\right] \qquad \text{B 11}$$

Substitution into Equation B5 gives

$$(1 - \eta_b) = \frac{\tan\gamma}{1 + \tan\beta_m \tan\gamma} \cdot \left[\frac{U}{c_x} - \frac{c_{\theta_2}}{c_x} + \frac{c_x}{U}\right] \qquad \text{B 12}$$

as required. This blade element efficiency is essentially a total to total efficiency at a particular radial station.

Whilst the term expressed in Equation B10 is indeed small for moderate values of hub swirl factor ($c_{\theta_2}/c_x \leq 0.9$), the validity of neglecting the product for higher swirl factors is questionable, as illustrated in the following example.

For a hub/tip ratio of 0.4 and a hub swirl factor of 1.1 the data of Table B3 provides the following values for the terms in Equation B9 at the hub :

$$c_x \;=\; 10.2 \ m/s$$

$$U \;=\; \Omega r \;=\; 78.54 \times 0.308 \;=\; 24.19 \ m/s$$

$$\frac{c_x}{U} \;=\; 0.422$$

$$\frac{U}{c_x} \;=\; 2.372$$

$$\left(\frac{c_x}{U}\right)\left(\frac{c_{\theta_2}}{2c_x}\right)^2 = 0.127$$

The term in the square brackets of Equation B9 when including the product $\left(\frac{c_x}{U}\right)(c_{\theta_2}/2c_x)^2$ gives a value of 1.822. When the product is neglected the value is 1.694, indicating a difference of 7.556%.

One of the significant features of the Van Niekerk method is the introduction of annulus losses for the optimisation of fan parameters. Since the sum of all the fan losses reduces the theoretical or ideal pressure rise, the effective pressure rise is written

$$\Delta p_o = \eta_{tt} \Delta p_{o_{th}} \qquad \qquad \text{B 13}$$

where η_{tt} is the overall fan total to total efficiency.

Fan losses are assumed to be made up of blade profile losses, stator losses and diffuser losses. Instead of incorporating these components together, Van Niekerk separates those losses that do not depend directly on the action of the fan blading, eg those that arise as a result of friction and flow separation on the annular fan shroud, expressing this as

$$\Delta p_o = \Delta p_{o_{th}} - annulus \ losses - blade \ losses \qquad \text{B 14}$$

where "blade losses" involve the blade element efficiency and "annulus losses" are associated with stator vanes, the fan shroud surfaces and exit diffuser components.

B.4

If the hub/tip ratio is not considered as a dependent variable, but held constant at different values, then the annulus efficiency is introduced in such a way that for any fan having a particular hub/tip ratio, then

$$\Delta p_o = \Delta p_{o_{th}} - (1 - \eta_a)\frac{1}{2}\rho c_x^2 - (1 - \eta_b)_{avg} \Delta p_{o_{th}}$$

B 15

The annulus losses are defined in terms of the axial velocity since for a fixed x_b, η_{tt} is constant. Neglecting scale effects, the annulus efficiency is dependent only on the shape and surface roughness of the stator blades, inner and outer shrouding and the exit diffuser, if present. The component of the annulus efficiency associated with the stators is constant because the design swirl coefficient is limited in such a way that it will always be the same for any fan having a particular annulus geometry.

Since η_a refers only to losses that are associated with the dynamic pressure through the annulus, the above equation does not include boundary layer separation effects at the hub, nor secondary losses. Van Niekerk notes that although these losses are relatively small, they can be included in either of the annulus or blade losses. Evaluation of η_a and the adjustment to η_b allow for secondary losses is difficult and must be estimated roughly or determined experimentally.

Making the generally accepted assumption that $\tan\gamma \ll 1$ and that $\tan\beta_m$ is $O(1)$, the expression for the blade element efficiency (Equation B12) may be approximated by

$$(1 - \eta_b) = \tan\gamma \left[\frac{U}{c_x} - \frac{c_{\theta_2}}{c_x} + \frac{c_x}{U} \right]$$

B 16

The average blade element efficiency across the blade span is
then obtained by integrating along the blade from hub to tip
as follows

$$
(1 - \eta_b)_{avg} = \frac{\int_{r_h}^{r_t} (1 - \eta_b).r.dr}{\int_{r_h}^{r_t} r.dr}
$$

B 17

Now

$$
\int_{r_h}^{r_t} r.dr \;=\; \frac{r_t^2}{2}(1 - x_b^2)
$$

B 18

and

$$
\int_{r_h}^{r_t} (1 - \eta_b).r.dr \;=\; (\tan \gamma)_{avg} \int_{r_h}^{r_t} \left[\left(\frac{U}{c_x}\right) - \left(\frac{c_\theta}{c_x}\right) + \left(\frac{c_x}{U}\right) \right] r.dr
$$

B 19

$$
=\; (\tan \gamma)_{avg} \left\{ \frac{\Omega r_t^3}{3 c_x}(1 - x_b^3) \;+\; r_t(1 - x_b)\left[\frac{c_x}{\Omega} - \frac{k}{c_x} \right] \right\}
$$

Using the definitions

$$
\phi_t = \frac{c_x}{U_t}, \qquad c_\theta(r_h) = \frac{k}{r_h}, \qquad \epsilon_h = \frac{c_\theta(r_h)}{c_x}
$$

B 20

and simplifying results in

$$
(1 - \eta_b)_{avg} = \frac{2}{3} \frac{(\tan \gamma)_{avg}}{\phi_t} \frac{(1 - x_b^3)}{(1 - x_b^2)} \;+\; \frac{2(\tan \gamma)_{avg}[\phi_t - \epsilon_h x_b]}{(1 + x_b)}
$$

B 21

B.6

Now dividing both sides of Equation B15 by $\Delta p_{o_{th}}$ gives

$$\frac{\Delta p_o}{\Delta p_{o_{th}}} = \eta_{tt} = 1 - \frac{(1-\eta_a)\frac{1}{2}\rho c_x^2}{\Delta p_{o_{th}}} - (1-\eta_b)_{avg} \qquad \text{B 22}$$

Since the theoretical total pressure rise is given by

$$\Delta p_{o_{th}} = \rho U_t c_\theta(r_h) x_b \qquad \text{B 23}$$

the expression for the total to total efficiency simplifies to

$$(1-\eta_{tt}) = (1-\eta_b)_{avg} + (1-\eta_a)\frac{\phi_t}{2\epsilon_h x_b} . \qquad \text{B 24}$$

Finally, by including the expression for the averaged blade element efficiency, the following equation is obtained :

$$(1-\eta_{tt})_{avg} = \frac{2}{3}\frac{(\tan\gamma)_{avg}}{\phi_t}\frac{(1-x_b^3)}{(1-x_b^2)} + \frac{2(\tan\gamma)_{avg}[\phi_t-\epsilon_h x_b]}{(1+x_b)} + (1-\eta_a)\frac{\phi_t}{2\epsilon_h x_b} \qquad \text{B 25}$$

Since x_b, η_a and ϵ_h are constant for a fan of a given annulus and stator geometry, and $(\tan\gamma)_{avg}$ varies only slightly with changes in tip flow factor over the range in which the efficiency is fairly high, the expression for $(1-\eta_{tt})$ may be differentiated with respect to ϕ_t obtain the condition of minimum loss, ie putting

$$\frac{d(1-\eta_{tt})_{avg}}{d\phi_t} = \frac{(1-\eta_a)}{2\epsilon_h x_b} - \frac{2}{3}\frac{(\tan\gamma)_{avg}}{\phi_t^2}\frac{(1-x_b^3)}{(1-x_b^2)} + \frac{2(\tan\gamma)_{avg}}{(1+x_b)} = 0 \qquad \text{B 26}$$

Expanding and solving for the optimum tip flow factor provides

$$(\phi_t)_{opt} = \left[\frac{4\epsilon_h x_b(1 + x_b + x_b^2)(\tan \gamma_{avg})}{3(1 - \eta_a)(1 + x_b) + 12x_b(\tan \gamma)_{avg}} \right]^{\frac{1}{2}}$$

Because Van Niekerk is concerned with fans having either inlet guide vanes or flow straighteners, only the total to total efficiency is derived. However, in the case of the rotor only fans of interest here, the axial and swirl components of the exit velocity are not recovered in a diffuser or exit flow straighteners. It is therefore appropriate to consider the total to static efficiency as opposed to the total to total value. The following is an extension of Van Niekerks' method.

The dynamic pressure in the fan exit flow is given by

$$p_d = \frac{1}{2}\rho(c_\theta^2 + c_x^2)$$

which can be re-written as

$$p_d = \frac{1}{2}\rho\left(\frac{k^2}{r^2} + c_x^2\right)$$

As above, the average dynamic pressure across the radius is defined as

$$(p_d)_{avg} = \frac{\int_{r_h}^{r_t} \frac{1}{2}\rho(k^2/r^2 + c_x^2).r.dr}{\int_{r_h}^{r_t} r.dr}$$

$$= \frac{1}{2}\rho c_x^2 - \frac{\rho c_\theta^2(r_t)\ln(x_b)}{(1 - x_b^2)}$$

B.8

Again using the definitions of Equation B20, the expression is written

$$(p_d)_{avg} = \frac{1}{2}\rho c_x^2 \left[1 - 2(\epsilon_h x_b)^2 \cdot \frac{\ln(x_b)}{(1-x_b^2)} \right]$$

B 31

The static pressure rise is defined as is the total pressure rise, (Equation B15) except that the dynamic pressure component is subtracted, ie

$$\Delta p_{ts} = \Delta p_{o_{th}} - (1-\eta_a)\frac{1}{2}\rho c_x^2 - (1-\eta_b)_{avg}\Delta p_{o_{th}} - (p_d)_{avg}$$

B 32

The total to static efficiency is defined as the ratio of the static pressure rise to the theoretical total pressure rise which is identical to the total to total efficiency except for the last term

$$\frac{(p_d)_{avg}}{\Delta p_{o_{th}}} = \frac{\frac{1}{2}\rho c_x^2 [1 - 2(\epsilon_h x_b)^2 \cdot \ln(x_b)/(1-x_b^2)]}{\rho U_t x_b c_\theta(r_h)}$$

B 33

$$= \frac{\phi_t}{2\epsilon_h x_b}\left[1 - 2(\epsilon_h x_b)^2 \cdot \frac{\ln(x_b)}{(1-x_b^2)} \right]$$

The total to static efficiency in final form is therefore given by :

$$(1-\eta_{ts})_{avg} = \frac{2}{3}\frac{(\tan\gamma)_{avg}}{\phi_t}\frac{(1-x_b^3)}{(1-x_b^2)} + \frac{2(\tan\gamma)_{avg}[\phi_t - \epsilon_h x_b]}{(1+x_b)}$$

B 34

$$+ (1-\eta_a)\frac{\phi_t}{2\epsilon_h x_b} + \frac{\phi_t}{2\epsilon_h x_b}\left[1 - 2(\epsilon_h x_b)^2 \cdot \frac{\ln(x_b)}{(1-x_b^2)} \right]$$

The optimum tip flow factor is determined as follows :

$$\frac{d(1-\eta_{ts})_{avg}}{d\phi_t} = \frac{(1-\eta_a)}{2\epsilon_h x_b} - \frac{2}{3}\frac{(\tan\gamma)_{avg}}{\phi_t^2}\frac{(1-x_b^3)}{(1-x_b^2)} + \frac{2(\tan\gamma)_{avg}}{(1+x_b)}$$

$$+ \frac{1}{2\epsilon_h x_b}\left[1 - 2(\epsilon_h x_b)^2\cdot\frac{\ln(x_b)}{(1-x_b^2)}\right] = 0 \qquad \text{B 35}$$

Simplifying and rearranging gives :

$$(\phi_t)_{opt} = \left[\frac{\frac{4}{3}\epsilon_h x_b(1-x_b)(1+x_b+x_b^2)(\tan\gamma)_{avg}}{(1-x_b^2)(2-\eta_a)-2(\epsilon_h x_b)^2\ln(x_b)+4\epsilon_h x_b(1-x_b)(\tan\gamma)_{avg}}\right]^{\frac{1}{2}} \qquad \text{B 36}$$

1.2 Program FANOPT

Program FANOPT implements the Van Niekerk method described above, but since the design constraints include the rotational speed, volumetric flow rate and the tip radius, the tip flow factor is already determined. In the following, the efficiency and pressure rise are calculated as functions of the hub-tip ratio. In addition, the swirl factor is limited to the range 0.3 to 1.1, corresponding to absolute outlet flow angles 16.7° and 47.7° respectively.

The following parameters are specified by the user :

    i.   The range of hub-tip ratios to use

    ii.   The range of swirl factors to use

    iii. Volumetric flow rate

    iv.   Tip radius

    v.   Rotational speed

    vi.   Fluid density

    vii. Average drag/lift ratio for the aerofoil to be used $(\tan\gamma)_{avg}$

vii. Estimated value for the annulus efficiency η_a

The calculations are performed within two loops as indicated in the psuedo-code of Table B1. In the outer loop, the hub-tip ratio is varied over the specified range and the corresponding values of axial velocity, tip flow factor, and hub radius are determined. For each hub-tip ratio, the inner loop varies the swirl factor over the specified range, from which the efficiency, pressure rise and swirl velocity are calculated.

The calculations start by determining the axial through flow velocity for a given hub-tip ratio, ie

$$c_x = \frac{Q}{\pi r_t^2 (1 - x_b^2)} \qquad \text{B 37}$$

The flow factor and hub radius are then calculated by means of the expressions

$$\phi_t = \frac{c_x}{\Omega r_t} \qquad \text{B 38}$$

$$r_h = r_t x_b \qquad \text{B 39}$$

Thereafter, for the specified range of swirl factor, the total to total and total to static efficiencies, swirl velocity, dynamic pressure and static pressure are calculated :

$$(1 - \eta_{tt})_{avg} = \frac{2}{3} \frac{(\tan \gamma)_{avg}}{\phi_t} \frac{(1 - x_b^3)}{(1 - x_b^2)} + \frac{2(\tan \gamma)_{avg}[\phi_t - \epsilon_h x_b]}{(1 + x_b)} + (1 - \eta_a) \frac{\phi_t}{2\epsilon_h x_b} \qquad \text{B 40}$$

$$(1 - \eta_{ts})_{avg} = \frac{2}{3} \frac{(\tan \gamma)_{avg}}{\phi_t} \frac{(1 - x_b^3)}{(1 - x_b^2)} + \frac{2(\tan \gamma)_{avg}[\phi_t - \epsilon_h x_b]}{(1 + x_b)} \qquad \text{B 41}$$

$$+ (1 - \eta_a) \frac{\phi_t}{2\epsilon_h x_b} + \frac{\phi_t}{2\epsilon_h x_b} \left[1 - 2(\epsilon_h x_b)^2 \cdot \frac{\ln(x_b)}{(1 - x_b^2)} \right]$$

B.11

$$c_\theta(r_h) = \epsilon_h c_x \qquad\qquad\qquad\text{B 42}$$

$$\Delta p_{o_{th}} = \rho\,\Omega\,r_h c_\theta(r_h) \qquad\qquad\qquad\text{B 43}$$

$$(p_d)_{avg} = \frac{1}{2}\rho c_x^2\left[1 - 2(\epsilon_h x_b)^2\cdot\frac{\ln(x_b)}{(1-x_b^2)}\right] \qquad\qquad\text{B 44}$$

$$\Delta p_{ts} = \eta_{ts}\Delta p_{o_{th}} \qquad\qquad\qquad\text{B 45}$$

1.3 Sample Calculations

Table B2 lists a typical set of input data and is used here to illustrate the sequence of calculations performed by FANOPT. The calculations are performed for a single data point, namely a hub-tip ratio of 0.4 and a swirl factor of 1.1. The FANOPT output file (Table B3), as used to generate the design point performance map depicted in Figure 4.6, is included for reference.

$$c_x = \frac{Q}{\pi r_t^2(1-x_b^2)}$$

$$= \frac{16}{\pi(0.771)^2(1-(0.4)^2)}$$

$$= 10.2\ m/s$$

$$\phi_t = \frac{c_x}{\Omega r_t}$$

$$= \frac{10.2}{78.54\ \times\ 0.771}$$

$$= 0.168$$

$$r_h = r_t x_b$$

$$= 0.771 \times 0.4$$

$$= 0.308 \ m$$

$$(1-\eta_{tt})_{avg} = \frac{2}{3}\frac{(\tan\gamma)_{avg}}{\phi_t}\frac{(1-x_b^3)}{(1-x_b^2)} + \frac{2(\tan\gamma)_{avg}[\phi_t - \epsilon_h x_b]}{(1+x_b)} + (1-\eta_a)\frac{\phi_t}{2\epsilon_h x_b}$$

$$= \frac{2}{3}\times\frac{(0.0167)}{(0.168)}\times\frac{(1-(0.4)^3)}{(1-(0.4)^2)} + \frac{2\times0.0167\times(0.168-1.1\times0.4)}{(1+0.4)} + \frac{(1-0.8)\times0.168}{(2\times1.1\times0.4)}$$

$$= 0.074 - 0.006 + 0.038$$

$$= 0.106$$

Thus $\eta_{tt} = (1-0.106) \times 100\%$

$$= 89.38\%$$

$$(1-\eta_{ts})_{avg} = \frac{2}{3}\frac{(\tan\gamma)_{avg}}{\phi_t}\frac{(1-x_b^3)}{(1-x_b^2)} + \frac{2(\tan\gamma)_{avg}[\phi_t - \epsilon_h x_b]}{(1+x_b)}$$

$$+ (1-\eta_a)\frac{\phi_t}{2\epsilon_h x_b} + \frac{\phi_t}{2\epsilon_h x_b}\left[1 - 2(\epsilon_h x_b)^2.\frac{\ln(x_b)}{(1-x_b^2)}\right]$$

$$= \frac{2}{3}\times\frac{(0.0167)}{(0.168)}\times\frac{(1-(0.4)^3)}{(1-(0.4)^2)} + \frac{2\times0.0167\times(0.168-1.1\times0.4)}{(1+0.4)}$$

$$+ \frac{(1-0.8)\times0.168}{(2\times1.1\times0.4)} + \frac{1}{2}\times\left(\frac{0.168}{1.1\times0.4}\right)\times\left(1-2\times(1.1\times0.4)^2\frac{\ln(0.4)}{(1-(0.4))^2}\right)$$

$$= 0.074 - 0.006 + 0.038 + 0.272$$

$$= 0.378$$

Thus $\eta_{ts} = (1-0.378)\times100\%$

$$= 62.246\%$$

$$c_\theta(r_h) = \epsilon_h c_x$$

$$= 1.1 \times 10.2$$

$$= 11.2 \ m/s^2$$

$$\Delta p_{o_{th}} = \rho \Omega r_h c_\theta(r_h)$$

$$= 1.2 \times 78.54 \times 0.308 \times 11.2$$

$$= 325.118 \ Pa$$

$$(p_d)_{avg} = \frac{1}{2}\rho c_x^2 \left[1 - 2(\epsilon_h x_b)^2 \cdot \frac{\ln(x_b)}{(1-x_b^2)} \right]$$

$$= \frac{1}{2} \times 1.2 \times (10.2)^2 \times \left(1 - 2 \times (1.1 \times 0.4)^2 \frac{\ln(0.4)}{(1-(0.4))^2} \right)$$

$$= 88.79 \ Pa$$

$$\Delta p_{ts} = \Delta p_{o_{th}} \eta_{ts}$$

$$= 325.118 \times 0.62246$$

$$= 202.37 \ Pa$$

$$\Delta p_o = \Delta p_{o_{th}} \eta_{tt}$$

$$= 325.118 \times 0.8938$$

$$= 290.59 \ Pa$$

```
for x_b  =  x_b(1)  to  x_b(n) do

    Calculate c_x

    Calculate φ_t

    Calculate Γ_h


    for ε_h  =  ε_h(1)  1  to ε_h(m)   do

        Calculate c_θ

        Calculate η_tt

        Calculate η_ts

        Calculate Δp_{0_{th}}

        Calculate c_θ

        Calculate (p_d)_{avg}

        Calculate Δp_{ts}
    enddo

enddo
```

Table B1 Psuedo-code, FANOPT calculation loops

Number of hub-tip ratios to evaluate	5
Range of hub-tip ratios	0.2...0.6
Number of swirl factors to evaluate	19
Range of swirl factors	0.3...1.2
Volumetric flow rate (m^3/s)	16.0
Tip radius (m)	0.771
Rotational speed (rad/s)	78.54
Density (kg/m^3)	1.2
Drag/lift ratio $((\tan\gamma)_{avg})$	0.0167
Annulus efficiency (η_a)	0.8

Table B2 FANOPT input data

Table B3 FANOPT output file

F A N O P T - Fan Optimisation - Version 1.0

INPUT DATA
----

tip radius	(m)	0.771
Cd/Cl	(.)	0.017
annulus efficiency	(.)	0.800
flow rate	(m^3/s)	16.000
density	(kg/m^3)	1.200
rotational speed	(RPM)	750.002

number of hub-tip ratios	5
hub-tip ratio range	0.20 .. 0.60
number of swirl factors	19
swirl factor range	0.30 .. 1.20

XB	=	0.200
Cx	=	8.925
Phi(t)	=	0.147
rh	=	0.154

Ps	Eff(ts)	Eff(tt)	Eps(h)	C(theta)	Po(th)	Pd(avg)
-22.145	-56.914	67.387	0.300	2.677	38.911	48.366
-16.378	-36.078	70.924	0.350	3.124	45.396	48.575
-10.639	-20.507	73.584	0.400	3.570	51.881	48.815
-4.928	-8.444	75.659	0.450	4.016	58.366	49.087
0.754	1.162	77.324	0.500	4.462	64.851	49.392
6.407	8.982	78.692	0.550	4.909	71.336	49.728
12.033	15.462	79.836	0.600	5.355	77.821	50.097
17.629	20.911	80.809	0.650	5.801	84.306	50.497
23.198	25.551	81.646	0.700	6.247	90.791	50.930
28.738	29.542	82.376	0.750	6.693	97.276	51.395
34.249	33.008	83.018	0.800	7.140	103.762	51.891
39.732	36.039	83.588	0.850	7.586	110.247	52.420
45.187	38.710	84.097	0.900	8.032	116.732	52.981
50.613	41.076	84.556	0.950	8.478	123.217	53.574
56.011	43.184	84.971	1.000	8.925	129.702	54.199
61.380	45.070	85.350	1.050	9.371	136.187	54.856
66.721	46.765	85.697	1.100	9.817	142.672	55.545
72.033	48.294	86.016	1.150	10.263	149.157	56.266
77.317	49.676	86.311	1.200	10.710	155.642	57.019

```
XB       =  0.300
Cx       =  9.415
Phi(t)   =  0.155
rh       =  0.231
```

Ps	Eff(ts)	Eff(tt)	Eps(h)	C(theta)	Po(th)	Pd(avg)
-8.207	-13.329	74.900	0.300	2.824	61.573	54.325
0.868	1.208	77.406	0.350	3.295	71.835	54.737
9.888	12.044	79.296	0.400	3.766	82.097	55.212
18.852	20.412	80.774	0.450	4.237	92.359	55.750
27.761	27.052	81.964	0.500	4.707	102.621	56.352
36.615	32.436	82.945	0.550	5.178	112.883	57.017
45.413	36.877	83.769	0.600	5.649	123.146	57.745
54.155	40.594	84.472	0.650	6.120	133.408	58.537
62.843	43.741	85.080	0.700	6.590	143.670	59.392
71.474	46.432	85.612	0.750	7.061	153.932	60.310
80.051	48.754	86.082	0.800	7.532	164.194	61.291
88.572	50.770	86.502	0.850	8.003	174.456	62.336
97.038	52.533	86.879	0.900	8.473	184.718	63.445
105.448	54.081	87.221	0.950	8.944	194.981	64.616
113.802	55.448	87.532	1.000	9.415	205.243	65.851
122.102	56.658	87.818	1.050	9.886	215.505	67.149
130.346	57.735	88.081	1.100	10.356	225.767	68.511
138.534	58.694	88.324	1.150	10.827	236.029	69.936
146.667	59.550	88.550	1.200	11.298	246.291	71.424

```
XB       =  0.400
Cx       =  10.200
Phi(t)   =  0.168
rh       =  0.308
```

Ps	Eff(ts)	Eff(tt)	Eps(h)	C(theta)	Po(th)	Pd(avg)
5.422	6.096	78.483	0.300	3.060	88.939	64.380
18.477	17.808	80.536	0.350	3.570	103.762	65.088
31.438	26.511	82.087	0.400	4.080	118.585	65.905
44.304	33.210	83.305	0.450	4.590	133.408	66.831
57.075	38.504	84.288	0.500	5.100	148.231	67.866
69.752	42.778	85.102	0.550	5.610	163.054	69.010
82.333	46.287	85.787	0.600	6.120	177.877	70.263
94.820	49.206	86.375	0.650	6.630	192.700	71.624
107.212	51.663	86.885	0.700	7.140	207.523	73.095
119.510	53.749	87.334	0.750	7.650	222.346	74.675
131.712	55.535	87.733	0.800	8.160	237.169	76.363
143.820	57.073	88.090	0.850	8.670	251.992	78.161
155.833	58.405	88.413	0.900	9.180	266.816	80.067
167.751	59.562	88.707	0.950	9.690	281.639	82.083
179.574	60.572	88.976	1.000	10.200	296.462	84.207

B.18

191.302	61.456	89.225	1.050	10.710	311.285	86.440
202.936	62.230	89.455	1.100	11.220	326.108	88.782
214.475	62.909	89.669	1.150	11.730	340.931	91.234
225.919	63.504	89.869	1.200	12.239	355.754	93.794

```
XB     =  0.500
Cx     = 11.424
Phi(t) =  0.189
rh     =  0.386
```

Ps	Eff(ts)	Eff(tt)	Eps(h)	C(theta)	Po(th)	Pd(avg)
18.620	14.954	80.452	0.300	3.427	124.514	81.554
36.830	25.354	82.304	0.350	3.998	145.266	82.730
54.883	33.058	83.708	0.400	4.569	166.019	84.087
72.778	38.966	84.811	0.450	5.141	186.771	85.625
90.515	43.617	85.705	0.500	5.712	207.523	87.343
108.095	47.353	86.447	0.550	6.283	228.275	89.243
125.516	50.402	87.074	0.600	6.854	249.028	91.323
142.780	52.925	87.614	0.650	7.425	269.780	93.585
159.886	55.032	88.084	0.700	7.996	290.532	96.027
176.834	56.808	88.499	0.750	8.568	311.285	98.650
193.624	58.314	88.869	0.800	9.139	332.037	101.454
210.257	59.598	89.202	0.850	9.710	352.789	104.439
226.732	60.698	89.505	0.900	10.281	373.542	107.605
243.049	61.641	89.781	0.950	10.852	394.294	110.952
259.208	62.453	90.035	1.000	11.424	415.046	114.480
275.209	63.151	90.270	1.050	11.995	435.799	118.188
291.053	63.750	90.489	1.100	12.566	456.551	122.078
306.738	64.265	90.694	1.150	13.137	477.303	126.148
322.266	64.705	90.887	1.200	13.708	498.056	130.399

```
XB     =  0.600
Cx     = 13.387
Phi(t) =  0.221
rh     =  0.463
```

Ps	Eff(ts)	Eff(tt)	Eps(h)	C(theta)	Po(th)	Pd(avg)
29.553	16.878	81.463	0.300	4.016	175.098	113.087
55.030	26.938	83.280	0.350	4.685	204.281	115.096
80.235	34.367	84.659	0.400	5.355	233.464	117.413
105.167	40.041	85.745	0.450	6.024	262.647	120.039
129.827	44.487	86.627	0.500	6.693	291.829	122.974
154.215	48.040	87.359	0.550	7.363	321.012	126.218
178.330	50.923	87.980	0.600	8.032	350.195	129.772
202.173	53.291	88.515	0.650	8.702	379.378	133.634
225.743	55.253	88.982	0.700	9.371	408.561	137.805
249.041	56.892	89.396	0.750	10.040	437.744	142.285

B.19

272.067	58.267	89.766	0.800	10.710	466.927	147.074
294.820	59.426	90.099	0.850	11.379	496.110	152.172
317.301	60.404	90.403	0.900	12.048	525.293	157.578
339.509	61.231	90.681	0.950	12.718	554.476	163.294
361.445	61.927	90.937	1.000	13.387	583.659	169.319
383.108	62.513	91.175	1.050	14.056	612.842	175.653
404.499	63.004	91.398	1.100	14.726	642.025	182.296
425.618	63.411	91.606	1.150	15.395	671.208	189.247
446.464	63.745	91.802	1.200	16.064	700.391	196.508
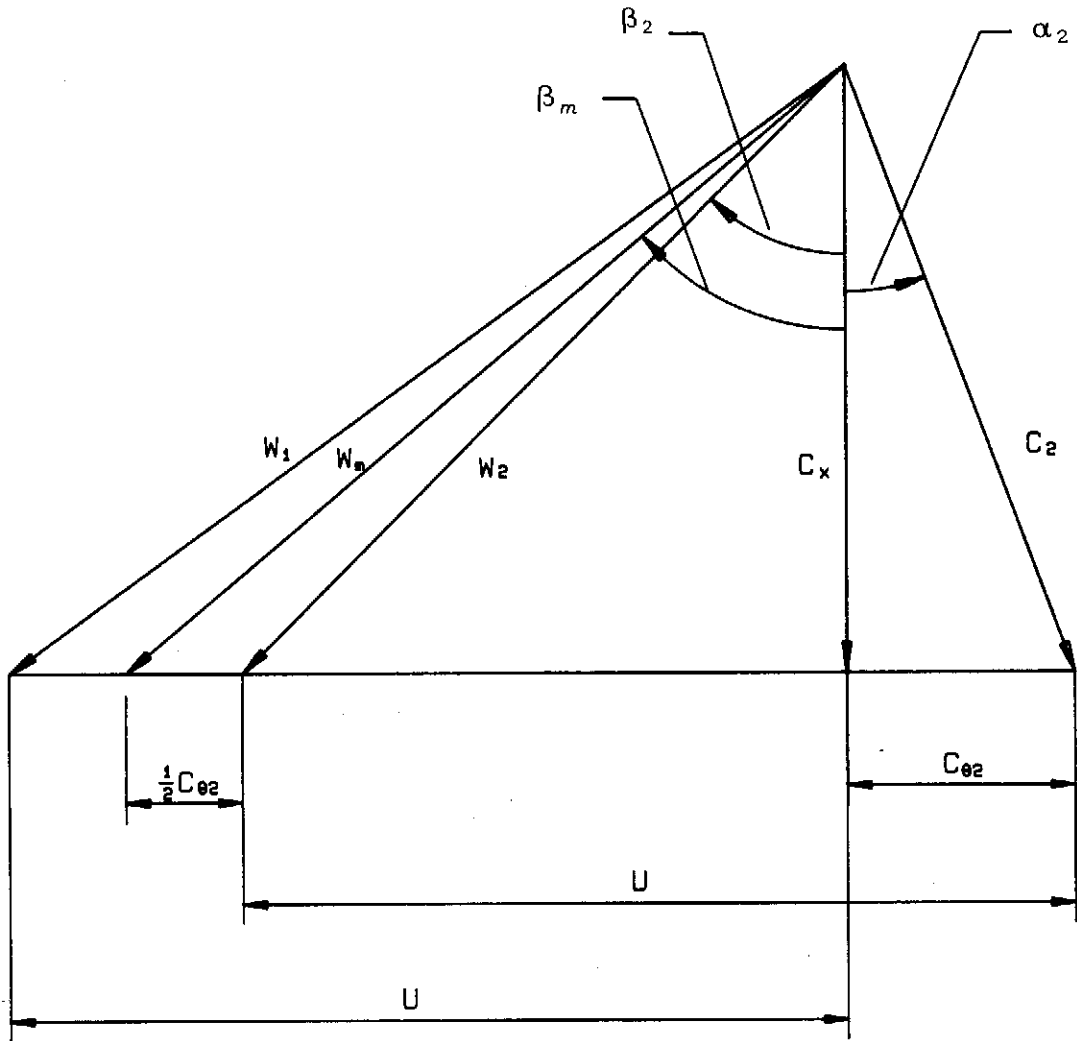
Figure B1   Free vortex velocity triangle

APPENDIX C FAN BLADE DESIGN

The radial equilibrium analysis assumes that whatever the geometry of the fan blading, it will induce the required changes in swirl velocity to effect the assumed pressure rise. However, due to the viscosity of real fluids and the consequent development of boundary layers over the wetted surfaces, the shape and nature of the fan blading will have an important influence on the actual flow turning realised and the losses in so doing. It is therefore necessary to have available relationships between the desired flow parameters and the geometry of the blading, as well as a means to assess the efficiency penalty associated with a particular geometry. Conventional practice, as manifested in the work of Van Niekerk (1958), Patterson (1944) and Wallis (1983) is to treat the fan blading as being made up of a number of separate two dimensional aerofoils and utilise the analytically derived expressions for lift and drag coefficient in conjunction with the experimentally measured lift/drag characteristics for aerofoil sections.

1.1 Lift and Drag Coefficients

For free-vortex or swirl distributions not far removed from the free-vortex, streamline shift will be non-existent or at least very small. In the free-vortex case, the axial velocity component is constant through the fan but will vary for the non free-vortex distributions. For the analysis that follows, a mean axial velocity is defined

$$c_{x_m} = \frac{1}{2}(c_{x_1} + c_{x_2}) \qquad \text{C 1}$$

and a mean relative velocity

$$w_m = \frac{c_{x_m}}{\cos\beta_m}$$

where the mean relative angle β_m is defined

$$\tan\beta_m = \frac{1}{2}(\tan\beta_1 + \tan\beta_2)$$

1.1.1 Lift Coefficient

If one now considers the forces exerted by the blade on the fluid, the force triangle (Figure C.2) is obtained. The vectors denoted by L and D are the lift and drag forces, respectively assigned perpendicular and parallel to the mean relative velocity w_m. The vectors X and Y are the axial and tangential components of total force (vector sum of L and D) exerted by the blade on the fluid respectively. From the geometry of the vector diagram

$$X = L\sin\beta_m - D\cos\beta_m$$

$$Y = L\cos\beta_m + D\sin\beta_m$$

Considering the x-direction force per unit span, Equation C4 may be written

$$dX = L\left(\sin\beta_m - \frac{D}{L}\cos\beta_m\right).dr$$

The lift coefficient is defined as

$$C_L = \frac{L}{\frac{1}{2}\rho\, w_m^2 c}$$

and the angle γ as

$$\tan\gamma = \frac{D}{L} = \frac{C_D}{C_L} \qquad\qquad \text{C 8}$$

and upon substitution into the expression for dX (Equation C6) yields

$$dX = \frac{\rho c c_{x_m}^2 C_L}{2\cos^2\beta_m}(\sin\beta_m - \tan\gamma\cos\beta_m).dr \qquad\qquad \text{C 9}$$

The term in brackets simplifies to

$$(\sin\beta_m - \tan\gamma\cos\beta_m) = \frac{\sin(\beta_m - \gamma)}{\cos\gamma} \qquad\qquad \text{C 10}$$

and thus

$$dX = \frac{\frac{1}{2}\rho c_{x_m}^2 C_L c}{\cos^2\beta_m} \cdot \frac{\sin(\beta_m - \gamma)}{\cos\gamma}.dr \qquad\qquad \text{C 11}$$

The torque exerted by one blade element at radius 'r' is dY.r and if there are n_b blades then the torque is n_b dY.r. Substituting the expressions for the lift and drag coefficients into Equation C11 and simplifying results in

$$dY = \frac{\frac{1}{2}\rho c_{x_m}^2 C_L c}{\cos^2\beta_m} \cdot \frac{\cos(\beta_m - \gamma)}{\cos\gamma}.dr \qquad\qquad \text{C 12}$$

The torque at a given radius is therefore

$$dT = \frac{\frac{1}{2}n_b\rho c_{x_m}^2 C_L c}{\cos^2\beta_m} \cdot \frac{\cos(\beta_m - \gamma)}{\cos\gamma}.r.dr \qquad\qquad \text{C 13}$$

For a blade element where the fluid is assumed to enter and exit at the same radius, the torque may also be written

$$dT = r(c_{\theta_2} - c_{\theta_1}).d\dot{m}$$ C 14

where the elementary mass flow rate $d\dot{m}$ is given by

$$d\dot{m} = 2\pi\rho c_{x_m} r.dr$$ C 15

For an axial flow fan with no guide vanes, the inlet flow is assumed to be purely axial with a zero swirl component, thus

$$dT = 2\pi\rho c_{x_m} c_{\theta_2} r.dr$$ C 16

Equating expressions C13 and C16 reveals that

$$C_L = \frac{4\pi c_{\theta_2} r \cos^2\beta_m \cos\gamma}{c n_b c_{x_m} \cos(\beta_m - \gamma)}$$ C 17

At a given radius the pitch 's' is given by the expression

$$s = \frac{2\pi r}{n_b}$$ C 18

which on substitution into Equation C17 gives

$$C_L \sigma = 2\left(\frac{c_{\theta_2}}{c_{x_m}}\right)\frac{\cos^2\beta_m \cos\gamma}{\cos(\beta_m - \gamma)}$$ C 19

C.4

where σ is the solidity and is defined as the ratio of the blade chord to pitch, ie $\sigma = c/s$. Except for very small lift coefficients, the drag/lift ratio will be small and so therefore, γ will be a small angle. Thus, $\cos\gamma \approx 1$ and

$$\cos(\beta_m - \gamma) \approx \cos\beta_m \qquad \qquad \text{C 20}$$

In the design phase before the details of the blade profile has been established, the expression for the lift coefficient may be approximated by

$$C_L \sigma = 2\left(\frac{c_{\theta_2}}{c_{x_m}}\right)\cos\beta_m \qquad \qquad \text{C 21}$$

1.1.2 Drag Coefficient

The drag coefficient, defined as

$$C_D = \frac{D}{\frac{1}{2}\rho w_m^2 c} \qquad \qquad \text{C 22}$$

is an expression of the energy losses (total pressure) incurred by a fluid as it passes over a two dimensional aerofoil, this loss in total pressure being due to skin friction and related effects. It is easily shown (Dixon (1978)) that the relationship between total pressure loss and the force vectors X and Y is given by

$$\frac{\Delta p_{o_{loss}}}{\rho} = \frac{1}{\rho s}(-X + Y\tan\beta_m) \qquad \qquad \text{C 23}$$

Furthermore, the geometry of the vector diagram indicates that the drag force, D can be expressed

$$D = \cos\beta_m(-X + Y\tan\beta_m)$$ C 24

which on combining with Equation C23 yields

$$D = s\cos\beta_m\Delta p_{o_{loss}}$$ C 25

The drag coefficient may therefore be written

$$C_D = \frac{s\cos\beta_m\Delta p_{o_{loss}}}{\frac{1}{2}\rho w_m^2 c}$$ C 26

In the cascade testing of compressor blade profiles, an often used total pressure loss coefficient defined by

$$\zeta = \frac{\Delta p_{o_{loss}}}{\frac{1}{2}\rho w_m^2}$$ C 27

reflects the measured loss in total pressure. Incorporating ζ into the drag coefficient relationship finally yields the most useful form of expression for design purposes :

$$C_D = \zeta\left(\frac{s}{c}\right)\cos^3\beta_m$$ C 28

1.1.3 Losses and Efficiency

The total pressure loss occurring within turbomachinery blading is usually expressed as the sum of three components, namely; profile losses, secondary flow losses and tip clearance losses.

Profile losses include all those losses in total pressure arising from skin friction and flow separation, and as such, are dominated by the growth and development of the boundary layer over blade surfaces. Consequently, profile losses are dependent on those factors which influence boundary layer growth, primarily surface roughness, Reynolds number and blade surface pressure gradient. Profile losses are essentially a two dimensional phenomenon and are adequately characterised by the measured drag coefficient for a given profile section.

Secondary losses are manifested by streamwise vortex structures and are caused by the turning of the hub and tip endwall boundary layers, as well as spanwise variations in circulation. Although numerous investigators have attempted analytical calculations of secondary flows in turbomachinery, the inherent complexity of these flows precludes the development of a usable theoretical procedure for loss estimation. In practice, empirical relationships are used to express secondary losses in terms of known major design parameters.

Tip clearance losses are indicated by a streamwise vorticity component in the tip region and are caused by the difference in pressure between the pressure and suction sides of the blade tips, as well as the relative motion between the blade tip and the outer shrouding. As with secondary flows, the analysis of tip clearance flows is not practical and empirically derived expressions in terms of drag coefficient augmentation or an overall efficiency penalty are utilised.

The procedure for the calculation of the pressure losses described below, closely follows the recommendations of Wallis (1983) who uses the experimental results obtained from compressor cascade tests. Wallis notes that the

experimental data always relates strictly to the specific geometry and test conditions for which it was measured, therefore these data can only be applied to industrial type fans with great caution. The justification for using such data rests on the fact that since there is little data that applies specifically to fan equipment, the fan designer has little option but to rely on compressor data. Furthermore, in those cases where the blade root solidities and stagger angles are similar to those encountered in compressors, the compressor data will be applicable.

1.1.3.1 Overall Total Pressure Loss Coefficient

Current practice for combining losses arising from profile and secondary flow components is to express the losses in terms of midspan design conditions, although this does not imply that losses are evenly distributed across the blade span. Nonetheless, Wallis (1983) states that for the same mean flow conditions, the suggested procedure will result in close agreement between the estimated and actual mean total pressure rise, provided tip clearances remain small.

The drag coefficient for a blade element is related to the total pressure loss by Equation C28. Multiplying through by C_L / K_{th} and rearranging gives

$$\frac{C_L \sigma}{K_{th}} = \zeta \frac{\cos^3 \beta_m}{K_{th}} \frac{C_L}{C_D} \qquad\qquad \text{C 29}$$

The Euler work equation gives

$$\frac{\Delta p_o}{\rho} = U c_{\theta_2} \qquad\qquad \text{C 30}$$

and non-dimensionalising by $\frac{1}{2}\rho c_{x_2}^2$ provides

$$K_{th} = \frac{\Delta P_o}{\frac{1}{2}\rho c_{x_2}} = 2\left(\frac{U}{c_x}\right)\left(\frac{c_{\theta_2}}{c_{x_2}}\right) = \frac{2}{\phi}\left(\frac{c_{\theta_2}}{c_{x_2}}\right) \qquad \text{C 31}$$

From the expression for the loading factor $C_L \sigma$ (Equation C21) and Equation C31 obtain :

$$\frac{C_L \sigma}{K_{th}} = \phi \cos \beta_m \qquad \text{C 32}$$

Substitution into Equation C29 and solving for ζ yields the relationship for the total pressure loss coefficient in terms of the design parameters, ie

$$\zeta = \left(\frac{C_D \phi}{C_L \cos^2 \beta_m}\right) K_{th} \qquad \text{C 33}$$

Two assumptions are now made :

    i.   The total pressure loss for the entire rotor can be expressed in terms of Equation C33 by evaluating all the component parameters at the mid-span (mean) station, ie

$$\zeta_R = \left(\frac{C_D \phi}{C_L \cos^2 \beta_m}\right)_{mean} K_{th} \qquad \text{C 34}$$

    ii.   The drag coefficient for the overall total pressure loss coefficient above (Equation C34) is the sum of the profile and secondary drag effects

$$C_D = C_{D_P} + C_{D_S}$$

where C_{D_P} is simply the blade section drag coefficient evaluated at the mean line station conditions and C_{D_S} the corresponding secondary drag coefficient as described below.

1.1.3.2 The Secondary Drag Coefficient

For any given blade profile section, lift and drag coefficient data are usually presented as a function of the flow angle of attack. However, because secondary drag is dependent on the many geometric and aerodynamic factors specific to a particular machine, it is not easily estimated. For design purposes, Wallis (1983) advocates the Howell expression

$$C_{D_S} = b C_L^2$$

C 36

where the recommended value of the coefficient b is 0.018 for general use, reducing to 0.015 for cases of high operational Reynolds number. He also indicates that provided the blade aspect ratio is greater than 1.5, these values should produce efficiency predictions within 2%. When the aspect ratio of the order 0.7, an additional loss of about 2% is likely and the characteristic curve near stall will be more rounded because of the influence of larger secondary flows.

1.1.3.3 Efficiency Estimation

Using the loss coefficient ζ_R, an estimate of the total to total and total to static efficiency may be made. The total to static efficiency is defined as

$$\eta_{ts} = 1 - \left(\frac{\Delta p_{o_{loss}} + \frac{1}{2}\rho c_2^2}{\Delta p_{o_{th}}} \right) \qquad \text{C 37}$$

Non-dimensionalising by dividing the bracketed numerator and denominator by $\frac{1}{2}\rho c_{xm}^2$ yields

$$\eta_{ts} = 1 - \left[\frac{\Delta p_{o_{loss}}}{\frac{1}{2}\rho c_{xm}^2} + \left(\frac{c_2}{c_{xm}} \right)^2 \right] / K_{th,m} \qquad \text{C 38}$$

From the definition of the total pressure loss coefficient, have that

$$\Delta p_{o_{loss}} = \zeta_R \frac{1}{2}\rho w_m^2 \qquad \text{C 39}$$

and therefore

$$\frac{\Delta p_{o_{loss}}}{\frac{1}{2}\rho c_{xm}^2} = \zeta_R \left(\frac{w_m}{c_{x_m}} \right)^2 \qquad \text{C 40}$$

Inserting this expression into Equation C38 gives

$$\eta_{ts} = 1 - \left[\zeta_R \left(\frac{w_m}{c_{xm}} \right)^2 + \left(\frac{c_2}{c_{xm}} \right)^2 \right] / K_{th,m} \qquad \text{C 41}$$

1.1.3.4 Tip Clearances

According to Wallis (1983), if the tip clearance does not exceed 1% of the blade span, no adjustments to the efficiency or pressure rise are necessary. For tip clearances greater than 1%, the following efficiency penalty is suggested :

$$\Delta\eta = 2\left(\frac{t_c}{h} - 0.01\right)$$
<div align="right">C 42</div>

With regard to the effects of tip clearance on total pressure rise, Wallis recommends the use of the experimentally derived curve due to Ruden (1944), which relates the additional losses in total pressure to the tip clearance/blade-span ratio, as illustrated in Figure C3. A least squares quadratic curve fit to this data provides an analytical formulation that facilitates usage in the design phase, ie

$$\zeta_t = -0.0125759 + 0.865714\left(\frac{t_c}{h}\right) + 83.98941\left(\frac{t_c}{h}\right)^2$$
<div align="right">C 43</div>

1.1.4 Blade Camber, Incidence and Flow Deflection

From Figure C4, the relationship between the blade camber angle and the remaining geometric parameters is easily deduced, ie

$$\theta = (\beta_1 - \beta_2) + (\delta - i)$$
<div align="right">C 44</div>

Although the incidence angle, i, has been shown to have an optimum value, Wallis states that this does not vary significantly from zero. The deviation angle, however, is dependent on the growth of the boundary layer over the blade surface and is difficult to determine accurately. Since it

is not necessary to specify camber with great accuracy, approximate estimates of deviation are acceptable in practice.

With regard to local incidence angle, Wallis recommends the use of zero incidence for preliminary design work although small amounts of negative incidence can improve efficiency in the case of low solidity (isolated aerofoil) blading.

Wallis states that in most design cases, an accurate estimate of exit flow deviation is not necessary because for high solidity blading, or in the hub region of low solidity blading, the cascade influence is accounted for by means of an "interference factor" technique. Isolated aerofoil data represent the loss of lift due to boundary layer growth as a reduction in the slope of the lift coefficient/incidence curve. Since increasing the solidity alters both the lift curve slope and the no-lift angle of a section, a useful interference factor must include the influence of both these variables. If experimental data is to be used, it must be applicable to the actual profiles use, ie it must pertain to those specific profiles or family of profiles operating under conditions similar to those of the experiment.

The following empirical relationship due to Carter (1950) is suggested for the determination of the deviation angle

$$\delta = m\theta \sqrt{\frac{s}{c}}$$

C 45

where m is a function of the blade stagger angle and is presented in Figure C5. This curve is in fact a modification of the original Carter data by Wallis, who extended the

stagger angle range to give deviation data applicable to isolated aerofoils. A third order polynomial curve-fit to the data provides ready access for design work, ie

$$m = 0.209253 + \frac{0.2322389}{10^2}\xi - \frac{0.3736909}{10^4}\xi^2 + \frac{0.8668135}{10^6}\xi^3 \qquad \text{C 46}$$

where ξ is given in degrees.

According to Wallis, blade camber variations along the blade span are almost always necessary for fans where the required flow deflection varies significantly from hub to tip, although in those cases where the overall flow turning angle is small, constant camber blading can provide satisfactory results.

It is suggested that the final choice of camber will depend on an assessment of stiffness, blade erosion, fan efficiency and power considerations and the selected value of the design lift coefficient. Increasing camber will generally result in higher design lift coefficient providing the loading factor limit is not exceeded. Wallis recommends a minimum camber angle of 14° and a small amount of negative incidence when $(\beta_1 - \beta_2)$ is minimal.

1.1.5 Blade Loading Factor Limits

The blade loading factor $C_L\sigma$ is a function of the flow turning angle, swirl velocity and axial through flow velocity, obtained via the equation

$$C_L\sigma = 2\left(\frac{c_{\theta_2}}{c_{x_m}}\right)\cos\beta_m \qquad \text{C 47}$$

Whilst the variables on the right hand side of the equation will be specified as part of the radial equilibrium analysis and fan duty requirements, either of C_l or σ must be specified by the designer. Wallis describes a number of methods and recommendations for the selection of these two parameters.

In the case of high solidity blading (and therefore loading factor), the value of lift coefficient is selected on the basis of stall properties rather than lift drag ratios obtained from isolated aerofoil tests. According to Wallis, the factors influencing the choice of lift coefficient are the flow turning angle, solidity, aspect ratio, tip clearance, stagger angle and inlet flow quality, since all these parameters have an effect on the initiation of stall. The fan designer is therefore forced to be conservative and select values of lift coefficient with a generous stall margin. The recommended lift coefficient range in general design practice lies within the domain 0.6 to 1.0 and the Keller (1937) design rules advise loading factors and solidities not exceeding 1.0 and 1.1 respectively. However, Wallis comments that a more definitive method for the determination of these variables is required and describes a variety of semi-empirical approaches culled from compressor design practice.

1.1.5.1 Low Solidity Blading

Single stage, low pressure rise fans are invariably of low solidity. For this type of blading, the maximum lift/drag ratio and the minimum lift coefficient increase with camber angle. However, when secondary effects are included in the drag/lift ratio, the lift coefficient corresponding to the maximum lift/drag ratio is reduced. Wallis therefore recommends the use of flat undersurface blading such as

Clark-Y or RAF-6 profiles because high camber angles are not required to achieve lift coefficients of the order 1.0. Also suggested are conservative design lift coefficients which lead to lower powers and noise levels, a wide efficiency operating envelope and a safe stall margin. Furthermore, small errors in the design of the associated ducting or duct resistance fluctuations are of lesser importance when a conservative value for lift coefficient is selected. Reduced design lift coefficients must also be used in cases of blade surface roughness, imperfections and poor quality inlet flow.

1.1.5.2 High Solidity Blading

Loading factor is of great importance in high solidity blading and a number of methods in the literature, namely Lieblein (1965) Carter (1955), Zweifel (1945), relate the flow turning angle to blading parameters such as solidity, nominal lift coefficient and stagger angle. Wallis' (1964) design method is based on the Howell correlation

$$C_L^* = 2\left(\frac{\cos\beta_1}{\cos\beta_2}\right)^{2.75} \qquad\qquad \text{C 48}$$

where C_L^* is a nominal design lift coefficient. Combining the Howell relationship with the blade loading expression (Equation C21), the Howell expression can be rewritten

$$\sigma^* = \epsilon\cos\beta_m\left(\frac{\cos\beta_2}{\cos\beta_1}\right)^{-2.75} \qquad\qquad \text{C 49}$$

and the relative flow angles may be reposed

$$\beta_1 = \tan^{-1}(\phi) \qquad\qquad \text{C 50}$$

$$\beta_2 = \tan^{-1}\left(\frac{\phi}{1+\epsilon\phi}\right) \qquad\qquad \text{C 51}$$

$$\beta_m = \tan^{-1}\left(\frac{\phi(2+\epsilon\phi)}{2(1+\epsilon\phi)}\right)$$

Wallis states that all the blade loading recommendations will provide conservative values of lift coefficient or solidity when used in fan design.

A limited trade-off between solidity and lift coefficient can be made. Because of multi-plane interference effects, increasing the solidity up to a value of about 2 gives some gains in load factor. Thus for fans of high loading, a non-linear increase in blade chord in the root region is experienced for free-vortex designs and can lead to impractical blade planforms.

Blade root chord reductions can be made if it is considered that the problem is extremely local in nature. Small local increases in both general and nose camber will increase the maximum lift coefficient attainable and hence delay the local flow separation that might arise from chord reductions. This will also reduce secondary drag.

At spanwise stations just outside the root region, any trade-off between solidity and lift coefficient is strongly advised if reductions in solidity are required (or desired).
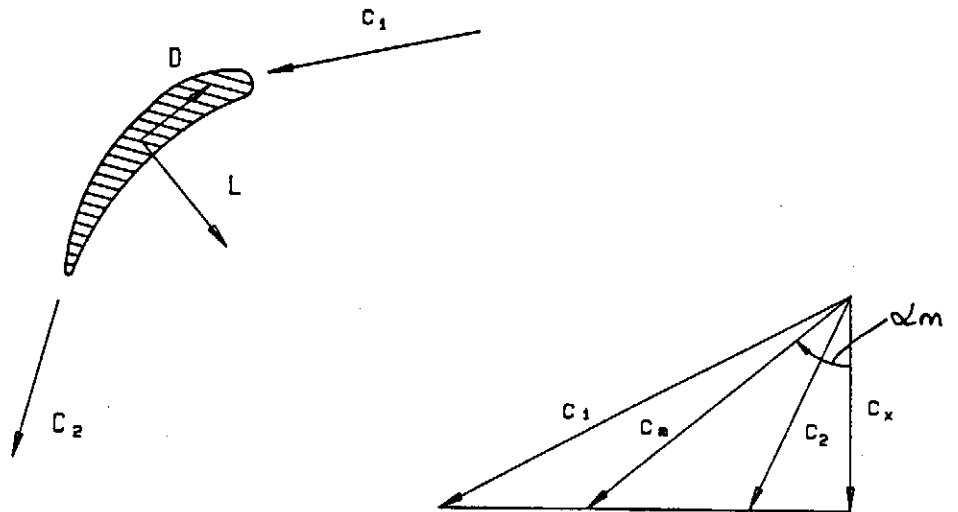
Figure C1 Lift and drag forces exerted by a cascade on the fluid
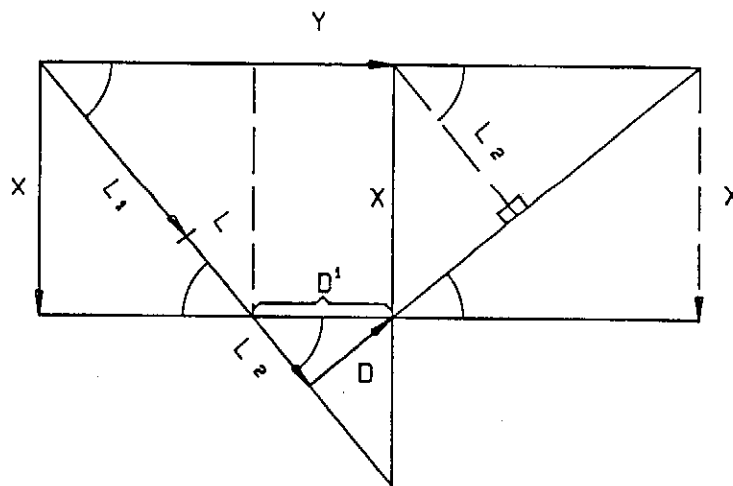
Figure C2 Axial and tangential forces exerted by unit span blade on fluid
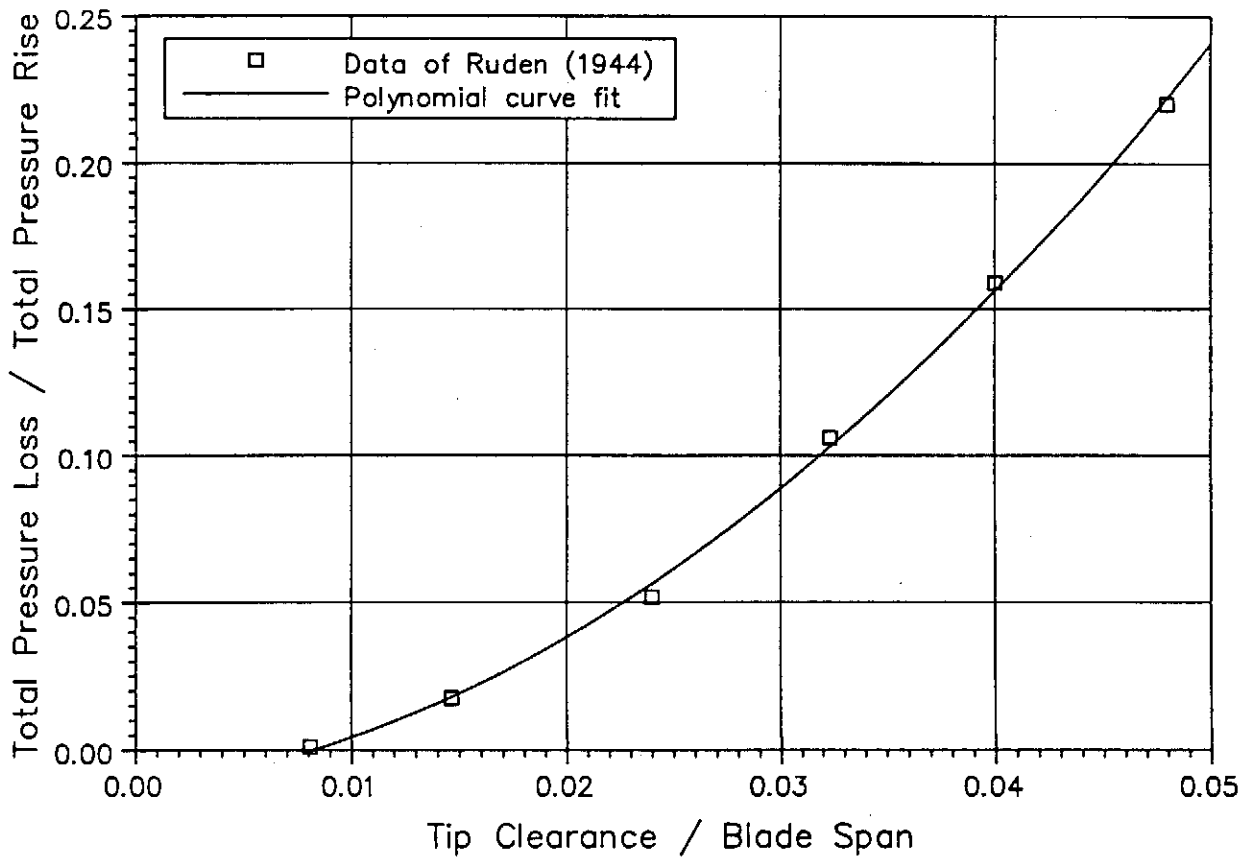
Figure C3 Tip clearance losses
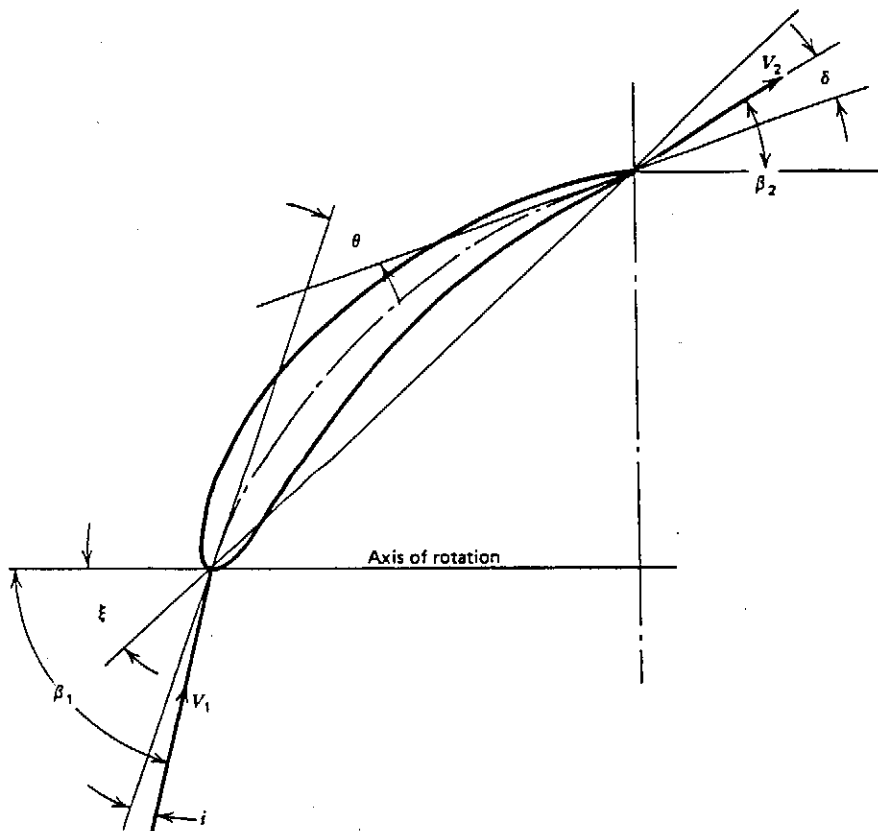
Figure C4 Blade camber, deviation and incidence angles
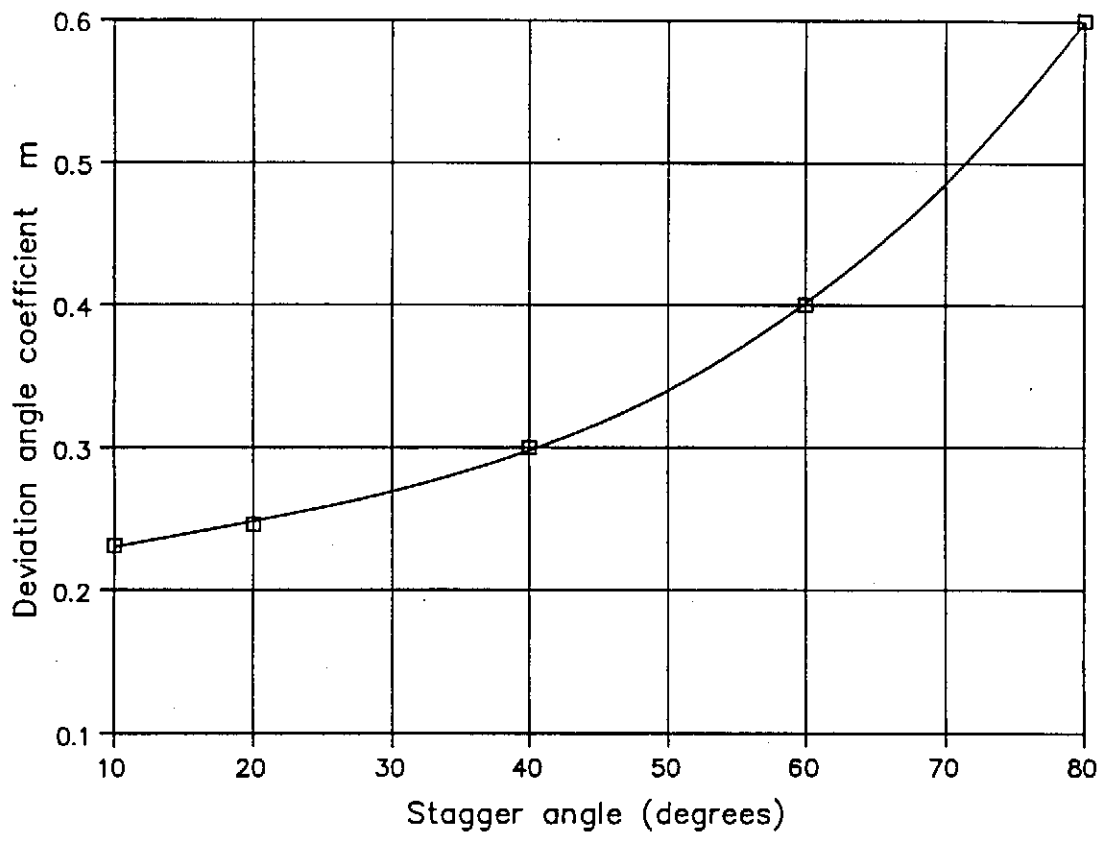
Figure C5 Deviation coefficient vs stagger angle

APPENDIX D FAN PERFORMANCE AND DATA PROCESSING

1.1 The Fan Laws and Data Scaling

The "Fan Laws" (see Osborne (1966), Dixon (1978)) are derived by means of a dimensional analysis, providing relationships for the pressure rise, volumetric flow rate and power consumption in terms of geometric and flow parameters, ie

$$p = k_p d^2 N^2 \rho . f_p (Re) \qquad\qquad \text{D 1}$$

$$Q = k_Q d^3 N . f_Q (Re) \qquad\qquad \text{D 2}$$

$$P = pQ = k_P d^5 N^3 . f_P (Re) \qquad\qquad \text{D 3}$$

In practice, it is found that the Reynolds number effects are quite small and they are usually neglected to give

$$p = k_p d^2 N^2 \rho \qquad\qquad \text{D 4}$$

$$\dot{Q} = k_Q d^3 N \qquad\qquad \text{D 5}$$

$$P = pQ = k_P d^5 N^3 \rho \qquad\qquad \text{D 6}$$

Since the fan laws are valid for any particular point on the fan pressure/volume characteristic, similar laws will be valid for every other point of operation, the only difference being the numerical values of the coefficients. The fan laws may therefore be used to scale the performance characteristics from a given set of operating conditions to another. In the following, the superscript (*) denotes an initial set of conditions, whilst the (') indicates the new or scaled condition.

$$\frac{p'}{p^*} = \frac{k_p d'^2 N'^2 \rho'}{k_p d^{*2} N^{*2} \rho^*}$$

<div align="right">D 7</div>

Since the constant k_p is identical for both the initial and scaled conditions,

$$p' = p^* \left(\frac{d'}{d^*}\right)^2 \left(\frac{N'}{N^*}\right)^2 \left(\frac{\rho'}{\rho^*}\right)$$

<div align="right">D 8</div>

Similarly, the volume flow and power relationships are

$$Q' = Q^* \left(\frac{d'}{d^*}\right)^3 \left(\frac{N'}{N^*}\right)$$

<div align="right">D 9</div>

$$p' = p^* \left(\frac{d'}{d^*}\right)^5 \left(\frac{N'}{N^*}\right)^3 \left(\frac{\rho'}{\rho^*}\right)$$

<div align="right">D 10</div>

1.2 Program FANDAP - Fan Data Processing

Program FANDAP calculates the fan performance characteristics from the primary measured flow variables and scales this data by means of the fan laws to a desired reference. The data input to FANDAP consists of two files, the test constants and the raw experimental data.

Table D1 depicts the structure of the test constant file which consists of data invariable in the context of test facility and the chosen reference conditions, ie

    i.   Reference density ρ'

    ii.   Reference temperature t'

    iii. Reference rotational speed N'

iv.   Reference fan diameter d'

v.   Hub-tip ratio x_b

vi   Fan tip radius r_t

vii.   Tip clearance t_c

viii   Plenum chamber cross-sectional area A_{plen}

ix.   Shroud diameter d

x.   Bellmouth diameter d_{bell}

xi.   Bellmouth calibration constant K_{bell}

xii.   Density of barometer fluid (mercury) ρ_{HG}

xiii. Local gravitational constant g

The raw data file (Table D2) consists of the test reference information, the ambient temperature and pressure and the measured parameters plenum chamber static pressure drop, bellmouth static pressure drop, input torque and rotational speed.

The calculation of the fan performance characteristics follows that of Venter (1990) and BS848(Type A). With reference to Figure 5.1, the complete fan characteristic can be calculated once the ambient pressure, temperature and density have been determined.

The calculations start by converting the test constants to base units, ie

$$t_{amb}(K) \;=\; t_{amb}(^{\circ}C) + 273.15 \qquad\qquad \text{D 11}$$

$$p_{amb} = \rho_{HG} g h_{HG} \times 1000 \qquad \text{D 12}$$

$$\rho_{amb} = \frac{p_{amb}}{R t_{amb}} \qquad \text{D 13}$$

$$A_2 = \frac{\pi d^2}{4} \qquad \text{D 14}$$

where h_{HG} is the ambient pressure measured in mm mercury and A_2 is the exit flow area of the fan shroud.

The mass flow rate through the fan test facility is obtained from

$$\dot{m} = K_{bell} \frac{\pi d_{bell}^2}{4} \sqrt{2\rho_{amb} \Delta p_{bell}} \qquad \text{D 15}$$

where K_{bell} is the compound calibration constant (described in Appendix E).

The measured plenum chamber pressure is the static pressure difference between the inside of the plenum chamber and the atmosphere, denoted $\Delta p_{S_{plen}}$. The ideal gas relationship is then used to calculate the air density inside the plenum chamber;

$$\rho_{plen} = \rho_{amb} \frac{(p_{amb} - \Delta p_{S_{plen}})}{p_{amb}} \qquad \text{D 16}$$

The velocity of the air within the plenum chamber is nearly zero due to the large cross-sectional area ratio between the plenum chamber and the fan inlet and therefore, the flow within

the plenum chamber is assumed incompressible. The fan static pressure is defined as the difference between the fan exit static pressure and the inlet total pressure, ie

$$p_{FS} = p_{amb} - (p_{s_{plen}} + p_{d_{plen}}) = \Delta p_{s_{plen}} - p_{d_{plen}} \qquad \text{D 17}$$

where the dynamic pressure is given by

$$p_{d_{plen}} = \frac{1}{2} \rho_{plen} V^2_{plen} = \frac{1}{2\rho_{plen}} \left(\frac{\dot{m}}{A_{plen}} \right)^2 \qquad \text{D 18}$$

The fan total pressure is defined as the difference between the total pressures at fan inlet and outlet, ie

$$p_{FT} = \left(p_{amb} + \frac{1}{2} \rho_{plen} V^2_2 \right) - (p_{amb} - \Delta p_{s_{plen}} + p_{d_{plen}}) \qquad \text{D 19}$$

$$= p_{FS} + \frac{1}{2} \rho_{plen} V^2_2$$

where V_2 is the deduced velocity through the fan shroud at the exit station. Note that in accordance with BS 848, Type A, the flow area reduction due to the fan hub is not taken into account, ie the full fan shroud diameter is used to determine the flow area;

$$V_2 = \frac{4\dot{m}}{\rho_{plen} \pi d^2} \qquad \text{D 20}$$

The power input to the shaft is deduced from the torque and rotational speed, ie

$$P_{fan} = \omega T = \frac{2\pi N T}{60} \qquad \text{D 21}$$

D.5

where ω and N are the rotational speeds in rad/s and rpm units respectively, and T the torque input to the fan shaft in Nm.

The fan total and static efficiencies are determined from the fan static pressure, volumetric flow rate and fan input power, ie

$$\eta_{FS} \;=\; \frac{p_{FS} Q_{plen}}{P_{fan}}$$

<div align="right">D 22</div>

$$\eta_{FT} \;=\; \frac{p_{FT} Q_{plen}}{P_{fan}}$$

<div align="right">D 23</div>

where the volumetric flow rate is calculated from the mass flow rate and the fan inlet conditions, ie

$$Q_{plen} \;=\; \frac{\dot{m}}{\rho_{plen}}$$

<div align="right">D 24</div>

Finally, the fan characteristics are scaled to the reference conditions by means of the fan laws described above, ie

$$Q' \;=\; Q^* \left(\frac{d'}{d*}\right)^3 \left(\frac{N'}{N*}\right)$$

<div align="right">D 25</div>

$$p'_{FS} \;=\; p^*_{FS} \left(\frac{d'}{d*}\right)^2 \left(\frac{N'}{N*}\right)^2 \left(\frac{\rho'}{\rho*}\right)$$

<div align="right">D 26</div>

$$P'_{fan} \;=\; P^*_{fan} \left(\frac{d'}{d*}\right)^5 \left(\frac{N'}{N*}\right)^3 \left(\frac{\rho'}{\rho*}\right)$$

<div align="right">D 27</div>

$$\eta'_{FS} \;=\; \eta^*_{FS}$$

<div align="right">D 28</div>

$$\eta'_{FT} = \eta^{*}_{FT}$$

D 29

where in this instance, the prime superscript refers to the reference conditions and the asterisk to the experimental conditions.

1.3 Sample Calculations

Table D2 is a typical set of measured fan performance data, in this case the B1 fan for a 63° stagger angle setting and including the nose cone and root seals. The processing of the experimental data is illustrated here by performing the calculations for a single point on the fan characteristics in the sequence of Equations D11 to D29. The FANDAP output file (Table D3) for this particular data set is included for reference.

The tenth data point has the following values :

Plenum chamber pressure differential	197.473 Pa
Bell mouth pressure drop	273.213 Pa
Torque	72.450 Nm
Rotational speed	751.531 RPM

Using this data and the test constants of Table D1, the calculations are as follows :

$$
\begin{aligned}
t_{amb} &= t_{amb} + 273.15 \\
&= 24.0 + 273.15 \\
&= 297.15 \ K
\end{aligned}
$$

$$p_{amb} = \rho_{HG} g h_{HG}$$

$$= 13579.04 \times 9.796 \times 753.8 \times 10^{-3}$$

$$= 100270.684 \; Pa$$

$$\rho_{amb} = \frac{p_{amb}}{R t_{amb}}$$

$$= \frac{100270.684}{287.08 \times 297.15}$$

$$= 1.175 \; kg/m^3$$

$$A_2 = \frac{\pi d^2}{4}$$

$$= \frac{\pi \times (1.542)^2}{4}$$

$$= 1.867$$

$$\dot{m} = K_{bell} \frac{\pi d_{bell}^2}{4} \sqrt{2 \rho_{amb} \Delta p_{bell}}$$

$$= \frac{0.9802 \times \pi \times (1.008)^2}{4} \sqrt{2 \times 1.175 \times 273.213}$$

$$= 19.820 \; kg/s$$

$$\rho_{plen} = \rho_{amb} \frac{(p_{amb} - \Delta p_{S_{plen}})}{p_{amb}}$$

$$= 1.175 \times \frac{(100270.684 - 197.473)}{100270.684}$$

$$= 1.173 \ kg/m^3$$

$$P_{d_{plen}} = \frac{1}{2\rho_{plen}} \left(\frac{\dot{m}}{A_{plen}} \right)^2$$

$$= \frac{1}{2 \times 1.173} \left(\frac{19.829}{16.0} \right)^2$$

$$= 0.655 \ Pa$$

$$p_{FS} = \Delta p_{S_{plen}} - P_{d_{plen}}$$

$$= 197.473 - 0.655$$

$$= 196.818 \ Pa$$

$$V_2 = \frac{4\dot{m}}{\rho_{plen} \pi d^2}$$

$$= \frac{4 \times 19.829}{1.173 \times \pi \times (1.542)^2}$$

$$= 9.052 \ m/s$$

$$p_{FT} = p_{FS} + \frac{1}{2}\rho_{plen}V_2^2$$

$$= 196.818 + \frac{1}{2} \, 1.173 \times (9.032)^2$$

$$= 244.668 \; Pa$$

$$P_{fan} = \frac{2\pi NT}{60}$$

$$= \frac{2 \times \pi \times 751.531 \times (72.450 - 2.0)}{60}$$

$$= 5544.425 \; W$$

$$Q_{plen} = \frac{\dot{m}}{\rho_{plen}}$$

$$= \frac{19.820}{1.173}$$

$$= 16.897 \; m^3/s$$

$$\eta_{FS} = \frac{p_{FS}Q_p}{P_{fan}}$$

$$= \frac{197.428 \times 16.897}{5544.425} \times 100$$

$$= 59.981 \; \%$$

$$\eta_{FT} = \frac{p_{FT} Q_{plan}}{P_{fan}}$$

$$= \frac{244.688 \times 16.897}{5544.425} \times 100$$

$$= 74.570 \ \%$$

$$Q' = Q^* \left(\frac{d'}{d^*}\right)^3 \left(\frac{N'}{N^*}\right)$$

$$= 16.897 \left(\frac{1.542}{1.542}\right)^3 \left(\frac{750.0}{751.531}\right)$$

$$= 16.862 \ m^3/s$$

$$p'_{FS} = p^*_{FS} \left(\frac{d'}{d^*}\right)^2 \left(\frac{N'}{N^*}\right)^2 \left(\frac{\rho'}{\rho^*}\right)$$

$$= 196.818 \left(\frac{1.542}{1.542}\right)^2 \left(\frac{750.0}{751.531}\right)^2 \left(\frac{1.2}{1.173}\right)$$

$$= 200.529 \ Pa$$

$$p'_{FT} = p^*_{FT} \left(\frac{d'}{d^*}\right)^2 \left(\frac{N'}{N^*}\right)^2 \left(\frac{\rho'}{\rho^*}\right)$$

$$= 244.688 \left(\frac{1.542}{1.542}\right)^2 \left(\frac{750.0}{751.531}\right)^2 \left(\frac{1.2}{1.173}\right)$$

$$= 249.301 \ Pa$$

$$P'_{fan} = P^*_{fan}\left(\frac{d'}{d*}\right)^5\left(\frac{N'}{N*}\right)^3\left(\frac{\rho'}{\rho*}\right)$$

$$= 5544.425\left(\frac{1.542}{1.542}\right)^5\left(\frac{750.0}{751.531}\right)^3\left(\frac{1.2}{1.173}\right)$$

$$= 5637.452 \quad W$$

Reference density	$1.2 \ kg/m^3$
Reference temperature	$20.0 \ °C$
Reference rotational speed	$750.0 \ rpm$
Reference fan diameter	$1.542 \ m$
Hub-tip ratio	$0.4 \ [.]$
Fan tip radius	$0.771 \ m$
Tip clearance	$0.003 \ m$
Plenum chamber X-sectional area	$16.0 \ m^2$
Shroud diameter	$1.542 \ m$
Bellmouth diameter	$1.008 \ m$
Bellmouth calibration constant	$0.9802 \ [.]$
Density of barometer fluid (mercury)	$13579.04 \ kg/m^3$
Local gravitational constant	$9.796 \ m/s^2$

Table D1. Test constants

REFERENCE - Date : 17/02/93; Time 15h50

B1 fan

nose cone and root seals

Axial position   40 mm

Stagger angle   63 deg

Pressure   (amb)   753.8 mm Hg

Temperature (amb)   24.0 deg C

$\Delta p_{s_{plen}}$ (Pa)	Δp_{bell} (Pa)	T (Nm)	N (rpm)
469.287	12.894	65.925	751.073
449.946	22.172	68.829	757.533
403.930	37.632	70.391	751.984
382.244	56.340	73.746	752.666
352.376	77.936	75.832	752.189
328.296	102.906	77.547	753.489
306.799	135.859	78.423	752.307
278.037	173.839	78.411	751.252
238.445	222.264	75.849	749.459
197.473	273.213	72.450	751.531
144.421	321.335	66.061	749.087
104.027	368.866	61.833	758.686
69.673	391.179	55.313	750.660
45.042	421.207	51.550	751.761
25.369	439.488	48.563	752.439

Table D2. Test data file

D.14

Table D3. FANDAP output file

F A N D A P - Fan Data Processor - Version 2.0

REFERENCE : B1 STAGGER ANGLE EFFECTS 17th Feb 1993 (B1_7 (3)) ax pos=40; ang=63 deg NC/RS

FAN GEOMETRY
----

hub-tip ratio	[.]	0.400
tip radius	(m)	0.771
tip clearance	(m)	0.003
fan shroud diameter	(m)	1.542
ref. shroud diameter	(m)	1.542
plenum chamber x-area	(m^2)	16.000
bell-mouth diameter	(m)	1.008
bell-mouth coefficient	[.]	0.980

TEST CONSTANTS
----

local grav. Constant	(kg.m/s^2)	9.796
ambient pressure	(mm - Hg)	753.800
ambient temperature	(deg C)	24.000
ambient pressure	(Pa)	100270.700
ref. density	(kg/m^3)	1.200
ref. temperature	(deg C)	20.000
ref. pressure	(Pa)	100989.000
ref. rotational speed	(RPM)	750.000

MEASURED DATA

	Ps(plen)	dP(bell)	Torque	RPM
1	469.2870	12.8940	65.9250	751.0730
2	449.9460	22.1720	68.8290	757.5330
3	403.9300	37.6320	70.3910	751.9840
4	382.2440	56.3400	73.7460	752.6660
5	352.3760	77.9360	75.8320	752.1890
6	328.2960	102.9060	77.5470	753.4890
7	306.7990	135.8590	78.4230	752.3070
8	278.0370	173.8390	78.4110	751.2520

9	238.4450	222.2640	75.8490	749.4590
10	197.4730	273.2130	72.4500	751.5310
11	144.4210	321.3350	66.0610	749.0870
12	104.0270	368.8660	61.8330	758.6860
13	69.6730	391.1790	55.3130	750.6600
14	45.0420	421.2070	51.5500	751.7610
15	25.3690	439.4880	48.5630	752.4390

PERFORMANCE PARAMETERS - DIMENSIONAL

	Vol. Flow Rate	FSP	FVP	FTP
1	3.676	479.945	2.303	482.248
2	4.778	452.239	3.893	456.131
3	6.268	411.769	6.705	418.473
4	7.661	388.821	10.020	398.841
5	9.013	358.723	13.878	372.601
6	10.336	332.903	18.261	351.164
7	11.893	311.919	24.185	336.104
8	13.468	283.266	31.033	314.299
9	15.259	243.817	39.867	283.684
10	16.864	200.511	48.736	249.247
11	18.339	147.225	57.695	204.920
12	19.392	103.010	64.563	167.574
13	20.177	70.100	69.941	140.041
14	20.901	44.765	75.089	119.855
15	21.326	24.672	78.207	102.880

	Vol. Flow Rate	Power	Eff(s)	Eff(t)
1	3.676	5135.021	34.356	34.521
2	4.778	5276.105	40.956	41.308
3	6.268	5476.879	47.125	47.892
4	7.661	5733.901	51.948	53.287
5	9.013	5906.333	54.741	56.859
6	10.336	6021.241	57.148	60.283
7	11.893	6108.901	60.724	65.433
8	13.468	6123.347	62.302	69.128
9	15.259	5944.034	62.590	72.825
10	16.864	5636.917	59.987	74.568
11	18.339	5156.482	52.361	72.880
12	19.392	4693.166	42.564	69.242
13	20.177	4270.187	33.122	66.170
14	20.901	3956.194	23.650	63.321
15	21.326	3710.279	14.181	59.134

	Vol. Flow Rate	Mass Flow Rate	Avg. Exit Vel.
1	3.676	4.307	1.962
2	4.778	5.647	2.573
3	6.268	7.357	3.352
4	7.661	9.002	4.101
5	9.013	10.588	4.823
6	10.336	12.166	5.542
7	11.893	13.979	6.368
8	13.468	15.813	7.204
9	15.259	17.880	8.146
10	16.864	19.824	9.031
11	18.339	21.499	9.794
12	19.392	23.034	10.493
13	20.177	23.721	10.806
14	20.901	24.614	11.213
15	21.326	25.143	11.454

DATA CHECKING

	Density (p)	Q (p)	Mass Flow (p)	FVPP
1	1.170	3.681	4.307	2.252
2	1.170	4.826	5.647	3.872
3	1.171	6.285	7.357	6.576
4	1.171	7.688	9.002	9.847
5	1.171	9.039	10.588	13.625
6	1.172	10.385	12.166	17.995
7	1.172	11.929	13.979	23.762
8	1.172	13.490	15.813	30.414
9	1.173	15.248	17.880	38.902
10	1.173	16.899	19.824	47.839
11	1.174	18.317	21.499	56.294
12	1.174	19.617	23.034	64.647
13	1.175	20.194	23.721	68.582
14	1.175	20.950	24.614	73.864
15	1.175	21.396	25.143	77.085

DATA CHECKING

	PDP	PFS	PFT	V2	POW(P)
1	0.031	469.256	471.508	1.962	5027.841
2	0.053	449.893	453.765	2.573	5301.456
3	0.090	403.840	410.415	3.352	5385.626
4	0.135	382.109	391.956	4.101	5654.948
5	0.187	352.189	365.814	4.823	5815.677
6	0.247	328.049	346.044	5.542	5961.050
7	0.326	306.473	330.236	6.368	6020.711
8	0.417	277.620	308.034	7.204	6011.325
9	0.532	237.913	276.814	8.146	5795.903
10	0.654	196.819	244.657	9.031	5544.425
11	0.769	143.652	199.946	9.794	5025.214
12	0.883	103.144	167.792	10.493	4753.697
13	0.936	68.737	137.319	10.806	4190.878
14	1.007	44.035	117.899	11.213	3900.785
15	1.051	24.318	101.404	11.454	3668.942

APPENDIX E CALIBRATION

The fan test facility used to measure the fan performance data
(described in Chapter 5) is the same as that used by Venter(1990)
who performed detailed calibrations of the inlet bellmouth, and
measured both the system leakage and the velocity profile inside
the plenum chamber. Since these factors are functions of the
system and unlikely to change dramatically with the passage of
time, only the pressure and torque transducers were calibrated.
What follows is a summary of the assumed system constants as
well as the transducer calibrations as used in the fan performance
tests.

1.1 Inlet Bellmouth

The inlet bellmouth is used to deduce the mass flow rate
through the fan test facility by measuring the pressure drop
across the device, ie

$$\dot{m} = \alpha \epsilon \frac{\pi d_{bell}^2}{4} \sqrt{2 \rho_{amb} \Delta p_{bell}}$$

<div align="right">E 1</div>

where the compound calibration coefficient, $\alpha\epsilon$, is specified
by BS 848, Type A.

Due to space limitations, Venter was forced to alter some
dimensions, thereby invalidating the recommended calibration
constants. In particular, the transformation piece between
the inlet bellmouth and the remainder of the facility is 1.500
m long and not three inlet diameters (3.000 m) as stipulated
by BS 848, Type A. However, in accordance with the provisions
of BS 848, Type A, Venter carefully calibrated the bellmouth

by means of pitot static traverses for different volumetric flow rates and determined that the compound calibration constant for the "non-standard" dimensions to be

$$\alpha \epsilon = K_{bell} = 0.9802 \qquad\qquad\qquad E \ 2$$

as opposed to the recommended value of 0.985

1.2 System Air Leakage

Venter evaluated the magnitude of system leakages and their effect on the V fan pressure characteristic. After sealing all access holes in the unit, a centrifugal fan equipped with a throttle and mass flow rate measuring device was used evacuate the facility and for a range negative plenum chamber pressures up to 550 Pa, Venter measured a maximum mass flow leakage of the order 0.045 kg/s. Venter then plotted a leakage-corrected V fan characteristic against a typical "as measured" fan static pressure curve and found that the effect of leaking air proved negligible. In light of the findings of Venter, no measurements of system leakage were performed, although prior to testing, all joints in the test facility were examined and where necessary, re-sealed with silicone rubber.

1.3 Plenum Chamber Velocity Profile

In accordance with BS 848, Type A, Venter measured the velocity distribution inside the plenum chamber in the same plane as the four static pressure tappings used to measure fan inlet pressure and found that nowhere does the air flow velocity exceed 1.25 times the average velocity (or a maximum 2.5 m/s) as required by BS 848, Type A.

E.2

1.4 Torque Transducer

A Höttinger T2 resistive, full-bridge torque transducer, with a range ±500 Nm was used to establish the input torque to the fan impeller. The torque transducer was calibrated statically using a balance arm and four steel discs of pre-determined mass, as depicted in Figure E1. The balance arm was bolted to the shaft of the fan drive train with the mass center of the balance arm adjusted to correspond with the axis of the fan shaft by means of a compensating counter weight. Loading the four discs sequentially provided a range of known torques to the fan shaft, from which the linear relationship between applied torque and output voltage was established. A Höttinger 3073 bridge amplifier was used to supply the excitation voltage and to amplify the output signal from the transducer. The calibration curve shown in Figure E2 indicates the linear relationship between the applied torque and the output signal for two different calibrations, this calibration data being listed in Table E1.

1.5 Pressure Transducers

The static pressure differences across the bellmouth and plenum chamber are both measured. The static pressure at the fan outlet as well as static pressure at the bellmouth inlet are assumed equal to ambient pressure.

For both pressure measurements, inductive differential pressure transducers (Höttinger PD 1) with a range ±1000 N/m^2 are used. The pressure transducers were calibrated against a Betz manometer with 0.2 $mmWg$ divisions. Calibration curves for both the bellmouth and plenum chamber pressure transducers are indicated in Figures E3 and E4 respectively with tabulated calibration data in Tables E2 and E3 respectively.

1.6 Rotational Speed

The rotational speed of the fan shaft is measured by means of magnetic pick-up and a frequency counter. The magnetic pick-up is placed in close proximity to a 7 tooth mild steel disc. As each tooth of the disc passes beneath the magnetic pick-up, a pulsed signal is transmitted to the frequency counter and the frequency of the pulses provides a measure of the rotational speed.

A pulse generator is used to generate a 100 Hz square wave signal for which the full scale output is adjusted to read 10 V. A frequency output of 100 Hz corresponds to a rotational speed of 857.1 rpm because there are 7 teeth on the metal disc used to activate the pick-up sensor.

Rotational speed measurements obtained from the frequency counter were compared to readings using both optical and mechanical hand held tachometers, indicating agreement to within 1.5 %.
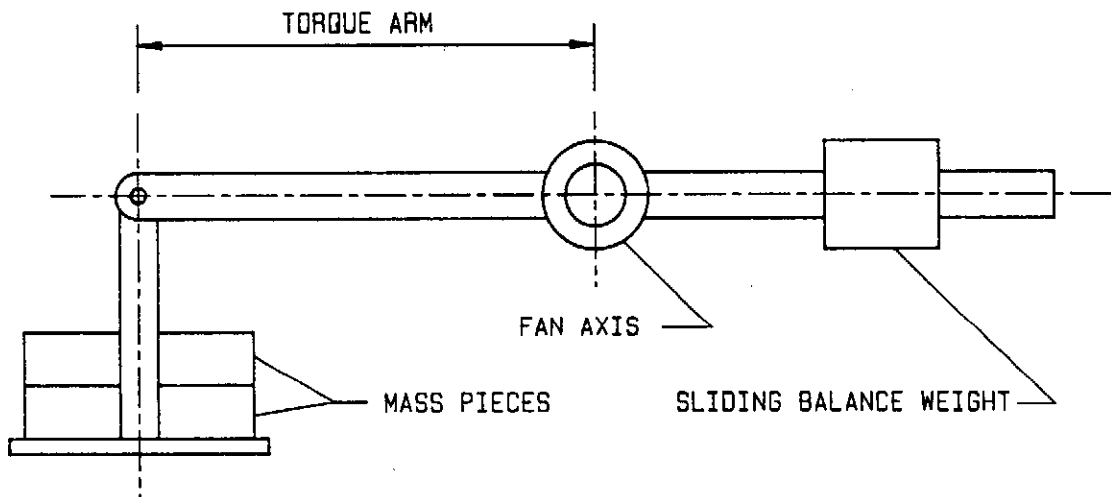

Figure E1 Torque calibration rig

E.4

Mass	Torque	Voltage (1)	Voltage (2)
kg	Nm	V	V
0.000	0.0000	0.006	0.005
4.740	24.1797	0.967	0.981
9.670	49.3286	1.997	2.012
14.523	74.0847	3.004	3.021
19.473	99.3356	4.030	4.031

Table E.1 Torque transducer calibration data

TORQUE TRANSDUCER CALIBRATION
$T = 24.6385V - 0.0244085$
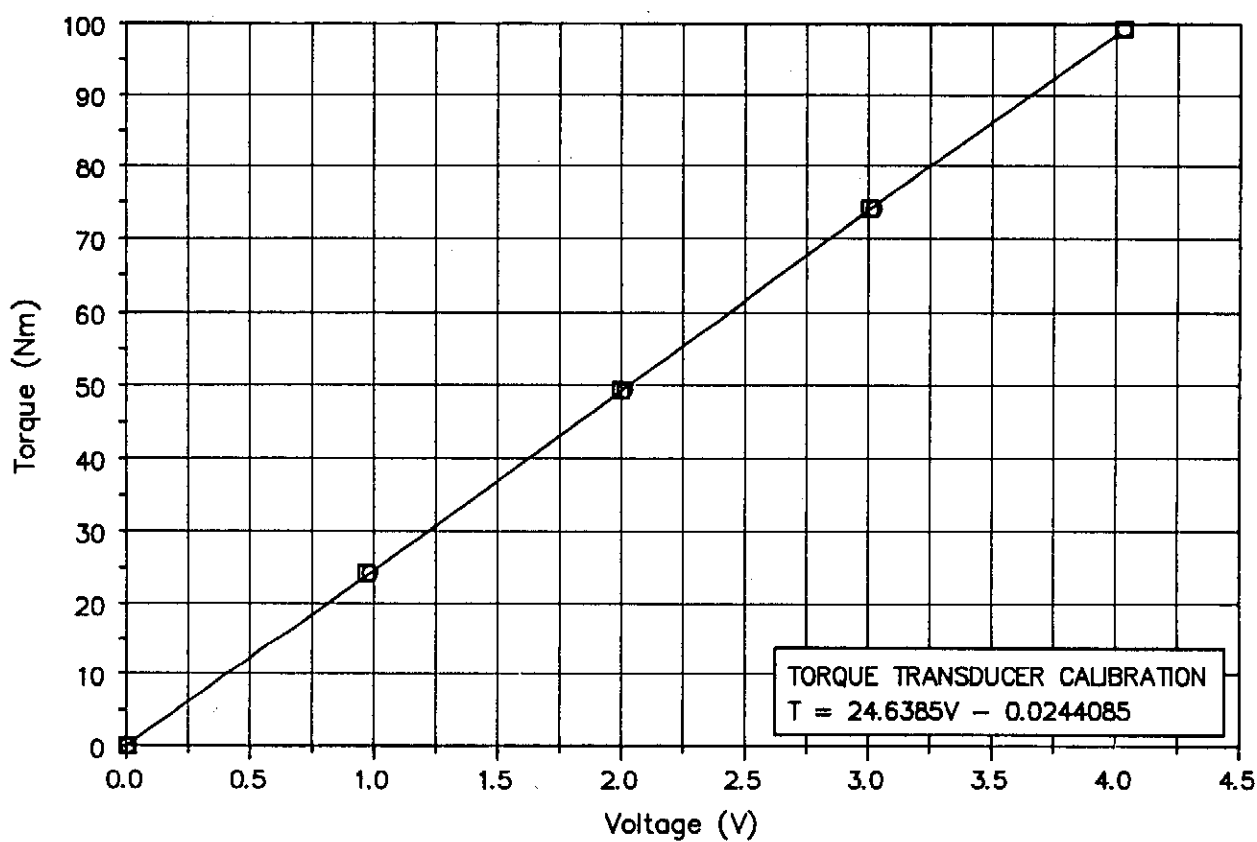
Figure E2 Torque calibration curve

E.5

mm Water	Pressure	Voltage
	Pa	V
0.0	0.00	0.0002
5.0	48.98	0.640
10.0	97.96	1.291
15.0	146.94	1.946
20.0	195.92	2.599
25.0	244.90	3.249
30.0	293.88	3.908
35.0	342.86	4.571
40.0	391.84	5.211
45.0	440.82	5.868
50.0	489.80	6.532
55.0	538.78	7.184
60.0	587.76	7.840

Table E.2 Bellmouth pressure transducer calibration

PRESSURE TRANSDUCER CALIBRATION
BELLMOUTH
P = 74.8844V + 1.04034
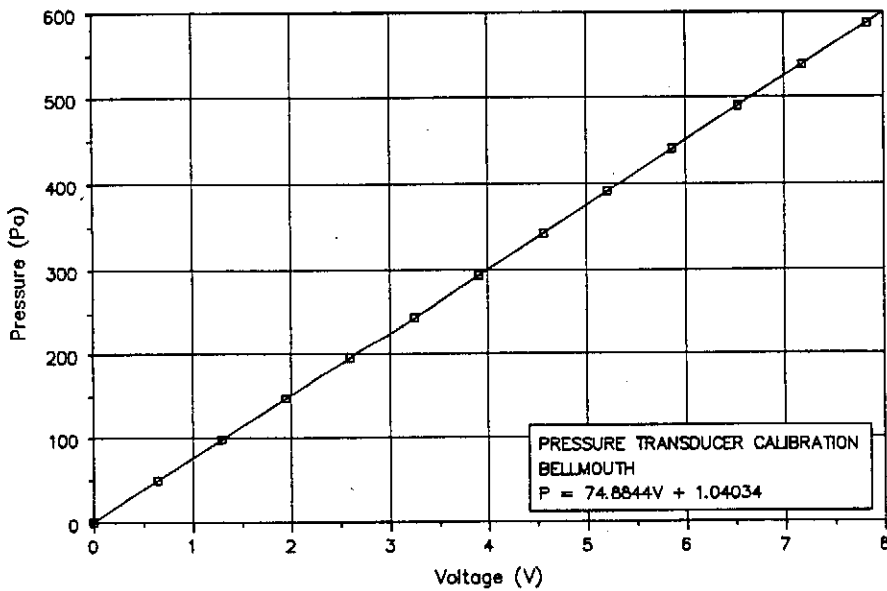
Figure E3 Bellmouth calibration curve

E.6

mm Water	Pressure	Voltage
	Pa	V
0.0	0.00	-0.007
5.0	48.98	0.617
10.0	97.96	1.259
15.0	146.94	1.906
20.0	195.92	2.553
25.0	244.90	3.196
30.0	293.88	3.839
35.0	342.86	4.476
40.0	391.84	5.121
45.0	440.82	5.759
50.0	489.80	6.410
55.0	538.78	7.050
60.0	587.76	7.690

Table E.3 Plenum chamber pressure transducer calibration

PRESSURE TRANSDUCER CALIBRATION
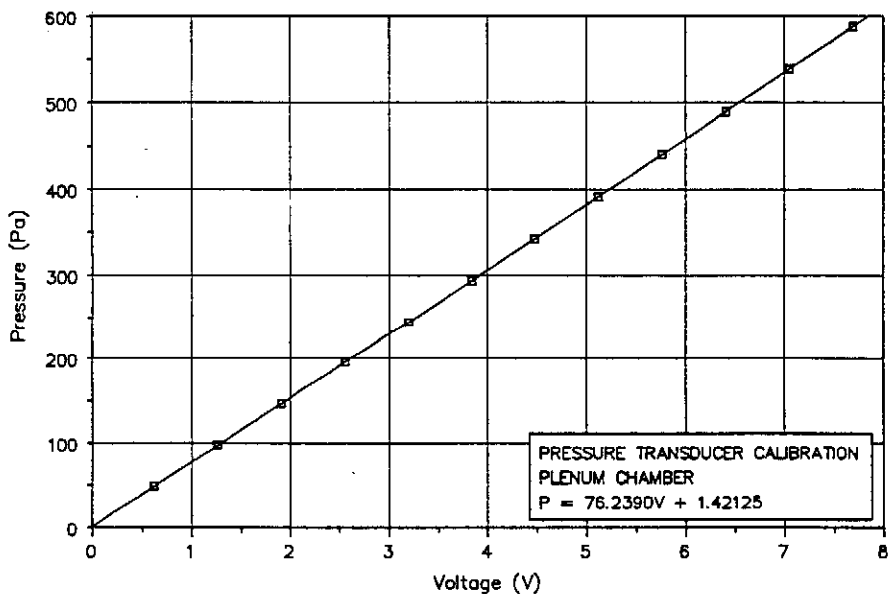PLENUM CHAMBER
P = 76.2390V + 1.42125

Figure E4 Plenum chamber calibration curve

E.7

APPENDIX F ACTUATOR DISC THEORY

Dixon (1978) has summarised the salient results of actuator disc theory, described in more detail by Hawthorne and Horlock(1954)

An isolated actuator disc is illustrated in Figure F1 with radial equilibrium established at fairly large distances from the disc. Using the simple radial equilibrium equations, an approximate solution to the velocity fields far upstream and downstream of the actuator disc can be found in terms of the axial velocity distributions far upstream and downstream of the disc.

The conditions far upstream and downstream are denoted by the subscripts ∞_1 and ∞_2 respectively. Actuator disc theory proves that at the disc ($x = 0$) for any radius, the axial velocity is equal to the mean of the axial velocities at ∞_1 and ∞_2 respectively at the same radius, ie,

$$c_{x_o} = \frac{1}{2}(c_{x_{\infty 1}} + c_{x_{\infty 2}})$$

F 1

In the downstream flow field ($x \geq 0$), the difference in axial velocity at some position (x,r) to that at position (∞,r) is conceived as a velocity perturbation. The axial velocity perturbation at the disc ($x = 0, r$) is denoted by Δ_o and that at position (x,r) by Δ. The important result is that velocity perturbations decay exponentially away from the disc, the same being true for the upstream flow field, ($x \leq r$). The result obtained for the decay rate is :

$$\frac{\Delta}{\Delta_o} = 1 - \exp\left(\mp\frac{\pi x}{r_t - r_h}\right)$$

F 2

where the minus and plus signs apply to the flow regions $(x \geq 0)$ and $(x \leq r)$ respectively. Now since

$$c_{x_1}(x) = c_{x_{o1}} + \Delta \qquad \text{F 3}$$

$$c_{x_2}(x) = c_{x_{o1}} - \Delta \qquad \text{F 4}$$

$$\Delta_o = \frac{1}{2}(c_{x_{\infty1}} - c_{x_{\infty2}}) \qquad \text{F 5}$$

combining with Equation F2 gives the variation in axial velocity through the blade row at a constant radial position :

$$c_{x_1}(x) = c_{x_{\infty1}} - \frac{1}{2}(c_{x_{\infty1}} - c_{x_{\infty2}})\exp\left(+\frac{\pi x}{r_t - r_h}\right) \qquad \text{F 6}$$

$$c_{x_1}(x) = c_{x_{\infty2}} + \frac{1}{2}(c_{x_{\infty1}} - c_{x_{\infty2}})\exp\left(-\frac{\pi x}{r_t - r_h}\right) \qquad \text{F 7}$$

The resulting equations for axial velocity distribution above can now be used to determine the streamline shape and position through the fan rotor. At the far upstream location, the axial velocity profile is constant and the mass-flow rate at any radius is given by

$$\dot{m}(r) = \pi \rho c_{x_1}(r^2 - r_h^2) \qquad \text{F 8}$$

Selecting a series of radii across the flow annulus at the far upstream station will determine the starting positions for a set of streamlines. Since the axial velocity profile will in general not be constant through the fan, the position of a particular streamline at a downstream station will be given by that radius at which the mass flow rate between the hub and

this radius is equal to the mass flow rate between the hub and the original radius at the far upstream station. In FANVTX, the procedure for the calculation of the streamlines is as follows :

i. Streamline radii at the far upstream station are selected and the corresponding mass flow rates between the hub and each streamline are calculated.

ii. At each pre-selected axial station, the axial velocity profile is calculated using the actuator disc equations.

iii.At each axial station, the velocity profile is integrated to give the mass flow rate distribution as a function of radius, ie

$$\dot{m}(r) = \int_{r_h}^{r} 2\pi\rho c_x(r).r\,dr$$

F 9

iv. For a given streamline, the radius is then interpolated from the mass flow rate/radius relationship at the corresponding far upstream mass flow rate.
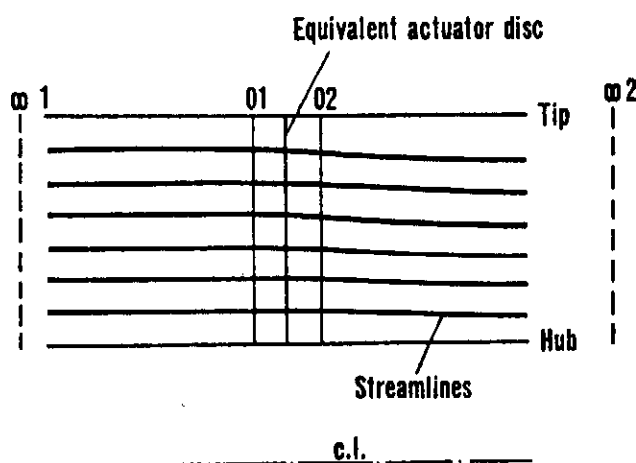

Figure F1 Actuator disc schematic (from Dixon (1978))

REFERENCES

Bard, H. and Böös, E. "Aerodynamic Fan Design - Computer Techniques", Industrial Fans - Aerodynamic Design, Instn. of Mech. Engrs., April 1987.

Bass, R.M., "Factors Influencing the Aerodynamic Design of Low Pressure Axial Fans", Industrial Fans - Aerodynamic Design, Instn. of Mech. Engrs., April 1987.

British Standards Institution, "Fans for General Purposes", Part 1, Methods of Testing Performance", BS848, 1980.

Carter, A.D.S., "The Low Speed Performance of Related Aerofoils in Cascades", Gt. Britain Aer. Research Council, ARC CP 29, 1950.

Carter, A.D.S., "The Axial Compressor" in H. Roxbee-Cox (Ed), Gas Turbine Principles and Practice, Newnes, London, 1955.

Collar, A.R., "The Design of Wind Tunnel Fans", Reports and Memoranda, No.1889, 1940.

Dixon, S.L., "Fluid Mechanics-Thermodynamics of Turbomachinery", Third Edition, William Clowes (Beccles) Ltd., Great Britain, 1978.

Glassman, A.J., "Turbine Design and Application", NASA, Washington DC, NASA SP-290, 1975.

Hawthorne, W.R., and Horlock J.H., "Actuator Disc Theory of the incompressible Flow in Axial Compressors", Proc. Instn. Mech. Engrs., London, 1962.

Hay, N., Metcalfe, R. and Reizes, J.A., "A Simple Method for the Selection of Axial Fan Blade Profiles", Proc. Inst. Mech. Engrs., Vol.192, No.25, 1978.

Hay, N., Mather, J.S.B. and Metcalfe, R., "Fan Blade Selection for Low Noise", Industrial Fans - Aerodynamic Design, Instn. of Mech. Engrs., April 1987.

Keller, C., "The Theory and Performance of Axial-Flow Fans", McGraw-Hill Book Company, Inc., 1937.

Lieblein, S., "Experimental Flow in Two Dimensional Cascades", in I.A. Johnson and R.O. Bullock (Eds), Aerodynamic Design of Axial Flow Compressors, NASA Report SP-36, 1965.

McGhee, R.J. and Beasley, W.D, "Low-Speed Aerodynamic Characteristics of a 17 Percent Thick Airfoil Section Designed for General Aviation Applications", NASA TN D-7428, December 1978.

McGhee, R.J.,Beasley, W.D, and Whitcomb, R.J, "NASA Low and Medium Speed Airfoil Development" in Advanced Technology Airfoil Research, Vol.2., NASA CP 2046, March 1980.

McKenzie, A.B., "The Selection of Fan Blade Geometry for Optimum Efficiency", Proc. Inst. Mech. Engrs., Vol.192, No.25, 1978.

Novak, R.A., "Streamline Computing Procedures for Fluid Flow Problems", Journal of Engineering for Power, Trans. ASME, Vol.89, 1967, pp. 478-490.

Osborne, W.C., "Fans", Pergamon Press Ltd., 1966.

Patterson, G.N., "Ducted Fans : Design for High Efficiency", Report ACA-7, Australian Council for Aeronautics, July 1944.

Ruden, P., "Investigation of Single Stage Axial Flow Fans", NACA Tech. Mem. No 1062, 1944.

Sinclair, M., von Backström, T.W. and du Buisson, J.J., "Heuristic Methods for Arranging Blades to Minimize Rotor Unbalance", Eng. Opt., Vol.22, pp 19-26, 1993.

Smith, T.W., "A Practical Approach to the Design of Low Pressure Axial and Mixed Flow Fans", Industrial Fans - Aerodynamic Design, Instn. of Mech. Engrs., April 1987.

Smith, Jr., L.H., "The Radial-Equilibrium Equation of Turbomachinery", Journal of Engineering for Power, Trans. ASME, Series A, Vol.88, 1966, pp. 1-12.

Thwaites, B., "A Note on the Design of Ducted Fans", The Aeronautical Quarterly, Vol.3, November 1951.

Van Niekerk, C.G., "Ducted Fan Design Theory", Journal of Applied Mechanics, 1958.

Van Niekerk, C.G., "Ontwerp van Waaiers met Höe Rendement en Lae Lawaai-Intensiteit", D.Sc thesis, University of Pretoria, 1964.

Van Rhyn, A.J., "Ondersoek na die Invloed van die Verandering van die Naaf-Huls Verhouding op die Werking van 'n Aksiaal Waaier", Project Report, University of Stellenbosch, 1993.

Venter, S.J., "The Effectiveness of Axial Flow Fans in A-Frame Plenums", PhD thesis, University of Stellenbosch, 1990.

Wallis, R.A, "Axial Flow Fans and Ducts", John Wiley & Sons, Inc., 1983.

Wallis, R.A, "A Rationalised Approach to Blade Element Design, Axial Flow Fans", Proc. Third A'asian Conf. Hydraulics and Fluid Mechanics, Sydney, 1968.

Zweifel, O., "The Spacing of Turbomachine Blading, Especially with Large Angular Deflection", Brown Boveri Rev., December 1945.